

AN EXPERIMENTAL AND COMPUTATIONAL STUDY
OF THE FLOW
IN A TRANSONIC COMPRESSOR ROTOR

by

William T. Thompkins, Jr.

GTL Report No. 129

May 1976

This research was carried out in the
Gas Turbine Laboratory, M.I.T., supported
by the NASA Lewis Research Center under
Grant NGL 22-009-383.

ABSTRACT

A comprehensive investigation of the flow field produced by an isolated transonic compressor rotor has been completed. This rotor has an overall diameter of two feet, an inlet hub/tip ratio of 0.5, a tip Mach number of 1.2 and a total pressure ratio of 1.65. The time resolved three dimensional exit flow produced by this rotor was experimentally measured with sufficient spatial and temporal resolution to determine velocity components and pressures inside individual blade wakes and in the surrounding flow. A numerical calculation of the steady inviscid three dimensional through-flow was computed using MacCormack's second order accurate time-marching scheme. Comparisons between the numerical solution, the exit flow measurements, and measurements of the intra-blade static density field obtained by gas fluorescence showed that the inviscid computation accurately models transonic compressor aerodynamics and rotor blade pressure distributions in the upstream portion of the passages, the viscous effects influencing mainly the downstream portions. It is felt that such a computation procedure has great potential as a compressor design and development tool especially when coupled with a suitable boundary layer analysis.

ACKNOWLEDGMENTS

Jack L. Kerrebrock has contributed time, money, and understanding to this work, and his contributions are gratefully acknowledged. Thorwald Christensen and Allen Epstein, who contributed several figures in Chapter IV, both aided greatly in the experimental portion of this project. Mr. W. D. McNally of the NASA Lewis Research Center whose efforts provided much of the computer time necessary for this project contributed to the theoretical portion of this work.

This research was supported by NASA Lewis Research Center under Grant NGL 22-009-383 supervised by Mr. W. D. McNally.

-5-
TABLE OF CONTENTS

<u>Chapter</u>		<u>Page No.</u>
I	INTRODUCTION	12
II	EXPERIMENTAL MEASUREMENTS	
	2.1 Test Facility	15
	2.2 Instrumentation	18
	2.3 Data Recording and Data Reduction	21
	2.4 Basic Flow Field Data	23
III	NUMERICAL METHODS	
	3.1 Introduction	34
	3.2 Numerical Procedures	35
	3.3 Boundary Conditions	40
	3.4 Results of Numerical Calculation	51
IV	COMPARISON OF RESULTS AND DISCUSSION	
	4.1 Comparison of Inviscid Solution to Intra-Blade Density Measure- ments	58
	4.2 Comparison of Inviscid Solution to Exit Flow Measurements	62
V	CONCLUSIONS AND DISCUSSION	67
	REFERENCES	69
	FIGURES	
	Chapter II	72
	Chapter III	109
	Chapter IV	126

LIST OF FIGURES

<u>Figure</u>		<u>Page No.</u>
2.1	Scale Drawing of Blowdown Test Facility	72
2.2	Typical Facility Parameters for Test Run	73
2.3	Rotor Design Table	74
2.4	Scale Drawing of Facility Test Section	75
2.5	Sketch of Four-Diaphragm Probe	76
2.6	Probe Calibration, Diaphragm 1	77
2.7	Probe Calibration, Diaphragm 3	78
2.8	Probe Calibration, Diaphragm 4	79
2.9	Probe Data Reduction Flow Chart	80
2.10	Probe Pitch Angle Sensitivity	81
2.11	Sketch of Miniature Stagnation Pressure Probe	82
2.12	Flow Chart for Digital Data Reduction	83
2.13	Time Resolved Total and Static Pressure Ratios, $r/r_t = 0.738$	84
2.14	Time Resolved Axial and Pitchwise Mach Number Components, $r/r_t = 0.738$	85
2.15	Time Resolved Radial Mach Number, $r/r_t = 0.738$	86
2.16	Time Resolved Total and Static Pressure Ratios, $r/r_t = 0.87$	87
2.17	Time Resolved Radial and Pitchwise Flow Angles, $r/r_t = 0.87$	88

-7-
LIST OF FIGURES (Continued)

<u>Figure</u>		<u>Page No.</u>
2.18	Time Resolved Axial and Pitchwise Mach Number Components, $r/r_t = 0.87$	89
2.19	Time Resolved Radial Mach Number, $r/r_t = 0.87$	90
2.20	Comparison of Miniature Stagnation Probe and Four-Diaphragm Probe Time Resolved Measurements, $r/r_t = 0.87$	91
2.21	Time Resolved Total Pressure and Temper- ature Ratios, $r/r_t = 0.738$	92
2.22	Rotor Average Performance, Pressure and Temperature Ratios	93
2.23	Rotor Average Performance, Exit Mach Number Components	94
2.24	Total Pressure Ratio Map, 0.1 Chords Downstream	95
2.25	Static Pressure Ratio Map, 0.1 Chords Downstream	96
2.26	Entropy Rise Map, 0.1 Chords Downstream	97
2.27	Axial Mach Number Map, 0.1 Chords Down- stream	98
2.28	Pitchwise Mach Number Map, 0.1 Chords Downstream	99

LIST OF FIGURES (Continued)

<u>Figure</u>		<u>Page No.</u>
2.29	Radial Mach Number Map, 0.1 Chords Downstream	100
2.30	Total Temperature Ratio Map, 0.1 Chords Downstream	101
2.31	Total Pressure Ratio Map, 1.0 Chords Downstream	102
2.32	Static Pressure Ratio Map, 1.0 Chords Downstream	103
2.33	Entropy Rise Map, 1.0 Chords Downstream	104
2.34	Axial Mach Number Map, 1.0 Chords Downstream	105
2.35	Pitchwise Mach Number Map, 1.0 Chords Downstream	106
2.36	Radial Mach Number Map, 1.0 Chords Downstream	107
2.37	Total Temperature Ratio Map, 1.0 Chords Downstream	108
3.1	Typical Shock Pattern for a Transonic Rotor	109
3.2	Side View of Compressor Rotor	109
3.3	Axial and Side Views of Computational Domain	110
3.4	Side View of Physical Domain	111

LIST OF FIGURES (Continued)

<u>Figure</u>		<u>Page No.</u>
3.5	Computed Rotor Pressure Ratio Profiles, Theta Averaged	112
3.6	Computed Incidence and Inlet Flow Angles, Theta Averaged	113
3.7	Computed Deviation and Exit Flow Angles, Theta Averaged	114
3.8	Computed Axial and Pitchwise Mach Number Profiles, Theta Averaged	115
3.9	Computed Mach Number Contours for $r/r_t = 1.0$	116
3.10	Computed Mach Number Contours for $r/r_t = 0.86$	117
3.11	Computed Mach Number Contours for $r/r_t = 0.75$	118
3.12	Computed Mach Number Contours for $r/r_t = 0.65$	119
3.13	Computed Pressure Coefficient for $r/r_t = 1.0$	120
3.14	Computed Pressure Coefficient for $r/r_t = 0.86$	121
3.15	Computed Pressure Coefficient for $r/r_t = 0.75$	122

-10-
LIST OF FIGURES (Continued)

<u>Figure</u>		<u>Page No.</u>
3.16	Computed Pressure Coefficient for $r/r_t = 0.65$	123
3.17	Computed Blade to Blade Stream Surfaces	124
3.18	Computed S2 Surfaces	125
4.1	Image Plane Positions	126
4.2	Visualized Density at $r/r_t = 0.88$	127
4.3	Computed Density at $r/r_t = 0.88$	128
4.4	Visualized Density at $r/r_t = 0.83$	129
4.5	Computed Density at $r/r_t = 0.83$	130
4.6	Visualized Density at $r/r_t = 0.80$	131
4.7	Computed Density at $r/r_t = 0.80$	132
4.8	Visualized Density at $r/r_t = 0.70$	133
4.9	Computed Density at $r/r_t = 0.70$	134
4.10	Visualized Density at $r/r_t = 0.65$	135
4.11	Computed Density at $r/r_t = 0.65$	136
4.12	Rotor Total and Static Pressure Ratios, Theta Averaged	137
4.13	Computed Total Pressure Map	138
4.14	Computed Static Pressure Map	139
4.15	Rotor Exit Air Angles, Theta Averaged	140
4.16	Computed Velocity Components at $r/r_t = 0.75$	141

LIST OF FIGURES (Continued)

<u>Figure</u>		<u>Page No.</u>
4.17	Computed Velocity Components at $r/r_t = 0.86$	142
4.18	Time Resolved Mach Number Components at $r/r_t = 0.845$	143
4.19	Time Resolved Mach Number Components at $r/r_t = 0.845$	144
4.20	Rotor Axial and Pitchwise Mach Number Profiles, Theta Averaged	145

CHAPTER I

INTRODUCTION

Improving the efficiency of modern transonic axial flow compressors is an area of increasing research effort because of a need to reduce gas turbine fuel consumption while also reducing engine weight. The best current compressor stages operate with moderately supersonic tip speeds and have total pressure ratios of 1.6 or higher with efficiencies approaching 90 percent. Only 3 or 4 percent of the inefficiency is fundamental in the sense of being directly related to frictional drag on the compressor blades; the remainder being determined by other loss mechanisms lumped under "secondary flows". Minimizing blade frictional losses and secondary flow losses will require experimental and theoretical methods which can resolve not only average flow properties but also the details of the complex three dimensional flows present in these machines.

Design of efficient stages has been retarded by a lack of adequate time resolved flow measurements downstream of high tip speed rotors. Time resolved, three dimensional measurements have been obtained only for low speed stages, for example reference (1). Some time resolved total pressure measurements for high speed stages, reference (2), have been reported, but measurements of a single flow quantity provides little information on detailed aerodynamics and flow mechanisms. One goal of the present investigation is to provide time resolved measurements of total and static

pressures, radial flow angles, and tangential flow angles downstream of a representative high speed, highly loaded compressor rotor. Measurements were taken for an isolated compressor rotor which has a tip Mach number of 1.2, a total pressure ratio of 1.65, a two foot overall diameter, and an inlet hub/tip ratio of 0.5.

A critical evaluation of the experimental data taken requires that the expected rotor through-flow be calculated as accurately as possible. Recent advances in digital computer processor speed and numerical methods have made it possible to compute flow solutions for the complex blade geometries found in turbomachinery. A fully three dimensional inviscid solution for the rotor through-flow was calculated to compare against the experimental data. This solution was computed using MacCormack's time-marching finite difference method which yields second order accurate solutions. By comparing the numerical solution to the experimental flow measurements, a much clearer understanding of the rotor aerodynamics and the importance of viscous phenomena in determining the rotor through-flow can be obtained than could be gotten by using only the experimental results.

During this investigation a flow visualization study of the intra-blade density for the test rotor was reported by Epstein, reference (3). This study provided instantaneous static density measurements on several axial planes through the rotor blade passage. The availability of the three dimensional instantaneous density measurements and the three dimensional numerical computation

-14-

for the same geometry provides a unique chance to evaluate the accuracy of the numerical computation. A comparison of the measured intra-blade density to the computed density field and an evaluation of the inviscid numerical computation's potential as a design tool are important portions of this research work.

CHAPTER II

EXPERIMENTAL MEASUREMENTS

2.1 Test Facility

A detailed time resolved study of the flow upstream and downstream of a high work compressor rotor has been conducted. During this study, measurements of total pressure, static pressure, radial flow angle, and pitchwise flow angle were obtained on the blade passing scale in several radial planes. It is the purpose of this section to describe the experimental facilities and instrumentation utilized, the data recording and data processing techniques used and the basic flow field data obtained.

The experiments were conducted in the M.I.T. Blowdown Compressor Facility which is described in reference (4), but because of the facility's unique nature it will be described in some detail here. This facility allows the testing of full scale high speed compressor rotors with modest expenditures of money and power. These savings are accomplished by testing a rotor in a pulsed mode rather than the conventional steady state mode. Such a procedure can be successful since most important aerodynamic phenomena have time scales of at most a rotor rotation period. For example, the flow time through the test rotor is approximately 1/20 of the rotor rotation period. Thus if steady state conditions can be provided for a few rotor rotation periods most relevant aerodynamic data can be collected.

The necessary steady state test time is provided by the

Blowdown Compressor Facility in a manner somewhat analogous to a shock tube experiment. The facility, drawn to scale in Figure 2.1, consists of a supply tank separated by a diaphragm from a test section and a dump tank into which the compressor exhausts. An experiment is performed by bringing the rotor up to speed in a vacuum, breaking the diaphragm and allowing a test gas to flow through the compressor. The gas flow rate is controlled by a choked discharge orifice so that a constant exit axial Mach number is maintained. During a test the rotor is driven only by its own inertia and therefore slows down as it does work on the test gas. Since the supply tank acoustic period is small compared to its blowdown time, the supply tank acts not like a shock tube driver but as a stagnation plenum whose pressure and temperature decrease with time. By proper selection of the initial supply tank pressure, which controls the power taken out of the rotor, the rotor's rate of deceleration can be matched to the plenum temperature's rate of decrease such that the rotor tip Mach number remains constant with time.

Under the conditions of constant exit Mach number and constant tip Mach number, the rotor non-dimensional performance parameters, P/P_{t2} for example, will remain constant on the blade passing time scale. This assertion will be true if the flow-through time is short compared to the blowdown period. For the blowdown facility this ratio is about 1/100. To illustrate the absolute time scales of interest during a blowdown test, typical facility parameters are

shown in Figure 2.2. The blowdown test lasts about 0.2 seconds, while the steady state test time lasts about 40 milliseconds. The test time begins at about 75 milliseconds. The comparison between the plenum temperature and the rotor speed squared shows that the rotor tip Mach number remained at 1.2, its initial value, throughout the test. The typical position of a radial traversing probe during a test is also shown. The initial blade passing frequency is 3.5 KHz.

In contrast to the blowdown tunnel design, the test rotor is of conventional design for a high speed, high work compressor rotor. The design of the rotor was also described in reference (4). Some highlights of the design are a total pressure ratio of 1.6, tip Mach number of 1.2, an inlet hub/tip ratio of 0.5, an exit hub/tip ratio of 0.64, and an inlet axial Mach number of 0.5. A summary of rotor design information is shown in Figure 2.3.

Double circular arc blade sections were used for the subsonic portion of the span; while, multiple circular arc blade sections were used for the supersonic portion. The rotor has 23 blades.

Figure 2.4 is a scale drawing of the facility test section and rotor flow path. The axial location of the various instrumentation ports is also noted. Port 4 and port 5 are immediately upstream and downstream of the rotor respectively. The axial spacing of the ports is about one axial chord length. The figure shows that the outer casing is cylindrical and that all the flow path convergence is taken on the inner casing.

2.2 Instrumentation

Supply tank, test section, and dump tank pressures were measured using conventional strain-gauge transducers having frequency response flat to 1 KHz. These transducers also have extremely good stability. The rotor speed is found from a magnetic pickup adjacent to a 115 tooth gear on the rotor shaft.

Time resolved measurements of the fluctuating pressures behind the compressor rotor were determined using probes based on the miniature silicon-bonded transducers produced by the Kulite Corporation. These transducers have frequency response flat from DC to 100 KHz and their diameter is 0.058 inches. Probes which can be used to resolve highly unsteady three dimensional flow fields can be produced by combining several of these diaphragms into one probe body. The probe design used in these experiments is shown in schematic form in Figure 2.5. Four transducers were mounted on flats on a cylindrical body to construct this probe. One transducer faces the mean flow direction while the remainder are inclined at 45 degrees to the mean flow direction. During a compressor test the probe is traversed radially inward with transducer number 1 perpendicular to the mean flow direction.

The fraction of the free stream dynamic pressure recovered at each transducer location is primarily a function of radial and pitchwise flow angles. Dynamic pressure recovery is influenced to a much lesser degree by Mach number and Reynolds number. The pressure recovery measured at each transducer location during

steady state testing is shown in Figures 2.6, 2.7, and 2.8 for several combinations of flow angles. The recovery measured for transducer number 2, which is not shown, is identical to that of transducer number 3, if the sign of θ is reversed. During a compressor test, the transducers are referenced to vacuum and indicate absolute pressure.

The effect of Mach number and Reynolds number variation on the probe calibrations were determined in steady state model testing. The range of Mach number simulated was 0.25 to 0.55; the range of Reynolds number simulated was 0.8×10^4 to 3×10^4 , based on probe diameter. The effect of changing Mach number and Reynolds number over these ranges was small for angle variations of ± 15 degrees. For larger angle variations, the effects of Mach number and Reynolds number are expected to be much stronger.

The physical dimensions of the traversing probe limit the spatial resolution that may be achieved. For the rotor tested the pitchwise distance between transducers is about 3% of blade spacing at the hub; while, in the radial direction the maximum distance between transducers is about 5% of the blade span. Large flow gradients could not be reliably determined over distances smaller than these.

It should be noted that the transducers are mounted on the probe body without any surrounding cavities. In this way the full frequency response of the transducers is retained. However the flow time across these transducers limits the probe response to about 10

times blade passing frequency, which is sufficient to resolve events occurring in the blade passing time scale.

One of the most important aspects of using the kulite diaphragms to measure absolute pressures is their proper calibration. In the Blowdown Compressor Facility, they are calibrated after each test during venting of the facility to atmospheric pressure. During this transient, the response of the low and high frequency response transducers is recorded. The kulite gages are calibrated by comparing their response to known response of the low frequency transducers.

The flow variables can be determined from the measured pressures using an iterative procedure for which a flow chart is shown in Figure 2.9. First, a guess of the total pressure is made. Values of the static pressure, radial flow angle (ϕ), and pitchwise flow angle (θ) are found using relationships like that illustrated in Figure 2.10 which are determined from the diaphragm recovery curves, Figures 2.7 and 2.8. These relationships express the effect of the flow angles on the recovery of diaphragm numbers 2, 3 and 4. A new value of the total pressure is calculated using Figure 2.6 which expresses the flow angle effect on the recovery of diaphragm number 1. If the new total pressure value differs from the guessed value by more than 0.5%, a new total pressure guess is made and the iteration repeated until the guessed and calculated values are sufficiently close.

When the flow angles are within ± 15 degrees and the Mach number not near 1.0, the flow angle measurements are accurate within

± 1 degree and the total pressure measurements are accurate within 2%. As the flow angles increase to 20 degrees, the accuracy decreases slowly. Beyond 20 degrees, one of the diaphragms seems to be located in a separated flow region and the accuracy decreases rapidly.

A second type of high response probe used was a miniature stagnation probe, sketched in Figure 2.11. This probe consists of a kulite diaphragm mounted inside a small impact tube. Earlier testing, reference (4) indicated that such a probe would be insensitive to angle variations of ± 15 degrees and have a frequency response flat to 30 KHz. Similar probes have been used, references (2) and (5), for unsteady pressure measurements in compressors with both subsonic and supersonic axial flow.

Both of these probes are mounted on radial traversing mechanisms, which allows the probe to survey the entire span within the steady state test time of 40 milliseconds. Since the rotor pressure distribution is swept past the traversing probes much faster than the probes are moved radially, a complete map of the flow field in one radial plane can be determined in one test run.

2.3 Data Recording and Data Reduction

During an experiment, test data is recorded on a fourteen channel FM tape recorder. This machine is an Ampex Corporation model FR-1900 recorder which allows recording of FM analog signals having frequencies from DC to 80 KHz. One channel of the recorder is reserved for a 200 KHz crystal oscillator which provides an

absolute time base for the experiment and subsequent data analysis. The recorder playback speed may be reduced by up to a factor of 64 to facilitate data analysis. The signal to noise ratio achieved using the recorder is 40 dB.

Analysis of the high response data collected is made practical by analog-to-digital conversion (ADC) and then performing data analysis on a digital computer. A flow chart of the data processing scheme is shown in Figure 2.12. The initial step of ADC is done using the ADAGE Computer available from the Electronic Systems Laboratory at MIT. The ADC process is described in detail in reference (6). Only a modest ADC rate is possible on the ADAGE, this fact requires that the analog tape playback speed be reduced by its maximum factor of 64. Tape recorder flutter compensation and low pass filtering are included in the ADC step.

The output of the ADC step is a digital format tape which contains one tape file for each of the original analog tape channels. The recorded 200 KHz oscillator is used as a trigger which allows sampling at a sufficient rate and establishes a very accurate real time for each digital sample.

Further data processing was done on the IBM 370/168 available at the Information Processing Center at M.I.T. During the reformatting and compaction steps, the quantity of data to be processed is reduced to cover only time periods of interest and voltage values are converted from their Adage binary format to their decimal values. An elapsed time indicator is assigned to each data sample as well as

a key which is unique for each analog tape recorder channel. The output of this intermediate processing step is also stored on magnetic tape. These values are then retrieved, converted to pressures, and stored on direct access devices for random retrieval by data reduction programs.

Data reduction programs perform several plotting functions as well as reducing the four diaphragm probe measurements to pressures, flow angles and Mach number components. Other functions of the programs include total temperature and entropy rise calculations, mass flow calculation, and time and mass flow averaging of flow variables.

2.4 Basic Flow Field Data

Measurements typical of those taken using the four diaphragm probe located 0.1 axial chords downstream of the rotor and at an r/r_t of 0.74 are shown in Figures 2.13, 2.14, and 2.15. Figure 2.13 shows the local total pressure ratio (P_{t2}/P_{t1}) and static pressure ratio (P_{s2}/P_{t1}). Figures 2.14 and 2.15 show the Mach number components computed from the pressures plus the measured flow angles. As time increases in these plots, the rotor turns such that the probe appears to move from the suction side of one blade to the pressure side of the adjacent blade.

Figure 2.14 shows, at least qualitatively, the velocity profile expected for a rotor wake when observed from a stationary reference frame. That is, the wake has an axial velocity defect and an excess of pitchwise or tangential velocity. Figure 2.13 shows that there

is a large total pressure defect associated with the wake and that the static pressure is not uniform across the wake, in fact it varies by as much as plus and minus 25 percent. Close scrutiny of Figure 2.13 shows that the minimum static pressure occurs on the pressure side of the wake; while, the maximum static pressure occurs on the suction side of the wake. These wakes are highly curved toward the pressure side of the blade in both the absolute and relative reference frames, and the static pressure gradient appears to be consistent with this streamline curvature. Large outward radial Mach numbers (up to 0.25) can be seen from Figure 2.15 to exist at the tangential location of minimum static pressure, i.e. on the pressure side of the wake. Across the wake, the radial Mach number decreases by approximately 0.25. An area of radial inflow also appears at around mid-gap.

These data are typical of data recorded for $r/r_t < 0.80$ in that the flow is periodic at blade passing period or the flow is steady in rotor coordinates.

Data recorded when the four diaphragm probe was located at $r/r_t = 0.87$ are shown in Figures 2.16 through 2.19. These data are representative of results obtained at large r/r_t . In Figure 2.16 the flow is shown to have large blade to blade variations; also, the blade wakes appear as areas of high total pressure rather than low total pressure as was the case at small radius ratio. Some local areas of total pressure ratio as high as 2.10 exist.

The large variations in the flow angles found at this radius

are shown in Figure 2.17. In a few of the time samples, the flow angles relative to the probe exceed the range of good probe accuracy. Pitchwise angles larger than 65 degrees or smaller than 25 degrees as well as radial angles of ± 20 degrees fall outside this range. The flow angle variations encountered at this radius are perhaps the most extreme encountered during the compressor testing but the vast majority of the data does fall within the range of good probe resolution.

The calculated Mach number components are shown in Figures 2.18 and 2.19. These data again show the large blade to blade variations at this radius; some blade passages appear severely stalled while others produce almost no blade wake.

By examining the wake shed by a single blade during successive passes at a constant r/r_t , it was found that the flow is quite unsteady in rotor coordinates for $r/r_t > 0.80$. Evidence of an unsteady separation process at $r/r_t > 0.83$ has also been found by Epstein in reference (3) using a fluorescent density measurement technique.

Figure 2.20 shows a comparison between the four diaphragm probe total pressure measurements and measurements made using the miniature total pressure probe. These data are from the same radial location, $r/r_t = 0.87$, but are from different test runs so they should not be expected to be identical. The level of total pressure appears to be the same as well as the range of pressure ratio, up to 2.10. In addition the shape of the local spikes in pressure appear

approximately the same.

In order to determine the distribution of work input and losses, a calculation of the local total temperature ratio was attempted. The temperature ratio was calculated using Euler's Turbine Equation as applied to a streamtube.

$$\frac{T_{t2}}{T_{t1}} = 1 + \frac{\omega r V_{\theta 2}}{C_p T_{t1}} \quad (2.1)$$

This form of the equation is valid for streamtubes in which the flow is steady in a coordinate system relative to the rotor. If we consider the instantaneous temperature ratio, the unsteady effect of the blowdown can be neglected; however, as was shown in the last section some portions of the flow are unsteady on a blade passing time scale. For such streamtubes the computed temperature ratios could be substantially in error, and this should be kept in mind when interpreting the following results.

Introducing convenient non-dimensional variables into Euler's equation yields:

$$\frac{T_{t2}}{T_{t1}} = 1 + (M_T)(\gamma-1)(r/r_t)M_{\theta 2}\left(1 + \frac{\gamma-1}{2}M^2\right)^{-\frac{1}{2}}(T_{t2}/T_{t1})^{\frac{1}{2}} \quad (2.2)$$

where M_T = rotor tip Mach number based on T_{t1} .

From the local total pressure and temperature, the local entropy rise across the blade row can be calculated.

$$\frac{\Delta s}{C_v} = \ln((P_{t2}/P_{t1})^{-(\gamma-1)}(T_{t2}/T_{t1})^{\gamma}) \quad (2.3)$$

Figure 2.21 shows the total temperature ratios and the total pressure ratios for $r/r_t = 0.738$. Here we see that the most work addition has occurred in the wakes. The observed wake total pressures

and total temperatures are generally consistent with the wake behavior discussed in reference (7).

If the local pressure, temperature, and Mach number are known throughout a radial plane behind the compressor rotor, the integral performance of this rotor can be calculated. For example the total mass flow:

$$\dot{m} = \iint \rho V_z r dr d\theta \quad (2.4)$$

rewritten in terms of convenient variables thus yields:

$$\dot{m} = \frac{\gamma P_o r_t^2}{a_o} \iint \left\{ (P_2/P_1) [(T_{t2}/T_{t1}) (1 + \frac{\gamma-1}{2} M^2)]^{-\frac{1}{\gamma}} M_z \right\} \frac{r}{r_t} \frac{d(r)}{r_t} d\theta \quad (2.5)$$

where the quantities inside the integral are the measured non-dimensional performance variables and $\frac{P_o}{a_o}$ are arbitrary reservoir conditions.

The compressor mass flow computed by this method is 14.2 Kg/sec at $t = 0.1$ seconds in the blowdown. Mass averaged flow quantities, such as total pressure ratio and total temperature ratio, can be determined by similar means:

$$(P_{t2}/P_{t1})_{av} = \frac{1}{\dot{m}} \iint (\rho V_z) (P_{t2}/P_{t1}) r dr d\theta \quad (2.6)$$

The mass averaged total pressure ratio at station 5 was 1.646; the mass averaged total temperature ratio was 1.158.

The mass averaged total temperature rise may also be calculated by using the known deceleration rate for the rotor

$$T_{t2} - T_{t1} = \frac{P_s}{C_{pm} \dot{m}} = \frac{I\omega}{C_{pm} \dot{m}} \frac{d\omega}{dt} \quad (2.7)$$

where P_s = the power being taken out of the rotor, and I = moment of

inertia of the rotor.

$$P_s = 264 \text{ KW} \quad \text{at } t = 0.1 \text{ seconds}$$

Using the mass flow previously determined, the total temperature ratio may be calculated and is found to be 1.154. This value compares very favorably to the calculated value of 1.158.

These two total temperature calculations are not strictly independent since the calculated local temperature was used in the mass flow calculation, see equation (2.5). However, the total temperature ratio appears to the 1/2 power; further, as can be seen from Figure 2.21, the temperature ratio is nearly constant outside the blade wakes. Thus it can be said that the local temperature calculated from the Euler equation seems to give a very realistic evaluation of the work input to the flow.

Mass flow averages at a constant radius were computed for several flow variables and are illustrated in Figures 2.22 and 2.23. These averages were computed from time samples five blade passing periods in length. Figure 2.22 shows the total pressure and temperature ratio. Here we see that the total temperature rather closely approaches the overall average value of about 1.16 except at the rotor tip. At the tip, substantial extra work input is found which is a typical result for compressor rotors of this design. Also the temperature determined at the different axial stations match closely.

There is, however, a systematic difference between the total pressures at stations 5 and 6 which corresponds to approximately a 4 percent decrease in efficiency, based on the average pressure and

temperature. When the relative reference frame total pressure is calculated from the mass flow averaged quantities, it is found to decrease by 3 percent from upstream of the rotor to port 5. This decrease while small compares well with the level of total pressure loss normally measured for cascades, see reference (8). At this measurement plane, most of the total pressure loss associated with wake mixing and secondary flows has not occurred. The rotor isentropic efficiency at port 5 is 97 percent, but the efficiency is reduced to 93 percent at port 6 by wake mixing and secondary flow losses.

Average pitchwise and axial Mach number profiles are shown in Figure 2.23. Considerable deviations from the design profiles exist and are especially important at larger r/r_t . The average radial Mach number was nearly zero.

Whenever high response data is collected, a serious problem arises in assimilating the quantity of data recorded. One way to overcome this problem is to construct level curves or contour plots of flow variables in an $r-\theta$ plane. Data samples recorded at several radial positions and approximately 3 blade passing periods in length were selected. The samples were all chosen to begin at the same relative time in a blade passing period. A data point in these samples then corresponds to a point in a sector of the $r-\theta$ plane including 3 blade passages.

A contour plot of the rotor total pressure ratio in the radial plane 0.1 chords downstream of the rotor is shown in Figure 2.24. In this plot data from 10 radial positions were used. The starting

points of the data samples were selected such that the blades are located at 0.0, 1.0, 2.0, and 3.0. At small r/r_t the flow field can be seen to have nearly constant total pressure except near the blade wakes. Near midspan, islands of high pressure appear in the core flow as well as near the wakes. At large r/r_t numerous islands of high and low pressure are scattered throughout the flow field. Here again it can be seen that at small r/r_t the wakes in general have a total pressure defect while at large r/r_t the wakes have an excess of total pressure.

It should be emphasized that these data are in a sense taken out of context since data from several different blades at different times are combined into a single plot. As was previously discussed, unsteadiness does exist and is important at larger radii; therefore, some distortion and loss of detail in these contour plots is inevitable. However, flow features common to all blades will be emphasized by this procedure.

A contour plot of the rotor static pressure ratio (P_{s2}/P_{t1}) is shown in Figure 2.25. Many interesting features appear in this plot; in particular the high static pressure area at about midspan and the localized high-gradient low-pressure areas. No convincing explanation for the origin of the areas is yet known; however, the existence of these areas is supported by the intra-blade density measurements of reference (3) previously noted.

A contour plot of the entropy rise $(s_2 - s_1)/C_v$, is shown in Figure 2.26. The entropy rise was determined from the measured total

pressure and the calculated total temperature. At small r/r_t the flow appears to be very nearly isentropic except for the wakes. Above midspan isolated regions of high entropy appear.

Contour maps of the axial Mach number, pitchwise Mach number, radial Mach number, and total temperature ratio are included as Figures 2.27 through 2.30 for later reference. These data all appear to be self-consistent. For example, large radial flows are directed away from the high static pressure areas at about midspan. In addition, these data all have large disturbances concentrated at blade passing frequency.

Similar sets of contour plots were prepared from radial surveys done further downstream of the rotor. Maps constructed from a traverse 1.0 axial chord downstream are shown in Figures 2.31 through 2.37. These figures show that considerable evolution of the flow field occurs in one axial chord. In particular, considerable decay of the disturbances introduced by the rotor has occurred at smaller r/r_t , while at larger r/r_t the disturbances seem to have propagated without significant decay. In addition, the main disturbance frequency for $r/r_t > 0.82$ is significantly lower than the blade passing frequency; the fundamental disturbance at these radii appears to be about 1.4 times blade passing frequency. The flow field in this outer section is similar to a cellular vortex flow of the type which occurs between coaxial rotating cylinders under some conditions of radial circulation variation. In Figures 2.35 and 2.36, zones of large inward and outward flow exist, together with

alternate large and small pitchwise or tangential velocity.

The evolution of the flow field from port 5 to port 6 is largely explained by the effect of the mean swirl velocity profile, or pitchwise velocity, on the blade wakes. These effects have been extensively discussed in general and for the test rotor swirl profile by Kerrebrock (9, 10). It was shown that in the inner portion of the annulus, $r/r_t < 0.82$, shear disturbances or wakes should be attenuated with increasing distance from the rotor; in this section of the annulus, the swirl velocity profile can be approximated as a free vortex. In the outer annulus section, for which the swirl velocity profile can be approximated as a solid body rotation, shear disturbances should be persistent or oscillatory in the downstream flow. These persistent disturbances are similar in nature to well known inertial waves. It was also argued in reference (10), at least in a qualitative sense, that the first mode of a stable shear disturbance field in the outer annulus would have a fundamental frequency which is about 1.4 times the blade passing frequency. This shear mode would have a tangential mode number, m , of approximately 16; a disturbance at blade passing frequency would have a mode number of $m = 23$. Regardless of the mean swirl profile, entropy disturbances should be convected by the mean flow. These predictions are all consistent with the flow field summary maps, Figures 2.32 through 2.36.

Measurements of the upstream sound pressure field for this same rotor, reference (11), showed that a well developed duct modal

structure exists which has dominant tones at mode numbers of $m = 7$ and $m = 16$. This sound field was typical of the combination tone field of a transonic fan. It now seems clear that the $m = 16$ tone is excited by the cellular flow in the downstream annulus. The $m = 7$ tone may be a combination tone of $m = 23$ and $m = 16$ disturbances.

NUMERICAL METHODS

3.1 Introduction

The rotor for which the experimental measurements were taken is highly loaded, has a low hub-to-tip ratio, and has transonic inlet Mach numbers. These facts dictate that a successful computation of the flow field must be fully three dimensional and must be capable of handling mixed subsonic and supersonic flows. Even though the results of Chapter II indicate the viscous blade wakes to have an important influence on the complete flow, the calculations in this section will be conducted for an inviscid non-heat conducting fluid, as the computation of general high speed viscous flows remains well beyond the range of current computational methods and computer hardware. The inviscid solution will be compared to the experimental measurements taken downstream of the rotor and to the intra-blade density measurements reported by Epstein in reference (3). These comparisons should provide unique information on the accuracy and suitability of inviscid flow analysis when applied to turbomachine aerodynamics. The comparisons should also provide a much better understanding of the influence of viscosity on the rotor through-flow. A three dimensional inviscid calculation also has considerable importance as an essential first step toward computing the complete rotor flow field by adding a boundary layer analysis to the inviscid computation.

The computational task is complicated by the appearance of

shock waves both inside the rotor passage and upstream of the rotor. A typical flow pattern for a transonic cascade is illustrated by Figure 3.1. A strong passage shock originates at the leading edge of one blade and terminates on the suction side of the adjacent blade. A weak oblique shock stands in front of the cascade. The position and strength of these shocks must be determined as part of the computational solution.

The development of computational procedures suitable for the solution of this complex flow problem was begun by Oliver and Sparis, references (12) and (13). These authors used MacCormack's time-marching method to solve a variety of two and three dimensional steady transonic flow problems. They also found a three dimensional solution for the test rotor geometry in the lightly loaded case. This solution was presented in reference (13). Using as a base the lightly loaded case, the procedures of reference (13) have been refined and extended to compute a solution for the highly loaded "design" case. In the next sections, the basic computational procedures and the results of the highly loaded calculation will be described.

3.2 Numerical Procedures

The computational problem is specified by the partial differential equations, the domain over which the solution is desired and the boundary conditions to be satisfied. The differential equations are:

the continuity equation

$$\frac{\partial \rho}{\partial t} + \nabla \cdot (\rho \bar{V}) = 0$$

and the inviscid momentum equations

$$\frac{D\bar{V}}{Dt} = - \frac{1}{\rho} \nabla P$$

Since shock waves appearing in the flow were expected to be weak, the energy equation was replaced by an isentropic flow assumption

$$P/P_0 = (\rho/\rho_0)^\gamma$$

The boundary condition to be satisfied on the blade surfaces is that the flow be tangent to the blade. The implementation of this condition is greatly simplified if the problem is solved in a reference frame rotating with the rotor. This boundary condition becomes $\bar{n} \cdot \bar{V}_{rel} = 0$ where \bar{n} is a unit vector normal to blade and \bar{V}_{rel} is the velocity in the rotating reference frame. The governing equations are then

$$\frac{\partial \rho}{\partial t} + \nabla \cdot (\rho \bar{V}_{rel}) = 0$$

$$\frac{D \bar{V}_{rel}}{Dt} + 2\bar{\Omega} \times \bar{V}_{rel} = - \frac{1}{\rho} \nabla p + \bar{\Omega} \times (\bar{\Omega} \times \bar{r})$$

where

$$\bar{V}_{rel} = \bar{V}_{abs} - \bar{\Omega} \times \bar{r} \quad \text{and} \quad \bar{\Omega} = \Omega \hat{f}_z$$

These equations when written in matrix form for a cylindrical coordinate system become

$$\frac{\partial U}{\partial t} + \frac{\partial F}{\partial r} + \frac{\partial G}{\partial \theta} + \frac{\partial H}{\partial z} = K \quad (3.1)$$

where

$$U = \begin{bmatrix} r\rho \\ r\rho u \\ r\rho v_{abs} \\ r\rho w \end{bmatrix} \quad F = \begin{bmatrix} r\rho u \\ r(\rho u^2 + p) \\ r\rho uv_{abs} \\ r\rho uw \end{bmatrix} \quad K = \begin{bmatrix} 0 \\ \rho v_{abs} + p \\ -\rho uv_{abs} \\ 0 \end{bmatrix}$$

$$H = \begin{bmatrix} r\rho w \\ r\rho uw \\ r\rho v_{abs} w \\ r(\rho w^2 + p) \end{bmatrix} \quad G = \begin{bmatrix} \rho(v_{abs} - \Omega r) \\ \rho u(v_{abs} - \Omega r) \\ \rho v_{abs}(v_{abs} - \Omega r) + p \\ \rho w(v_{abs} - \Omega r) \end{bmatrix}$$

The equations are non-dimensionalized using the new variables

$$\rho' = \frac{\rho}{\rho_0} \quad t' = \frac{tc_0}{L} \quad p' = \frac{p}{\rho_0 c_0^2} = \frac{\rho' \gamma}{\gamma}$$

The non-dimensional equations are then

$$\frac{\partial U'}{\partial t'} + \frac{\partial F'}{\partial r'} + \frac{\partial G'}{\partial \theta'} + \frac{\partial H'}{\partial z'} = K' \quad (3.2)$$

$$\begin{aligned}
 U' &= \begin{bmatrix} r'\rho' \\ r'\rho'u' \\ r'\rho'v'_{abs} \\ r'\rho'w' \end{bmatrix} & F' &= \begin{bmatrix} r'\rho'u' \\ r'(\rho'u'^2 + \frac{\rho'\gamma}{\gamma}) \\ r'\rho'v'_{abs} \\ r'\rho'w' \end{bmatrix} & K' &= \begin{bmatrix} 0 \\ \rho'v'^2_{abs} + \frac{\rho'\gamma}{\gamma} \\ r'\rho'u'v'_{abs} \\ 0 \end{bmatrix} \\
 H' &= \begin{bmatrix} r'\rho'w' \\ r'\rho'w'u' \\ r'\rho'w'v'_{abs} \\ r'(\rho'w'^2 + \frac{\rho'\gamma}{\gamma}) \end{bmatrix} & G' &= \begin{bmatrix} \rho'(v'_{rel}) \\ \rho'(v'_{rel})u' \\ \rho'(v'_{rel})v'_{abs} + \frac{\rho'\gamma}{\gamma} \\ \rho'(v'_{rel})w' \end{bmatrix}
 \end{aligned}$$

The prime superscripts will be dropped in all following sections.

The physical flow domain is illustrated by Figure 3.2 which shows the blade passages as seen by an observer looking radially inward. Some important geometric features are the blade twist and the 35 degree slope of the spinner and hub surface. The domain is bounded at the blade tips by a cylindrical hard wall. By symmetry, the domain is reduced to the blade passage bounded by the hub and tip casings and the suction and pressure surfaces of two adjacent blades.

This domain is transformed to one with a simple shape by a coordinate stretching which is detailed in reference (13). This procedure stretches the blade surfaces into untwisted planes and maps the hub surface onto the z axis. The stretched domain is shown in Figure 3.3. The equations describing this stretching follow below:

$$Z = z \quad \Theta = \frac{[\theta - \theta_u(r, Z)] \cdot \Delta\theta}{\theta_l(r, Z) - \theta_u(r, Z)}$$

$$R = \frac{r - r_h(Z)}{r_t - r_h(Z)} r_t$$

where $r_h(Z)$ = equation describing hub surface

r_t = radius of tip surface

$\theta_l(r,Z), \theta_u(r,Z)$ map out the pressure and suction surfaces of the blades

$$\Delta\theta = \frac{2\pi}{N} ; \quad N = \text{number of blade} = 23$$

The physical location of radial and axial coordinate grid lines are shown in Figure 3.4. There are 67 grid lines in the axial direction of which 31 are inside the rotor blade passage. There are 16 equally spaced grid lines in the radial direction and 12 equally spaced grid lines in the azimuthal direction.

The transformation to the stretched coordinate system modifies the basic equations. The Euler equations in the stretched domain become

$$\frac{\partial U}{\partial t} + \frac{\partial F}{\partial R} \frac{\partial R}{\partial r} + \frac{\partial H}{\partial R} \frac{\partial R}{\partial Z} + \frac{\partial F}{\partial \theta} \frac{\partial \theta}{\partial r} + \frac{\partial G}{\partial \theta} \frac{\partial \theta}{\partial \theta} + \frac{\partial H}{\partial \theta} \frac{\partial \theta}{\partial Z} + \frac{\partial H}{\partial Z} = K \quad (3.3)$$

Solutions to these equations were obtained at interior points using MacCormack's method. A good discussion of this method is given in reference (12). It is a two-step, explicit, second order accurate conditionally stable method. This method may be used to compute solutions to intrinsically unsteady flows or to compute asymptotically steady flows from initial conditions. Shock waves

which appear in the flow are resolved as regions of large gradients spread over 3 to 5 mesh points.

MacCormack's method is used in its split operation form for efficiency. A typical difference equation would appear as:

$$U_{j,k,1}^* = U_{j,k,1}^n - \frac{\delta t}{\delta Z} \Delta^+ H(U_{j,k,1}^n)$$

$$U_{j,k,1}^{n+1} = \frac{1}{2} [U_{j,k,1}^n + U_{j,k,1}^* - \frac{\delta t \Delta^-}{\delta Z} H(U_{j,k,1}^*)]$$
(3.4)

The addition of artificial viscosity terms was required to stabilize the solution along sonic surfaces and near blade leading and trailing edges. The form of the viscosity terms used is

$$V_{j,k,1}^{n+1} = \alpha \{ [|u_{j+1,k,1}^n - u_{j,k,1}^n| (U_{j+1,k,1}^* - \frac{U_{j,k,1}^{n+1} + U_{j,k,1}^n}{2})]$$

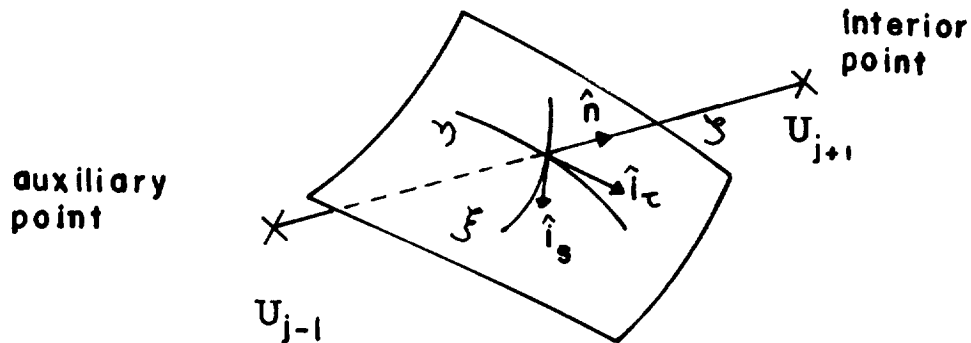
$$+ [|u_{j-1,k,1}^n - u_{j,k,1}^n| (U_{j-1,k,1}^* - \frac{U_{j,k,1}^{n+1} + U_{j,k,1}^n}{2})] \}$$
(3.5)

3.3 Boundary Conditions

At solid walls the boundary condition for inviscid flow, that the velocity normal to the wall be zero, must be applied. Adequate procedures exist for implementing this condition in supersonic flow and are generally based on the method of characteristics, see references (14) and (15). A variety of procedures are available for purely subsonic flow. For transonic flows, the implementation of

this condition with second order accuracy is difficult since simplifying assumptions usually cannot be made. Sparis (13) suggested a method which should be applicable in transonic flows when shock capturing schemes like MacCormack's method are used. In the next section this method will be reviewed and the proper equations for use in a rotating reference frame developed.

In this procedure the governing equations written in a body centered coordinate system are used to determine normal derivatives valid at the solid wall. The derivatives are used to evaluate a fluid state vector at an auxiliary point outside the computational domain. The fluid state on the boundary is then determined as if the boundary point were an interior point. The logical position of the auxiliary point is illustrated below.



At each point on this surface, an orthogonal curvilinear coordinate system consists of the local surface normal, \bar{n} , and two curves

in the surface, η and ξ . Differential arc lengths along each coordinate line are defined as:

$$ds = h_s d\xi$$

$$d\tau = h_\tau d\eta$$

$$dn = h_n d\zeta$$

The ζ coordinate line is taken to be a straight line and $h_n \equiv 1$.

The normal momentum equation in this coordinate system is

$$\frac{\partial u_n}{\partial t} + \frac{u_s}{h_s} \frac{\partial u_n}{\partial \xi} + \frac{u_\tau}{h_\tau} \frac{\partial u_n}{\partial \eta} + \frac{u_n}{h_n} \frac{\partial u_n}{\partial \zeta} + \frac{u_n u_s}{h_n h_s} \frac{\partial h_n}{\partial \xi} + \frac{u_\tau u_n}{h_\tau h_n} \frac{\partial h_n}{\partial \eta} \quad (3.6)$$

$$- \frac{u_s^2}{h_s h_n} \frac{\partial h_s}{\partial \zeta} - \frac{u_\tau^2}{h_\tau h_n} \frac{\partial h_\tau}{\partial \zeta} = - \frac{1}{\rho h_n} \frac{\partial p}{\partial \zeta} = \Omega^2 r (\hat{i}_r \cdot \bar{n}) - 2\Omega (\hat{i}_z \times \bar{v}_{rel}) \cdot \bar{n}$$

For simplicity the centrifugal and coriolis accelerations are expressed in terms of the base (r, θ, z) coordinate system. Since $u_n \equiv 0$ on the surface, this equation reduces to:

$$\rho \left[\frac{u_s^2}{h_s h_n} \frac{\partial h_s}{\partial \zeta} + \frac{u_\tau^2}{h_\tau h_n} \frac{\partial h_\tau}{\partial \zeta} \right] = \frac{1}{h_n} \frac{\partial p}{\partial \zeta} + \bar{n} \cdot [2\Omega (\hat{i}_z \times \bar{v}_{rel}) - \Omega^2 r \hat{i}_r]$$

Recognizing that $\frac{1}{h_s h_n} \frac{\partial h_s}{\partial \zeta} = \frac{1}{R_s}$ and $\frac{1}{h_\tau h_n} \frac{\partial h_\tau}{\partial \zeta} = \frac{1}{R_\tau}$ are the radii of

curvature of the surface along the ξ and η coordinate lines, this equation becomes

$$\frac{1}{a^2} \frac{\partial p}{\partial n} = \frac{\partial p}{\partial n} = \frac{\rho}{a^2} \left[\frac{u_s^2}{R_s} + \frac{u_\tau^2}{R_\tau} \right] - \frac{\bar{n} \cdot}{a^2} [2\Omega(\hat{i}_z \times \bar{v}_{rel}) - \Omega^2 r \hat{i}_r] \quad (3.7)$$

which is one of the desired normal derivatives.

Expressions for $\frac{\partial u_s}{\partial n}$ and $\frac{\partial u_\tau}{\partial n}$ can be determined most easily from the vorticity components. In the body centered coordinate system:

$$\begin{aligned} \omega_s &= \frac{1}{h_\tau h_n} \left[\frac{\partial(h_n u_n)}{\partial \eta} - \frac{\partial(h_\tau u_\tau)}{\partial \zeta} \right] \\ &= \frac{1}{h_\tau} \left[-h_\tau \frac{\partial u_\tau}{\partial \eta} - u_\tau \frac{\partial h_\tau}{\partial \eta} \right] \\ &= - \left[\frac{u_\tau}{R_\tau} + \frac{\partial u_\tau}{\partial n} \right] \end{aligned} \quad (3.8)$$

Also

$$\omega_\tau = \left[\frac{u_s}{R_s} + \frac{\partial u_s}{\partial n} \right] \quad (3.9)$$

For the highly loaded calculation, the flow is irrotational every-

where except downstream of the rotor and the vorticity components

are found from $\bar{\omega}_{rel} = \bar{\omega}_{abs} - 2\bar{\Omega} = -2\Omega \hat{i}_z$

If the fluid motion is not irrotational, the vorticity components

at the wall may be found by integrating Crocco's equation along a

particle path.

$$\frac{D(\bar{\omega}/\rho)}{Dt} = (\bar{\omega}/\rho \cdot \nabla) \bar{v} + \frac{1}{\rho} (\nabla T \times \nabla S)$$

An expression for u_n at the auxiliary point may be found by observing that:

$$(u_n)_{j+1} = (u_n)_j + \frac{\partial u_n}{\partial n} \delta n + \frac{\partial^2 u_n}{\partial n^2} \frac{\delta n^2}{2} + \frac{\partial^3 u_n}{\partial n^3} \frac{\delta n^3}{3!} + \mathcal{O}(\delta n^4)$$

$$(u_n)_{j-1} = (u_n)_j + \frac{\partial u_n}{\partial n} \delta n + \frac{\partial^2 u_n}{\partial n^2} \frac{\delta n^2}{2} + \frac{\partial^3 u_n}{\partial n^3} \frac{\delta n^3}{3!} + \mathcal{O}(\delta n^4)$$

Adding these equations and using the fact that $u_n = 0$ yields:

$$(u_n)_{j-1} = (u_n)_{j+1} + \frac{\partial^2 u_n}{\partial n^2} \delta n^2 + \mathcal{O}(\delta n^4)$$

As Sparis (13) pointed out, a second order accurate value of $(u_n)_{j-1}$ can be found if $\frac{\partial^2 u_n}{\partial n^2}$ can be evaluated with first order accuracy.

An expression for $\frac{\partial^2 u_n}{\partial n^2}$ can be found from the continuity equation

$$\frac{\partial \rho}{\partial t} + \frac{1}{h_s h_n h_\tau} \left[\frac{\partial}{\partial \xi} (h_\tau h_n u_s \rho) + \frac{\partial}{\partial \eta} (h_s h_n u_\tau \rho) + \frac{\partial}{\partial \zeta} (h_s h_\tau u_n \rho) \right] = 0$$

which reduces to

$$\frac{\partial \rho}{\partial t} + \frac{\partial}{\partial s} (\rho u_s) + \frac{\rho u_s}{R_\xi} + \frac{\partial}{\partial \tau} (\rho u_\tau) + \frac{\rho u_\tau}{R_\eta} + \frac{\partial}{\partial n} (\rho u_n) = 0$$

After taking $\frac{\partial}{\partial n}$ and defining $\frac{1}{h_s h_\tau} \frac{\partial h_\tau}{\partial \xi} = \frac{1}{R_\xi}$ and $\frac{1}{h_s h_\tau} \frac{\partial h_s}{\partial \eta} = \frac{1}{R_\tau}$

$$\rho \frac{\partial^2 u_n}{\partial n^2} + \frac{\partial \rho}{\partial n} \frac{\partial u_n}{\partial n} = - \frac{\partial^2 \rho}{\partial n \partial t} - \frac{\partial^2 (\rho u_s)}{\partial s \partial n} - \frac{\partial^2 (\rho u_\tau)}{\partial \tau \partial n} - \frac{\partial}{\partial n} \left[\frac{(\rho u_s)}{R_\xi} + \frac{(\rho u_\tau)}{R_\eta} \right] \quad (3.10)$$

$\frac{\partial^2 u_n}{\partial n^2}$ can always be evaluated with first order accuracy by using one-sided time and normal derivatives. For transonic irrotational flow, all terms in this equation are at most the order of $\frac{M_{rel}}{R}$, see equations 3.7 and 3.8. Then $(u_n)_{j-1} = -(u_n)_{j+1} + \frac{(\delta n^2)}{R} + (\delta n^4)$

When the surface characteristic radius of curvature is large, $(u_n)_{j-1} = (u_n)_{j+1}$ will be a second order accurate approximation. For the thin, circular arc blades used for the test rotor, the approximation is adequate. These equations complete the relations needed to implement the solid-wall boundary conditions.

The upstream and downstream boundary conditions are among the most important conditions determining the solution. They, along with the initial conditions, determine if a steady or unsteady solution is reached, the rotor pressure rise and the mass flow rate. Unfortunately, the nature and number of conditions necessary for a well posed problem is not known for sets of non-linear equations of mixed type. We must therefore be guided by experience and intuition in formulating these conditions for practical calculations.

Boundary conditions used in the highly loaded blade case were derived using the following model. As can be seen from Figure 3.4, the upstream and downstream boundaries are rather far from the rotor, about 3 chord lengths. It would be expected that at these locations the flow could be represented as a base flow with a superimposed perturbation.

$$\bar{v} = \bar{v}_0(t, r, z) + \bar{v}'(t, r, \theta, z) \quad v'/V_0 \ll 1$$

$$p = p_0(t, r, z) + p'(t, r, \theta, z) \quad p'/p_0 \ll 1$$

where the base flow is independent of the azimuthal coordinate.

For this case, the equations describing the base flow are

$$\frac{D\bar{V}_0}{Dt} = - \frac{\nabla p_0}{\rho_0} \quad \text{and} \quad \frac{D\rho_0}{Dt} + (\rho_0 \bar{V}_0) = 0$$

Using as a coordinate system the modified cylindrical coordinate system shown below, the equation of motion may be written in terms of the tangential velocity and the meridional velocity,

$$\bar{V}_m = V_r \hat{i}_r + V_z \hat{i}_z$$


The equations of motion written in a general orthogonal curvilinear coordinate system are

$$\frac{\partial \rho}{\partial t} + \frac{1}{h_n h_m h_\theta} \left[\frac{\partial}{\partial n} (h_m h_\theta \rho u_n) + \frac{\partial}{\partial m} (h_n h_\theta \rho u_m) + \frac{\partial}{\partial \theta} (h_n h_m \rho u_\theta) \right] = 0$$

$$\frac{\partial u_n}{\partial t} + \frac{u_n}{h_n} \frac{\partial u_n}{\partial n} + \frac{u_m}{h_m} \frac{\partial u_n}{\partial m} + \frac{u_\theta}{h_\theta} \frac{\partial u_n}{\partial \theta} + \frac{u_n u_m}{h_n h_m} \frac{\partial h_n}{\partial m} + \frac{u_n u_\theta}{h_n h_\theta} \frac{\partial h_n}{\partial \theta} \quad (3.11)$$

$$- \frac{u_m^2}{h_n h_m} \frac{\partial h_m}{\partial n} - \frac{u_\theta^2}{h_n h_\theta} \frac{\partial h_\theta}{\partial n} = - \frac{1}{\rho h_n} \frac{\partial p}{\partial n}$$

$$\frac{\partial u_\theta}{\partial t} + \frac{u_n}{h_n} \frac{\partial u_\theta}{\partial n} + \frac{u_m}{h_m} \frac{\partial u_\theta}{\partial m} + \frac{u_\theta}{h_\theta} \frac{\partial u_\theta}{\partial \theta} + \frac{u_\theta u_m}{h_\theta h_m} \frac{\partial h_\theta}{\partial m} + \frac{u_\theta u_n}{h_\theta h_n} \frac{\partial h_\theta}{\partial n}$$

$$- \frac{u_m^2}{h_m h_\theta} \frac{\partial h_m}{\partial \theta} - \frac{u_n^2}{h_n h_\theta} \frac{\partial h_n}{\partial \theta} = - \frac{1}{\rho h_\theta} \frac{\partial p}{\partial \theta}$$

$$\frac{\partial u_m}{\partial t} + \frac{u_n}{h_n} \frac{\partial u_m}{\partial n} + \frac{u_m}{h_m} \frac{\partial u_m}{\partial m} + \frac{u_\theta}{h_\theta} \frac{\partial u_m}{\partial \theta} + \frac{u_m u_n}{h_m h_n} \frac{\partial h_m}{\partial n} + \frac{u_m u_\theta}{h_m h_\theta} \frac{\partial h_m}{\partial \theta}$$

$$-\frac{u_{\theta}^2}{h_m h_{\theta}} \frac{\partial h_{\theta}}{\partial m} - \frac{u_n^2}{h_n h_{\theta}} \frac{\partial h_n}{\partial m} = -\frac{1}{\rho h_m} \frac{\partial p}{\partial m}$$

Since $u_n = 0$, by definition and $\frac{\partial}{\partial \theta} = 0$ by assumption, these equations reduce for the base flow to,

$$\begin{aligned} \frac{\partial u_m}{\partial t} + \frac{u_m}{h_m} \frac{\partial h_m}{\partial m} - \frac{u_{\theta}^2}{h_m h_{\theta}} \frac{\partial h_{\theta}}{\partial m} &= -\frac{1}{\rho h_m} \frac{\partial p}{\partial m} \\ \frac{\partial p}{\partial t} + \frac{1}{h_m} \frac{\partial(\rho u_m)}{\partial m} + \rho u_m \left[\frac{1}{h_n h_m h_{\theta}} \frac{\partial(h_n h_{\theta})}{\partial m} \right] &= 0 \\ \frac{\partial u_{\theta}}{\partial t} + \frac{u_m}{h_m} \frac{\partial u_{\theta}}{\partial m} + \frac{u_{\theta} u_m}{h_m h_{\theta}} \frac{\partial h_{\theta}}{\partial m} &= 0 \\ -\frac{u_m^2}{h_m h_n} \frac{\partial h_m}{\partial n} - \frac{u_{\theta}^2}{h_n h_{\theta}} \frac{\partial h_{\theta}}{\partial n} &= -\frac{1}{\rho h_n} \frac{\partial p}{\partial n} \end{aligned} \quad (3.12)$$

The first two equations may be rewritten in characteristic form using the isentropic relation $dp = a^2 d\rho$

$$\begin{aligned} \frac{\partial u_m}{\partial t} + \frac{u_m}{h_m} \frac{\partial u_m}{\partial m} + \frac{1}{\rho h_m} \frac{\partial p}{\partial m} &= \frac{u_{\theta}^2}{h_m h_{\theta}} \left(\frac{\partial h_{\theta}}{\partial m} \right) \\ \frac{1}{\rho a} \frac{\partial p}{\partial t} + \frac{u_m}{\rho a h_m} \frac{\partial p}{\partial m} + \frac{a}{h_m} \frac{\partial u_m}{\partial m} &= -\frac{a u_m}{h_n h_m h_{\theta}} \frac{\partial(h_{\theta} h_n)}{\partial m} \end{aligned} \quad (3.13)$$

Adding and subtracting these equations yields

$$\begin{aligned} \left[\frac{\partial u_m}{\partial t} \pm \frac{1}{\rho a} \frac{\partial p}{\partial t} \right] + \frac{1}{h_m} \left[(u_m \pm a) \frac{\partial u_m}{\partial m} + (u_m \pm a) \frac{1}{\rho a} \frac{\partial p}{\partial m} \right] &= \frac{u_{\theta}^2}{h_m h_{\theta}} \frac{\partial h_{\theta}}{\partial m} \\ &+ \frac{a u_m}{h_n h_m h_{\theta}} \frac{\partial(h_{\theta} h_n)}{\partial m} \end{aligned}$$

or

$$\frac{D^+ J^+}{Dt} = \frac{u_\theta^2}{h_m h_\theta} \frac{\partial h_\theta}{\partial m} - \frac{a u_m}{h_m h_\theta h_n} \frac{\partial (h_\theta h_n)}{\partial m}$$

where

$$J^+ = u_m + \frac{2}{\gamma-1} a \quad (3.14)$$

$$\frac{D^- J^-}{Dt} = \frac{u_\theta^2}{h_m h_\theta} \frac{\partial h_\theta}{\partial m} + \frac{a u_m}{h_m h_\theta h_n} \frac{\partial (h_\theta h_n)}{\partial m}$$

where

$$J^- = u_m - \frac{2}{\gamma-1} a$$

The third equation is already in characteristic form.

$$\frac{Du_\theta}{Dt} = - \frac{u_\theta u_m}{h_\theta h_m} \frac{\partial h_\theta}{\partial m} \quad (3.15)$$

These characteristic equations are identical in form to the one dimensional unsteady flow equations.

For transonic compressor rotors the meridional Mach number is less than one at the upstream and downstream boundaries. In this case information flows to a point along the downstream running J^+ and convective characteristics and along the upstream running J^- characteristic. If a point lies on the upstream computational boundary, the J^+ characteristic value may be specified as well as the swirl velocity, u_θ . If a point lies on the downstream computational boundary, the J^- characteristic value may be specified.

For the highly loaded calculation, an inlet reservoir condition, corresponding to a J^+ value, and an inlet swirl velocity of zero were specified. At the exit boundary, the static pressure was

-49-

specified. The curvature term, $\frac{1}{h_m h_\theta} \frac{\partial h_\theta}{\partial m}$ was assumed to be small as would be the case if the physical domain were imagined to be extended several diameters with constant radii both upstream and downstream. This choice was made to model the experimental situation and for convenience, but more general geometries could be utilized.

These boundary conditions are equivalent to the physical constraints imposed when a compressor is tested. Inlet or reservoir conditions are specified, usually atmospheric stagnation conditions, and the inlet swirl velocity is zero. Downstream of the compressor, some throttling device is used to determine the compressor operating point. A particular operating point is determined by the intersection of the compressor characteristic and the throttle characteristic. The operation of this device could be simulated by specifying either the compressor static pressure ratio or the mass flow. It is computationally somewhat easier to specify the rotor static pressure ratio.

No attempt was made to calculate the actual flow at the throttle, and hence account for the effect of disturbances there. Such a calculation, especially in the strongly rotating flow downstream of the rotor, is potentially as difficult as the through-flow calculation itself. This simplification does imply some inconsistencies at the boundaries. In particular, at the upstream boundary the transmission of acoustic disturbances is falsified; at the downstream boundary vorticity convection is distorted. The acoustic

disturbances carry very little energy and their falsification can have very little influence on the flow over the rotor. The rotor mass flow for the solution to be presented was determined not by the accumulated action of acoustic waves but by the action of a few nearly plane waves of finite amplitude. When the downstream perturbations are not calculated, the effective model of the flow beyond the downstream computational boundary is one which is axisymmetric and uniform in the streamwise direction. Such a flow can have no radial vorticity and is potentially inconsistent with the blade flow solution if that solution requires a significant amount of radial vorticity to be present at the computational boundary. For the present solution, this inconsistency does not appear to be important even though some radial vorticity is shed by the rotor. This vorticity is considerably modified by the cumulative action of the artificial viscosity terms and the inherent dissipation and dispersion of the numerical scheme. Resolution of radial vorticity is further degraded by the increased spacing between axial grid points as the downstream boundary is approached. In future calculations, the importance of the artificial viscosity terms should be reduced by an order of magnitude or more. When this occurs, the present model should be reconsidered.

An auxiliary observation to be made at this point about equations (3.12) is that the addition of blade force terms would not alter their hyperbolic nature. Such a set of equations offers a different method of solution for axisymmetric through-flow problems.

Some distinct advantages may stem from its hyperbolic nature when the meridional Mach number approaches or exceeds one.

Limitations of computation time and storage prevent detailed flow resolution near blunt leading and trailing edges. These points are dealt with by the expedient of placing them between grid points, or considering the edges to be infinitely thin. The Kutta condition is imposed at the trailing edge by requiring that the suction and pressure surface flow angles, in a plane normal to the blade axis, and pressure be equal at the last grid point on the blade. This procedure allows a slip surface to form in a plane tangent to the trailing edge. The movement of this surface is not explicitly followed in the calculation.

3.4 Results of Numerical Calculation

The solution for the highly loaded case was computed using the IBM 370/168 computer available at the Information Processing Center at Massachusetts Institute of Technology and the IBM 360/67 Time Sharing System at the NASA Lewis Research Center at Cleveland, Ohio. The number of grid points necessary for a three dimensional problem, about 13,000 for this solution, means that a large amount of computer time is required to achieve a converged solution. Because of the large expenditure of CPU time involved, this calculation was terminated when the solution was further from steady state than would normally be desired. A residual unsteadiness of 5 percent is present at some points in the domain, but major features of the solution like rotor total pressure ratio and shock wave

strengths have been stable for over 80 time steps.

The computed rotor total pressure ratio, mass averaged, is 1.82 compared to 1.68 for the isentropic design case. The computed average inlet Mach number is 0.46 while the design case has an inlet Mach number of 0.50. The radial variation in the θ averaged total and static pressure ratios at the rotor exit is illustrated in Figure 3.5. This figure shows that the computed total pressure ratio varies from a minimum value of 1.52 at the hub radius to approximately 1.85 at midspan. From this point out to the tip, the pressure ratio oscillates around a value of about 1.88. The design pressure ratio is constant at a value of 1.68. A minimum static pressure ratio of 1.07 occurs at the hub radius and the pressure ratio rises to a maximum value of 1.40 near the tip radius.

Figure 3.6 shows the variation with radius of the inlet air angle, in the relative reference frame, and the incidence angle. Over the outer portion of the blade span, the incidence angle is nearly equal to the design values. Over the inner portion of the blade span, the incidence angles are much higher than the design values; the additional incidence reaching 12.5 degrees at the hub radius. In later sections the effect of these large angles of attack on the rotor through-flow will be clearly seen.

The rotor exit air angles and the deviation angles are shown in Figure 3.7 for the design and the computational cases. The design exit angles are taken from the correlations of reference (8) for double and multiple circular arc blades. The agreement between

the predicted angles and angles from the correlations is quite good over the entire span. The maximum difference is about two degrees. The maximum deviation from the blade metal angles can also be seen to be only two or three degrees across most of the blade span. At the hub radius the blade camber is quite large, as is normally the case with free vortex blading, and the deviation increases accordingly.

Figure 3.8 compares the computed axial and pitchwise Mach number variation with radius at the rotor exit to the design values. The computed axial Mach number is close to the design value of 0.46 over the whole span. This figure also shows that the computed pitchwise Mach number is higher than the design values over the entire span. The design intent was to produce a free vortex outflow, and the computed outflow approximates a free vortex from $r/r_t = 0.75$ to the tip radius. Near the hub radius the computed pitchwise Mach number is constant rather than decreasing like $1/r$.

Contour plots of the relative coordinate system Mach number are shown in Figures 3.9 through 3.12. These plots are for computational blade-to-blade surfaces at the blade tip radius, the hub radius and at two intermediate radii. Figure 3.9 indicates that a strong passage shock exists at the tip radius and that it is nearly normal to the flow. A weak oblique shock stands in front of the cascade. The particular numerical method used is of the shock capturing type which means that shock waves are resolved as local areas of high gradients spread over several mesh points. The approximate

location of the computed shocks is shown as dashed lines in the figures. For the passage shock, this dashed line follows the Mach number equal 1.0 contour which is at about the midpoint of this shock. The importance of the entrance region geometry is indicated by the expansion of the flow up to a Mach number of 1.7 on the suction surface. Resolution of the oblique shock is poor because of the relative coarseness of the finite difference grid in the upstream region. The overall flow appears qualitatively the same as the two dimensional flow illustrated by Figure 3.1. In Figures 3.10 and 3.11, the passage shock can be seen to weaken and move forward relative to the blades as the radius decreases. The bow shock in front of the cascade weakens and then disappears. Figure 3.12 shows the Mach number contours along the hub surface. In this figure the effect of the large angle of attack on this blade section can be seen. A patch of supersonic flow appears on the suction surface in an otherwise subsonic flow as a result of the large flow turning around the blade leading edge. A sharp recompression terminates the supersonic patch and extends across the blade passage.

Plots of the pressure coefficient, $C_p = (p - p_i) / \frac{1}{2} \rho_i u_i^2$, along these same computational blade to blade surfaces are shown in Figures 3.13 through 3.16. The subscript "i" here refers to rotor passage inlet conditions. These figures illustrate that the blade loading is very high especially at the hub radius, Figure 3.16. Here the ΔC_p from the minimum pressure point to the rotor exit is 1.42. This pressure rise is near the maximum that a two dimensional

turbulent boundary layer can be expected to traverse, $(p_{\text{exit}} - p_{\text{min}})$
 $/ \frac{1}{2} (\rho u^2)_{\text{at } p_{\text{min}}}$ is 0.81. The blade loading decreases
 as the radius increases, ΔC_p is only 0.59 at the tip radius.
 However, the passage shock is probably strong enough to separate
 the suction surface boundary layer. The absence of a leading edge
 stagnation point is due to the relative coarseness of the finite-dif-
 ference grid at the leading and trailing edges.

The flow field as illustrated by these eight figures appears
 qualitatively as might be expected if the flow were quasi-two dimen-
 sional. One illustration, however, that this flow is in fact
 strongly three dimensional is shown in Figure 3.17. This figure
 shows the position of three computed blade-to-blade stream surfaces,
 which are normally called S1 surfaces. The coordinates of these
 surfaces were determined by integration along the fluid particle
 paths, through a constant inlet radius line. The projected view of
 these surfaces is the one which would be seen by an observer facing
 directly downstream. Near the tip radius these surfaces approximate
 a surface of revolution; however, at smaller radii they cannot be
 approximated as surfaces of revolution. The middle stream surface
 in Figure 3.17 has an inlet radius ratio of 0.772. At the rotor
 exit, the streamline on the blade suction surface has a radius ratio
 of 0.80; while the streamline on the blade pressure surface has an
 exit radius ratio of 0.85. The radial displacement of the two
 streamlines is 16 percent of the blade height. At a slightly lower
 radius, the displacement in streamlines is at its maximum value of

20 percent. The warpage or streamline radial displacement is one manifestation of the streamwise vorticity being shed by the rotor blade. The necessity for a shed vortex sheet near the hub radius is shown by Figure 3.8, where it can be seen that the average outlet pitchwise velocity approximates a free vortex only over the outer portion of the blade span. The very intricate nature of the flow kinematics is illustrated by the S1 surface nearest the hub. Along the blade suction surface the flow is converging in the radial direction while the streamlines are diverging in the azimuthal direction. The reverse situation is occurring on the pressure surface.

Stream surfaces with a different orientation, normally called S2 surfaces, are shown in Figure 3.18. These surfaces are determined by fluid particles which initially lie on a radial line. The S2 surfaces shown have upstream positions near the blade pressure surface, at mid-gap, and near the blade suction surfaces. The angular distance between these surfaces has been exaggerated to allow each surface to be seen but otherwise they are to the same scale and viewed as Figure 3.17. This figure shows, perhaps more clearly than Figure 3.17, the blade to blade and hub to tip variation in streamline shape imposed by the free vortex blading.

The flow field illustrated in this chapter seems to be a reasonable and realistic inviscid flow solution for a highly loaded transonic compressor rotor. While this solution could be improved by continued iteration to reduce unsteadiness and by increased grid resolution at blade leading edges, incorporating even a first order

boundary layer growth and separation prediction would seem to be a more important step. In the next chapter, this solution will be compared to experimental measurements made at the rotor design point.

COMPARISON OF RESULTS AND DISCUSSION

4.1 Comparison of Inviscid Solution to Intra-Blade
Density Measurements

An unique visualization study of the flow through the test rotor has been reported by Epstein (3). He was able to visualize the instantaneous static density field using a fluorescent gas, 2, 3 butanedione, as a tracer. In this technique, the flow is illuminated along a plane using a dye laser. The laser produces a 0.3 micro-second pulse centered at a wavelength of 425 nm. Illumination at this wavelength causes the tracer gas to fluoresce, within 10^{-8} seconds. The intensity of the fluorescent emission, when photographically recorded, indicates the density variation in the illuminated plane. Quantitative density maps are obtained by correcting the images for distortion and non-linearities in the illumination and imaging systems. All the visualized density maps shown in this chapter are reproduced from reference (3).

Figure 4.1 shows the radial positions of the seven planes for which density maps were obtained. The visualized density in the outermost plane, radius ratio of 0.88, is shown in Figure 4.2. In this and subsequent fully corrected contour maps, the contour interval is approximately 10 percent and the upstream density is specified to be 1.0. The computed density contour map on this same plane is shown in Figure 4.3. The contour interval for this map is 5 percent. This figure shows that the flow expansion on the blade suction

surface is accurately predicted both in magnitude and shape. The flow expands to a density of about 90 percent of the upstream density at a point midway between the leading edge and the passage shock. The spatial resolution of the passage shock is of course much finer in the optical density measurements, but the shock strength is the same in both cases, density ratio of 1.35, and the shock falls nearly at the blade maximum thickness point. The flow visualization also shows the passage shock to terminate in a lambda shock formation typical of a laminar shock-boundary layer interaction. It appears that the shock does separate the boundary layer as would be expected for a shock of this strength. A density ratio of about 1.1 is predicted for the oblique shock standing in front of the rotor while the measured value is 1.2. The flow visualization also shows the shock to be detached. The computed shock strength is correct for an attached oblique shock. For example, at a radius ratio of 0.88, the upstream Mach number is 1.3 and the required turning to align the flow with the suction surface is 3.5 degrees. According to the Rankine-Hugoniot relations, this shock should be attached and have a density ratio of 1.1. The computed density ratio is 1.1. However, a small decrease in the upstream Mach number would require that the shock be detached as it is in the visualization photographs.

The visualized and computed densities at a radius ratio of 0.83 are shown in Figures 4.4 and 4.5. The visualized flow appears much the same as at the previous radius except for the low density

"bubble" at the foot of the passage shock. A possible explanation for this "bubble" is that it is the core of a strong vortex formed by the vorticity from the outer region of the blade turning downstream around the separation region. Away from this "bubble" the computed flow seems to accurately model the visualized flow.

Experimental and computed densities in the $r/r_t = 0.80$ plane are shown in Figures 4.6 and 4.7. This plane is at a slightly larger radius than the design sonic cylinder. The passage shock remains quite strong in both cases, density ratio of 1.3, and the flow expands on the suction surface to a density nearly equal to the upstream density. The measured strength of the oblique shock is large, density ratio of 1.25; while, the computed shock strength is again smaller, about 1.05. No evidence of boundary layer separation is found at this radius, and the match between the computed and experimental densities is best at this radius. The important three dimensional nature of this flow is illustrated by the fact that the suction surface expansion does not continue from the blade leading edge up to the passage shock as it would if the flow were two dimensional. The predicted minimum density point generally occurs about midway between the leading edge and the passage shock. The experimental minimum density also occurs in this same area although this fact is not clear from Figure 4.6.

At a radius ratio of 0.70, Figures 4.8 and 4.9, the character of the flow has markedly changed. In the visualized flow the bow shock has been replaced by a diffuse compression region. Computed

Mach number contours in the entrance region are closely approximated by Mach number contours along the computational blade to blade surface shown in Figure 3.11. The computed flow expands to a density ratio of 0.80, relative to the upstream flow, at about the 35 percent chord point as does the visualized flow. In both cases, the density rise across the blade passage is 1.3.

The density fields are compared at a radius ratio of 0.65 in Figures 4.10 and 4.11. This radius is the smallest for which experimental measurements are available; unfortunately, much of the blade passage is obscured by the blade shadow. Computed Mach numbers are subsonic on this plane except for a supersonic patch at the minimum density point. This point occurs somewhat further downstream of its experimental position but otherwise the two density maps compare well.

These comparisons between the visualized and computed densities demonstrate that the inviscid computation accurately predicts the intra-blade density field upstream from obvious viscous phenomena like the passage shock-boundary layer interaction. The only important difference is the consistent under prediction of the oblique shock strength.

To determine if this difference is due to insufficient grid resolution, the difference in rotor total pressure ratio, or some other explanation such as an unstarted rotor passage will require further work.

4.2 Comparison of Inviscid Solution to Exit Flow

Measurements

The average performance of the test rotor was predicted well within the limitations of inviscid flow analysis. Radial profiles of the computed and experimental total and static pressure ratio, theta averaged, are shown in Figure 4.12. This figure shows that the average profile is accurately predicted even though the computed total pressure ratio is higher than the experimental value. The computed total pressure ratio, mass averaged, is 1.85; the experimental value is 1.64. Contour maps of the total and static pressures in a r - θ plane immediately downstream of the rotor are shown in Figures 4.13 and 4.14. Small deviations from periodicity with blade spacing in these maps are artifacts from the contour plotting routine. Except for the spikes in total pressure at $r/r_t = 0.86$ and 0.91 , important blade to blade variations occur only around $r/r_t = 0.80$. Figures 2.24 and 2.25 are the experimental pressure maps for the same axial station. The basic radial gradients in both of these maps are predicted accurately, but local details particularly near the blade wakes are not predicted well. One unusual feature of the flow, the spikes in total pressure, does appear to have an inviscid origin since they appear in both experimental and computed pressure maps.

The computed average flow angles in the relative reference frame are compared to the experimental angles in Figure 4.15. For $r/r_t < 0.90$ the predicted angles are generally one to two degrees

-63-

lower than the measured values. At larger r/r_t the predicted values are generally 6 to 7 degrees lower than the measured values. Both the time resolved pressure measurements and the gas density measurements indicate that an unsteady boundary layer separation is occurring at these radii.

Figure 4.16 shows the pitchwise variation of the computed velocity components at a radius ratio of 0.75. Figures 2.14 and 2.15 show the time resolved Mach number components at a comparable location. In Figure 2.14, areas of low axial Mach number are the viscous blade wakes. These wakes also have an excess of pitchwise Mach number. Between these wakes the structure of the velocity field is reasonably well predicted by the inviscid computation. In particular, the computed radial velocity has a large outward component at the pressure surface. The measured radial velocity, Figure 2.15, also has a large outward component at the edge of the pressure side of the wake. Across the wake, its radial Mach number decreases by 0.20 to 0.25 which means that a large cross flow velocity exists inside the wake. Pitchwise and axial Mach numbers between the wakes are generally consistent with Figure 4.16. The time resolved flow from the hub to a radius ratio of about 0.80 is similar to the flow shown in Figures 2.14 and 2.15.

Predicted velocities at a radius ratio of 0.86 are shown in Figure 4.17. These velocities are similar to those for $r/r_t = 0.75$ except for a smaller jump in radial velocity. Figures 4.18 and 4.19 show the time resolved Mach number components at a radius ratio

of 0.845. Wakes at this radius are not as sharply defined as at lower radii, and the first wake shown appears to be shed from a badly stalled blade. Away from the stalled blade, the inviscid core flow is generally consistent with the predicted velocities although the agreement is poorer than at an r/r_t of 0.74. Increasing flow unsteadiness appears as the radius ratio increases to 0.87, Figures 2.18 and 2.19. Blades at this radius appear either to be badly stalled or to shed no easily defined wake. The inviscid computation does not seem to model any portion of the flow accurately. As the radius increases further, the time resolved flow remains unsteady, and the agreement with the predicted velocities remains generally poor.

Average computed and experimental exit Mach number profiles are compared in Figure 4.20. The computed pitchwise Mach number profile has nearly the same shape and slope as the experimental profile except at the tip radius, but is at a higher level which reflects the higher computed pressure ratio. At a radius ratio of 0.95, the experimental profile rises steeply. The axial Mach number profiles differ substantially over the whole span. Much of the difference in axial Mach number at the hub is due simply to the effect of wake blockage. A simple integration over the measured wake profile yields a total wake displacement thickness which is approximately 15 percent of the blade spacing. Accounting for this amount of blockage in a one dimensional manner would bring the computed axial Mach number near the hub from 0.42 up to 0.55; the

measured value at this location is 0.62. If the relative coordinate system turning remained the same, this change in axial Mach number would bring the computed pitchwise Mach number down to 0.47 from 0.53; the measured value at this location is 0.43. Even though these changes represent only a lowest order correction to the computed solution, it seems clear that accounting for the blade boundary layer growth in even a simple manner would greatly improve the accuracy of the predicted average performance.

The experimentally observed decrease in axial velocity and increase in pitchwise velocity at the tip radius are results which have often been reported for single and multiple stage compressors (16, 17, 18). These profiles are generally agreed to result from the existence of an annulus wall boundary layer. However, for the test rotor this explanation requires that the tip boundary layer grow to a thickness which is approximately 10 percent of the blade span across the rotor. Such a growth rate is several times faster than that predicted by the best calculation procedures (18, 19). These methods do not consider that for the test rotor the tip boundary layer must cross both branches of the bow shock which could cause rapid boundary layer growth. The experimental flow is further complicated by the fact that in the outer portion of the annulus blade wakes have a large pitchwise velocity and a large outward radial velocity. These wakes which also have low axial velocity tend to accumulate at the tip radius. The importance of these wakes and the wall boundary layer is illustrated by the experimental total

temperature map immediately downstream of the rotor, Figure 2.30. An area of high temperature, low axial velocity fluid has collected near the tip on the pressure side of the wake. This fluid is probably accumulated both by cross-flow in the wall boundary layer and by convection of the blade wakes. At the measurement plane one chord downstream, this fluid on the pressure side of the wake seems to have become the center of a major loss area, see Figure 2.33 which is an entropy rise map.

While the inviscid calculation provides a realistic base flow solution and some insight into the details of the flow downstream of the rotor, this exit flow is dominated to a large extent by the wakes and the wall boundary layers. A significant improvement in the computed average performance can be achieved by incorporating even simple boundary layer models, but a complete understanding of the downstream flow will require detailed consideration of the wakes and the wall boundary layer.

CONCLUSIONS AND DISCUSSION

A comprehensive investigation of the flow field produced by an isolated transonic compressor rotor has been completed. This study included time resolved flow measurements at two axial locations downstream of the rotor and a numerical computation of the three dimensional inviscid through-flow. Spatial and temporal resolution achieved was sufficient to determine velocity components and pressures inside individual blade wakes and in the surrounding flow. These measurements showed that the exit flow could be separated into an inviscid core flow plus a wake only in the inner half of the annulus. In the outer half of the annulus, the exit flow was unsteady in the relative reference frame because of an interaction with a cellular flow pattern established in the downstream annulus by the shear disturbances themselves. Where an inviscid core flow existed, its details were consistent with the through-flow solution, but significant interaction between the core flow and the wakes occurs. Where boundary layer separation and unsteadiness were important flow features, the inviscid through-flow solution did not accurately predict flow details, but the rotor average performance was predicted well within the limitations of an inviscid analysis. The accuracy of the predicted average performance could be greatly improved by accounting for wake blockage. Comparisons between the computed through-flow and a set of intra-blade density measurements showed that the computed solutions

accurately predicted the density field inside the rotor blade passage even though the viscous phenomenon have an important influence on the exit flow.

The three dimensional inviscid computation has considerable potential as a compressor design and development tool, especially when coupled with an accurate boundary layer solution, even though each solution requires a large amount of computer time. It is estimated that a converged solution for a new rotor geometry will require about 25 hours of CPU time on an IBM 370/168. Such an expenditure, while inappropriate for preliminary design studies, can be easily justified for evaluation and improvement of final designs. In addition when computations of this type are coupled with high resolution experimental measurements these computations are a powerful tool for understanding the flows encountered in existing compressors.

REFERENCES

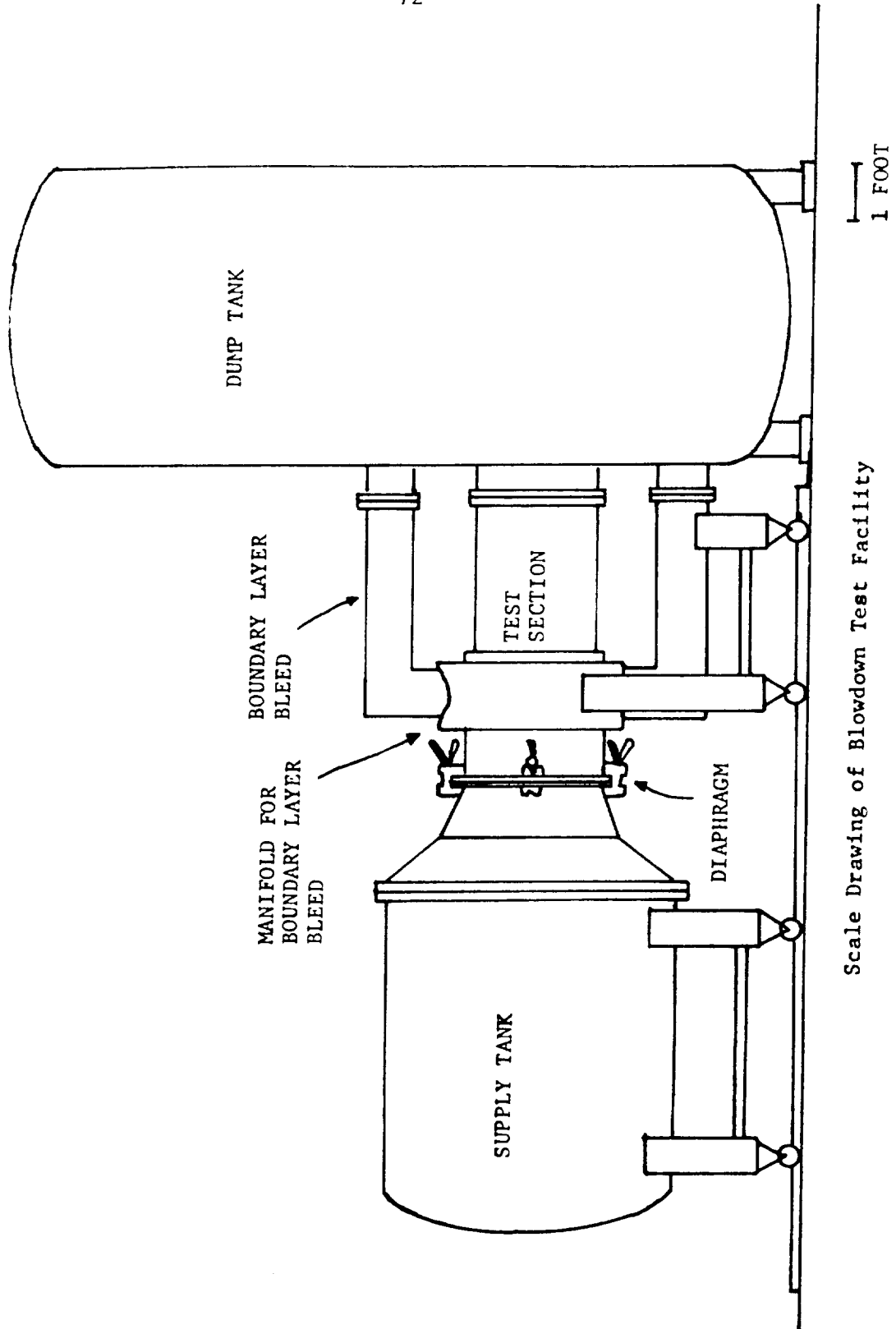
1. Lakshminarayana, B., and Poncet, A., "A Method of Measuring Three-Dimensional Wakes in Turbomachinery," J. Fluids Engr., June 1974.
2. Weyer, J., and Hungenberg, H., "Analysis of the Unsteady Flow in a Transonic Compressor by Means of High-Response Pressure Measuring Techniques," AGARD Conference on Unsteady Phenomena in Turbomachinery, AGARD CPP-177, Paper No. 11, 1975.
3. Epstein, A. H., "Quantitative Density Visualization in a Transonic Compressor Rotor," Ph.D. Thesis, MIT, Sept. 1975.
4. Kerrebrock, J. L., "The MIT Blowdown Compressor Facility," MIT Gas Turbine Lab. Report No. 108, Sept. 1975.
5. Gallus, H. E., "Results of Measurements of the Unsteady Flow in Axial Subsonic and Supersonic Compressor Stages," AGARD Conference on Unsteady Phenomena in Turbomachinery, AGARD CPP-177, Paper No. 10, 1975.
6. Probst, H. C., "Gas Turbine Laboratory Data Transmission/Reduction System," MIT Gas Turbine Lab. Internal Memorandum, Sept. 1971.
7. Kerrebrock, J. L., and Mikolajczak, A. A., "Intra-Stator Transport of Rotor Wakes and Its Effect on Compressor Performance," ASME Paper No. 70-GT-39.
8. Johnson, I., and Bullock, R., eds., "Aerodynamic Design of Axial Flow Compressors," NASA SP-36 NASA 1965.
9. Kerrebrock, J. L., "Waves and Wakes in Turbomachine Annuli

with Swirl," AIAA Paper No. 74-87.

10. Thompkins, W. T., and Kerrebrock J. L., "Exit Flow from a Transonic Compressor Rotor," AGARD Conference on Unsteady Phenomena in Turbomachinery, CPP-177, Paper No. 6, 1975.
11. Thompkins, W. T., "Combination Tones from a Transonic Compressor Rotor," SM Thesis, MIT, Sept. 1973.
12. Oliver, D. A., and Sparis, P., "A Computation Study of Three-Dimensional Transonic Shear Flow in Turbomachine Cascades," AIAA Paper No. 71-83.
13. Sparis, P., "A Computational Study of the Three-Dimensional Flow in a Single Stage Transonic Compressor," Ph.D. Thesis, MIT, February 1974.
14. McCormack, R. W., and Warminy, R. F., "Survey of Computational Methods for Three-Dimensional Supersonic Inviscid Flow with Shocks," AGARD LSR-64, Paper No. 5, 1973.
15. Abbett, M. "Boundary Condition Computational Procedures for Inviscid Supersonic Steady Flow Field Calculations," Aerotherm Corp., Mt. View, Calif., Final Report 71-41, 1971.
16. Hirsch, C., "End-Wall Boundary Layers in Axial Compressors," ASME Paper No. 74-GT-72.
17. Smith, L. H., Jr., "Casing Boundary Layers in Multistage Compressors," Proceedings, Symposium on Flow Research on Blading, Brown Boveri, Ltd., Baden, Switzerland, 1969.
18. Balsa, T. F., and Mellor, G. L., "The Simulation of Axial Compressor Performance Using an Annulus Wall Boundary Layer

Theory," ASME Paper No. 74-GT-56.

19. Daneshyar, M., and Horlock, J. H., and Marsh, H., "Prediction of Annulus Wall Boundary Layers in Axial Flow Turbomachines," University of Cambridge Report CUED/A - Turbo/TR 31, 1972.



Scale Drawing of Blowdown Test Facility

Figure 2.1

Typical Blowdown Facility Parameters
for a Design Speed Test

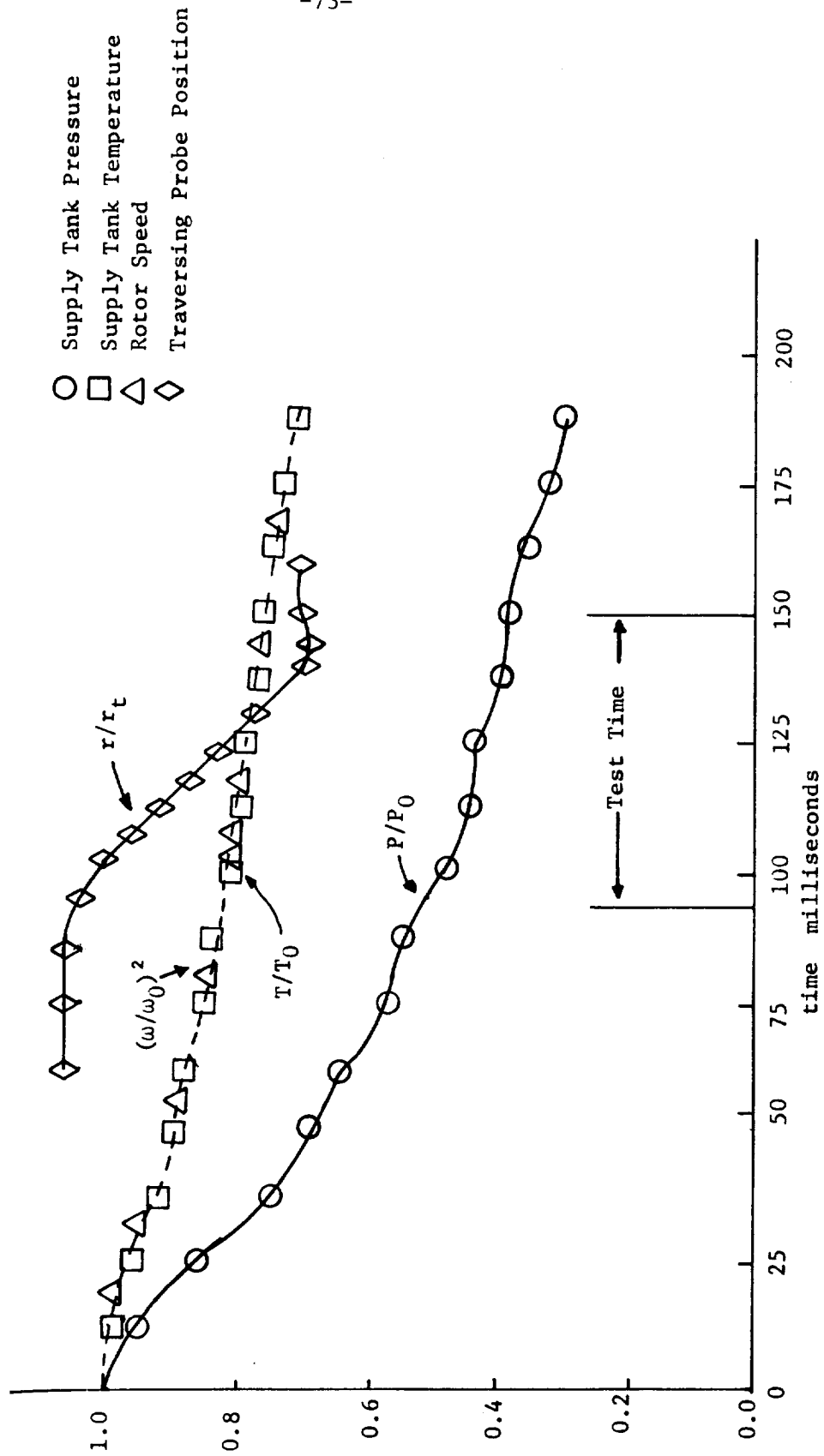
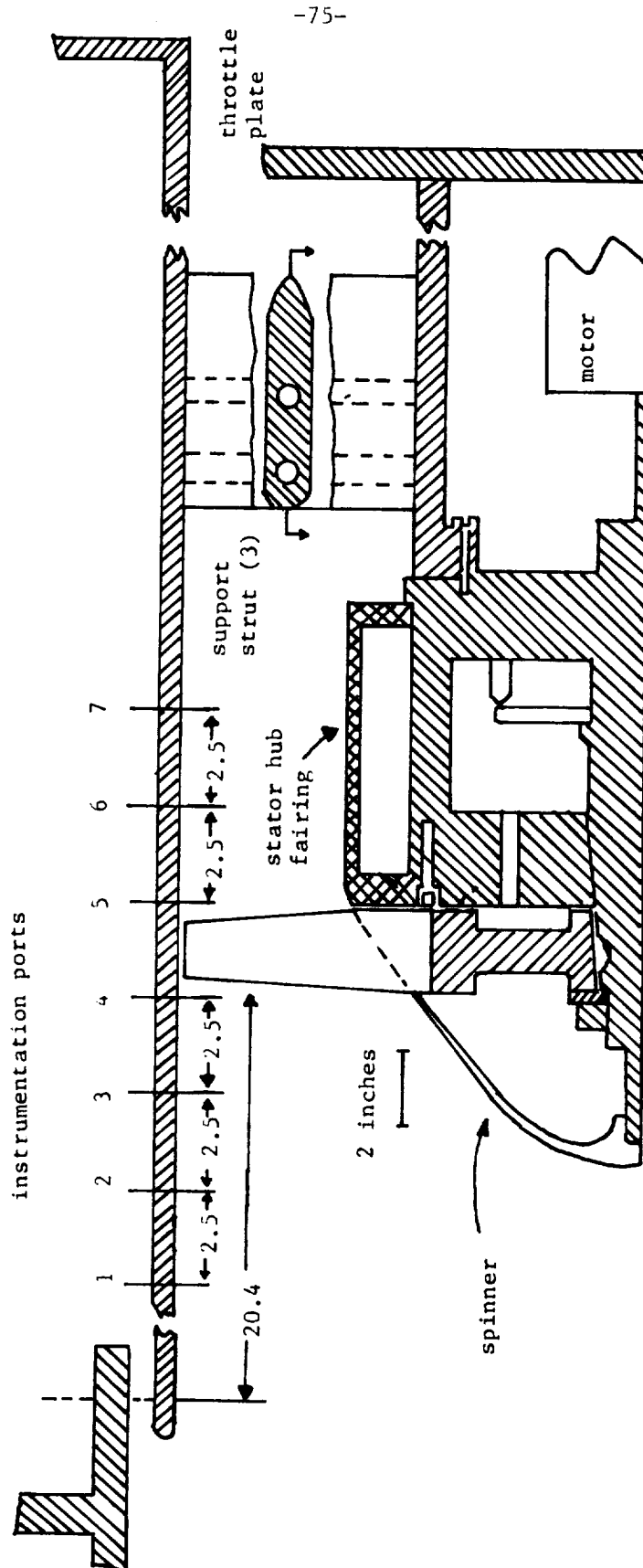


Figure 2.2

Design Parameters for Each Design Streamsurface

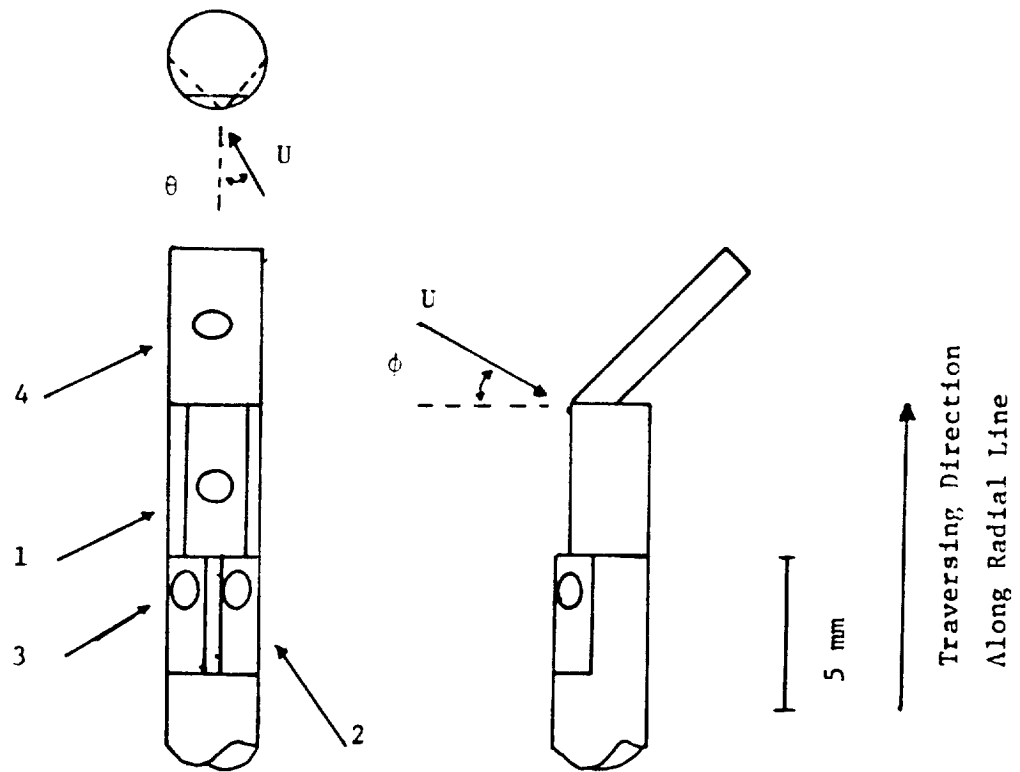
r_1/r_t	0.5	0.6	0.7	0.8	0.9	1.0
r_2/r_t	0.64	0.71	0.78	0.85	0.93	1.0
M_t	0.60	0.72	0.84	0.96	1.08	1.2
M_{r1}	0.78	0.88	0.98	1.07	1.29	1.30
β_1	50.2	55.2	59.2	62.5	65.2	67.4
β_2	23.8	35.7	44.2	50.6	55.6	59.5
σ_r	2.00	1.67	1.43	1.25	1.11	1.00
D_r	0.50	0.49	0.45	0.43	0.40	0.38
i_c	11.5	10.4	9.9	7.7	4.5	1.3
ϕ	22.0	14.7	9.0	7.5	6.7	8.1
α_1	38.7	44.8	49.3	55.0	61.2	66.1
α_2	16.7	30.1	40.3	47.5	54.1	58.0
δ	28.9	38.1	45.0	51.1	56.3	61.7
t/c	0.10	0.086	0.072	0.058	0.044	0.030
M_3	0.68	0.65	0.62	0.60	0.58	0.57

Figure 2.3



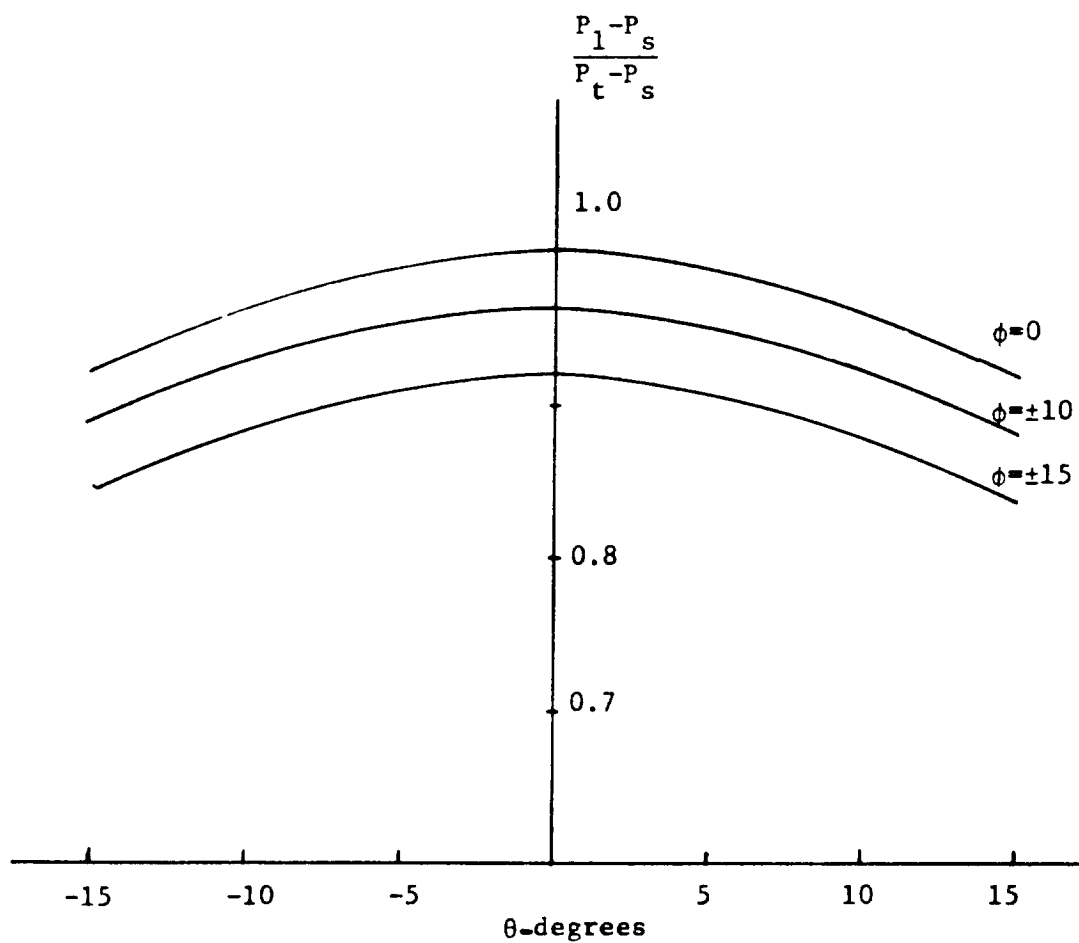
Scale Drawing of Test Section Showing Location of
Instrumentation Ports and Rotor Flowpath

Figure 2.4



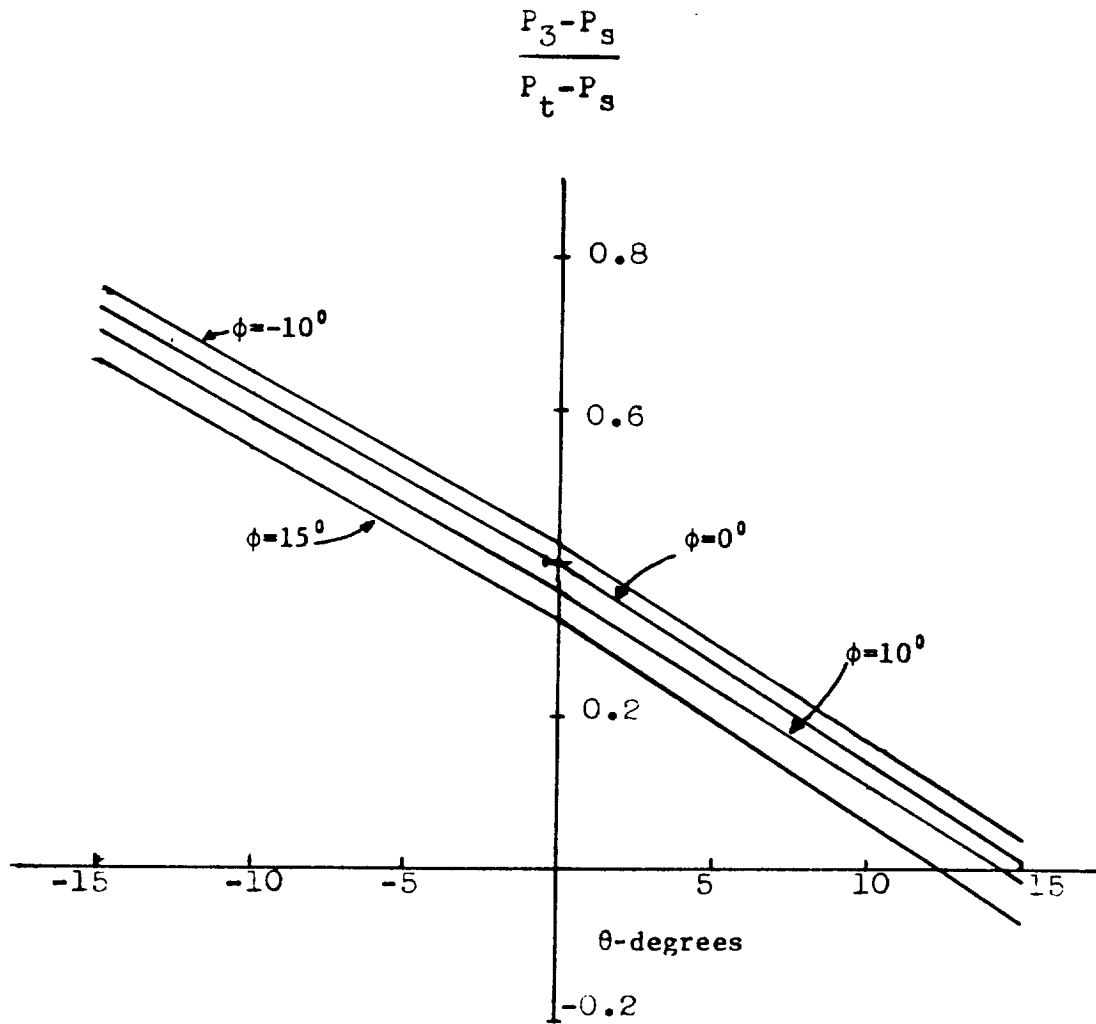
Sketch of Four-Diaphragm Probe Showing
Air Angle Definitions

Figure 2.5



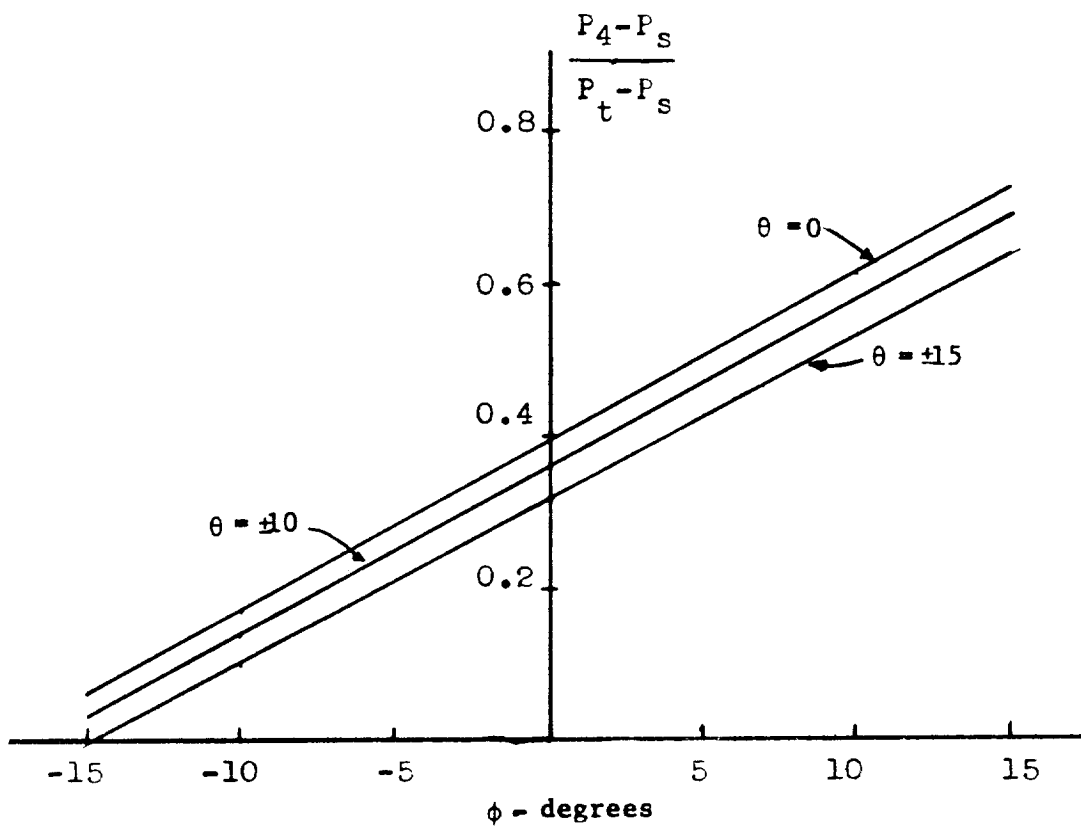
Four-Diaphragm Probe Calibration
Pressure Recovery for Diaphragm 1

Figure 2.6



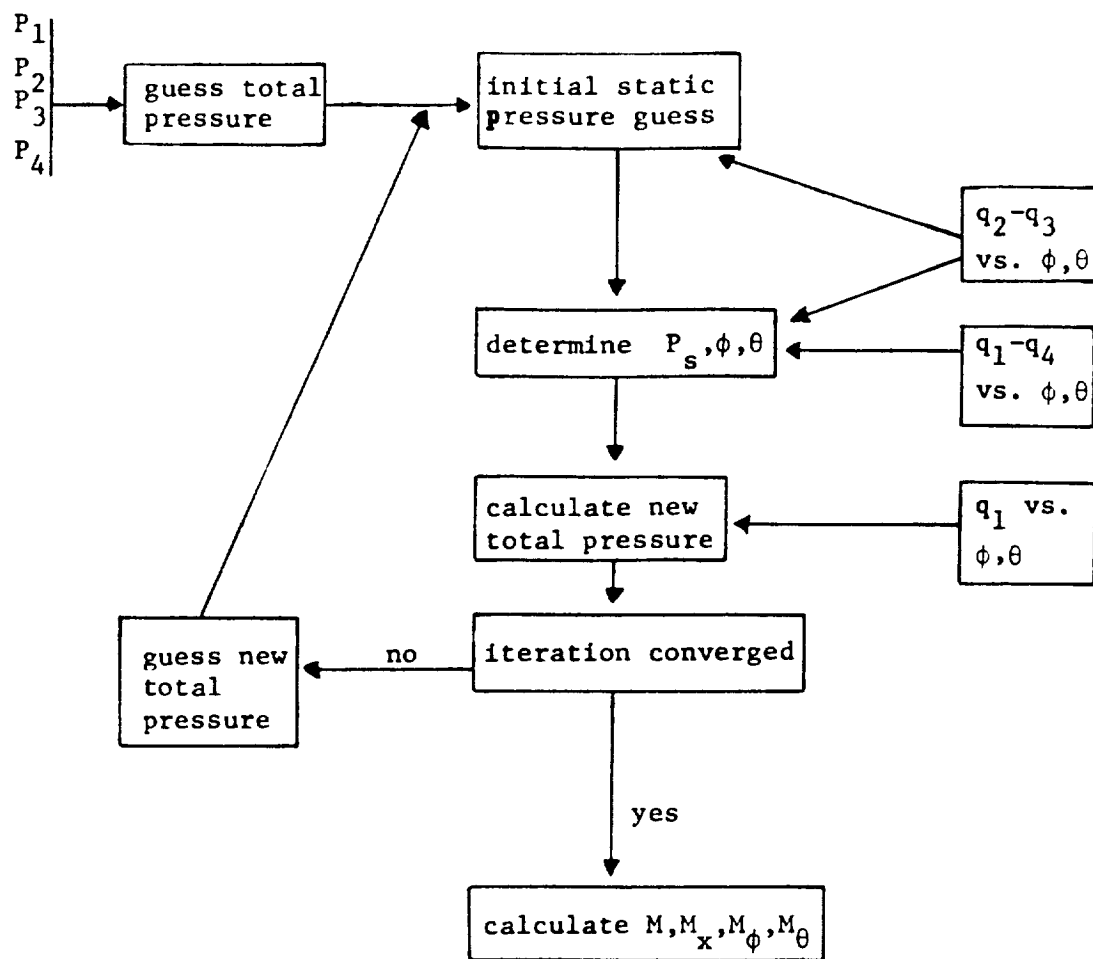
Four-Diaphragm Probe Calibration
Pressure Recovery for Diaphragm 3

Figure 2.7



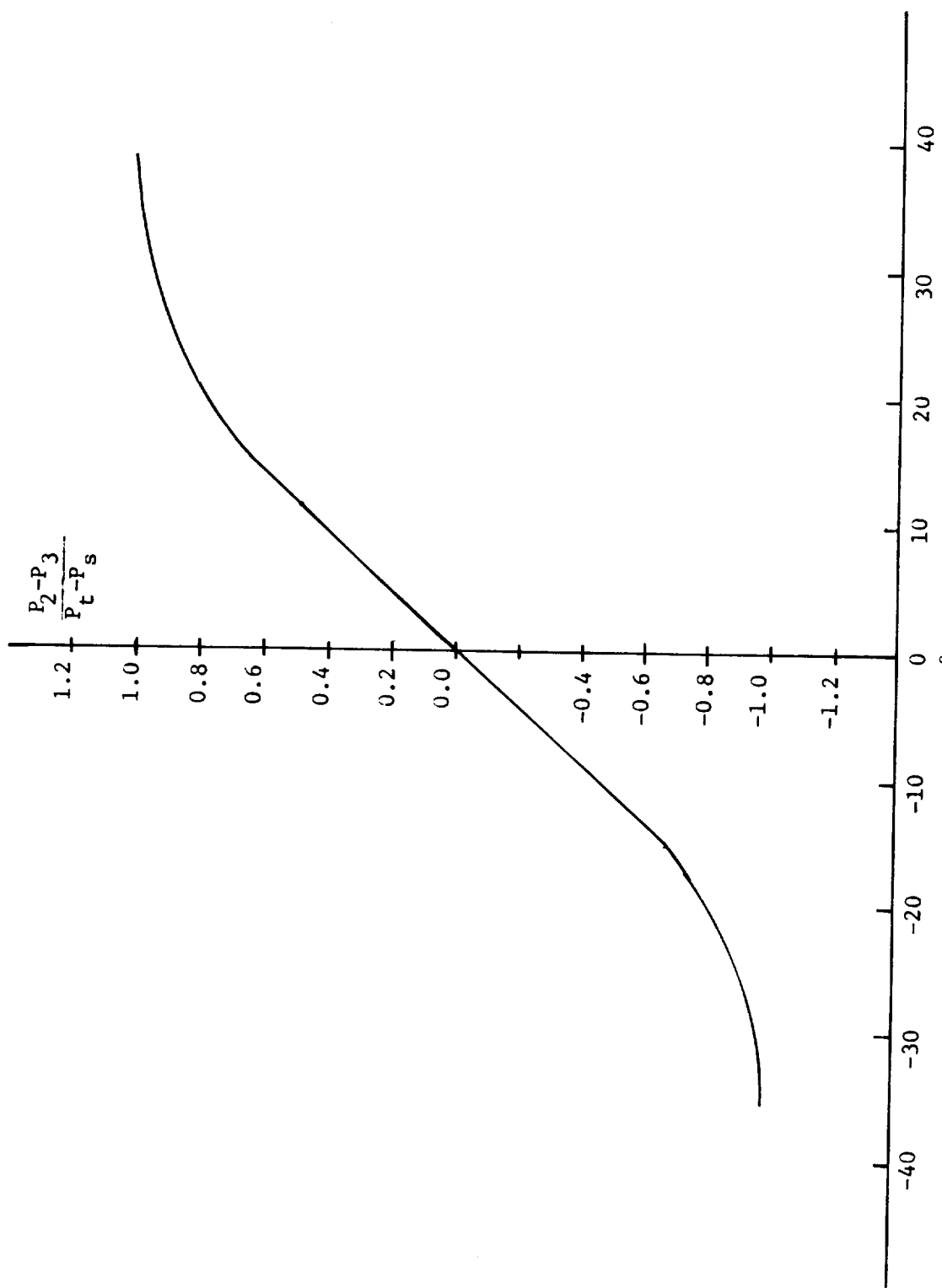
Four-Diaphragm Probe Calibration
Pressure Recovery for Diaphragm 4

Figure 2.8



Flow Chart for Four-Diaphragm Probe
Data Reduction

Figure 2.9



Sensitivity of pitch angle measurements for ϕ equal 0.0

Figure 2.10

Scale Drawing of Miniature
Stagnation Pressure Probe

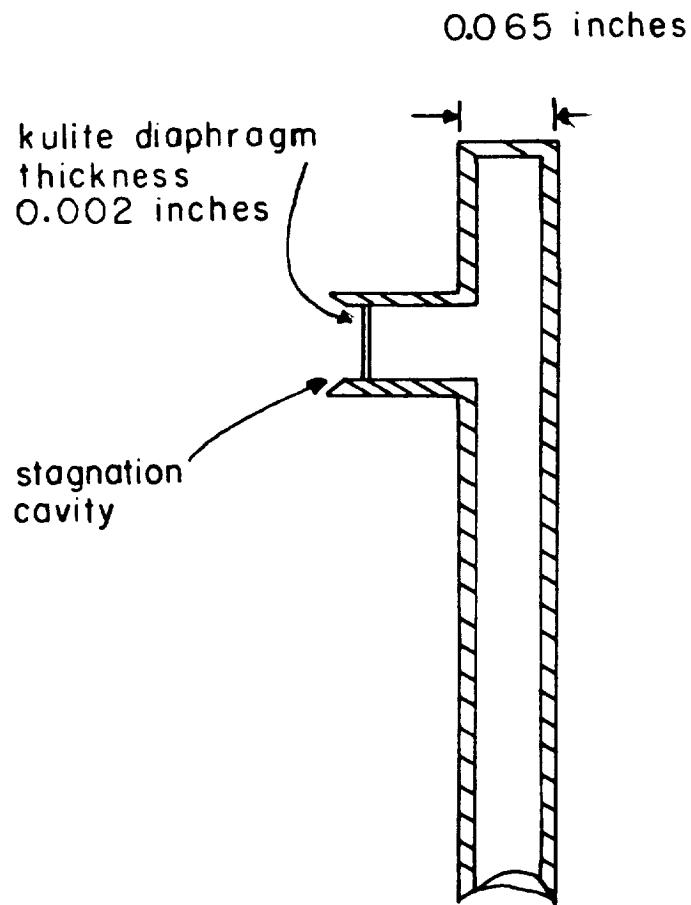
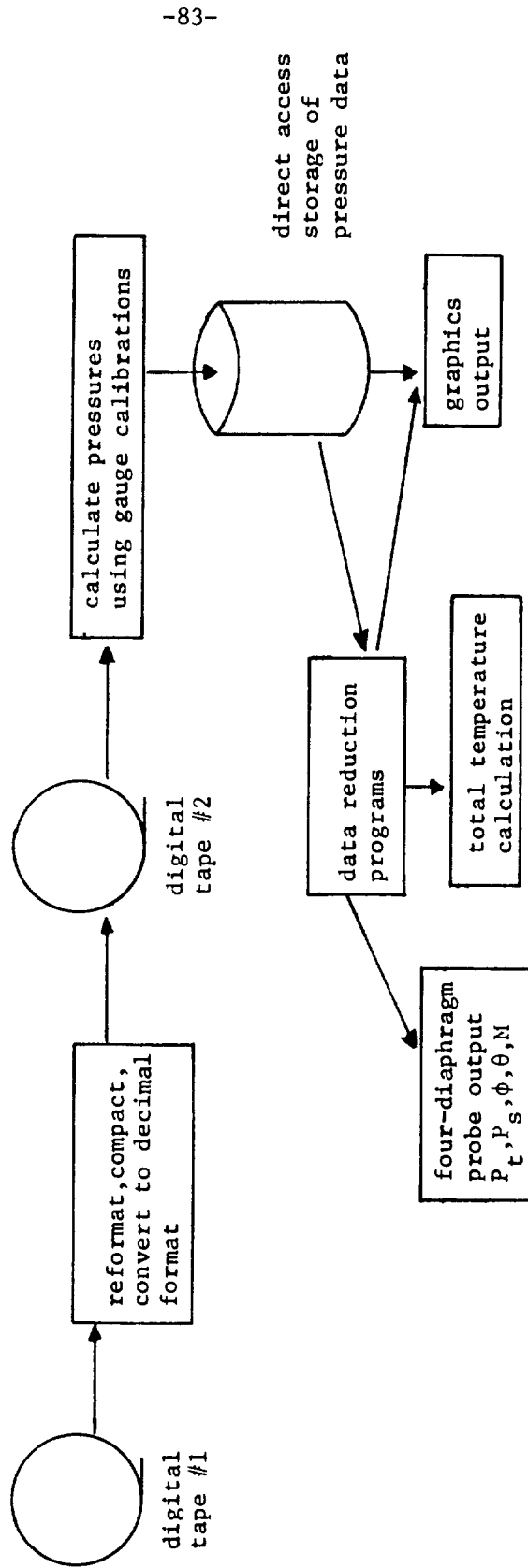
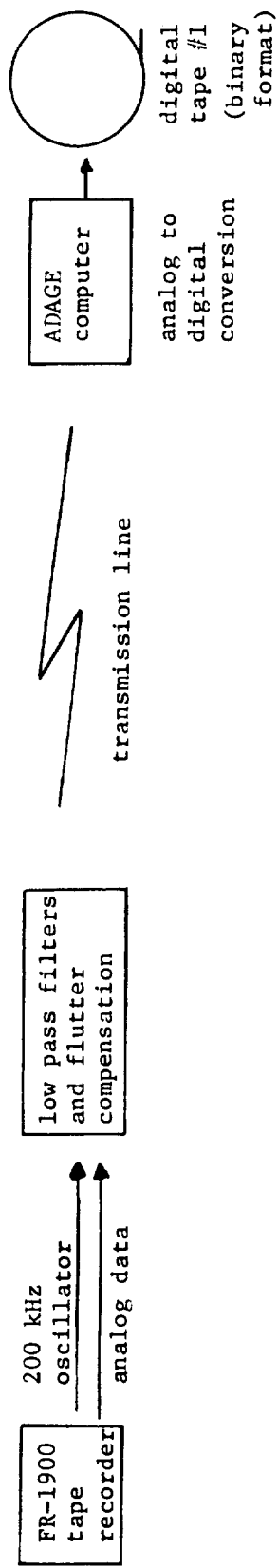


Figure 2.11



Flow Chart for Analog to Digital Conversion and Digital Data Reduction Programs

Figure 2.12

TOTAL AND STATIC PRESSURE RATIOS
 $R/RT = 0.738$
 0.1 AXIAL CHORDS DOWNSTREAM OF ROTOR

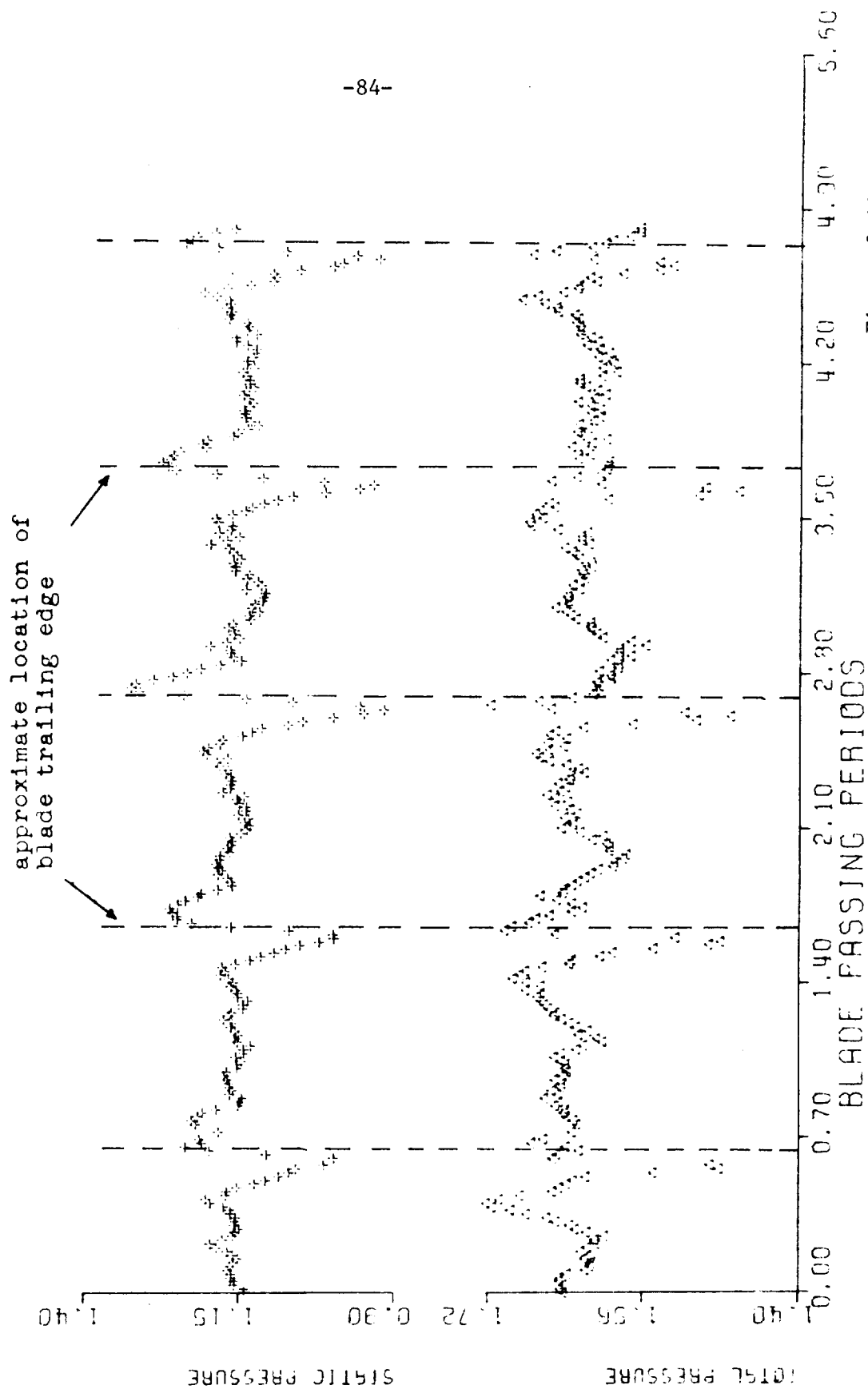


Figure 2.13

MACH NUMBER COMPONENTS
 $R/RT = 0.738$
 0.1 AXIAL CHORDS DOWNSTREAM OF ROTOR

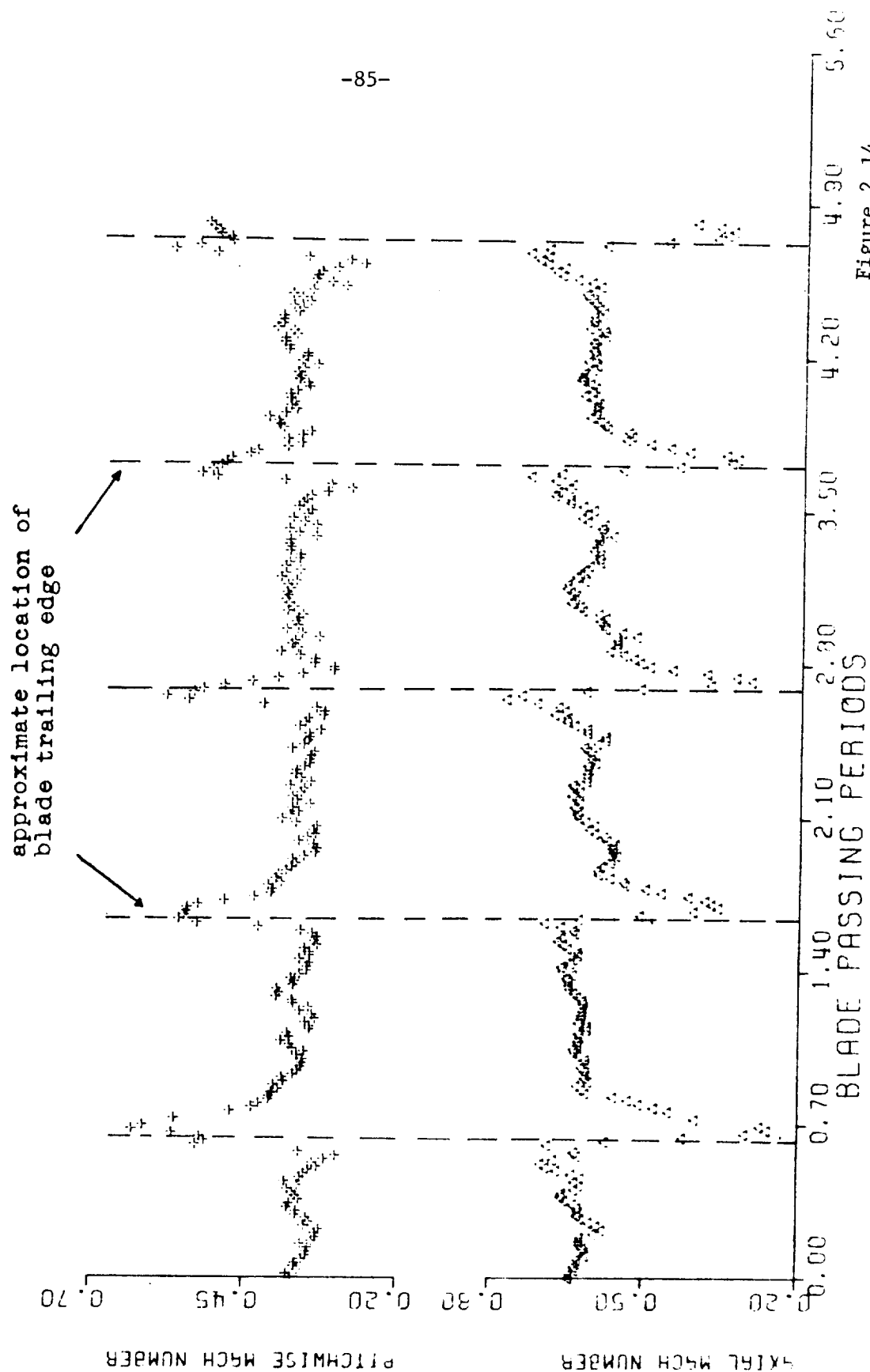
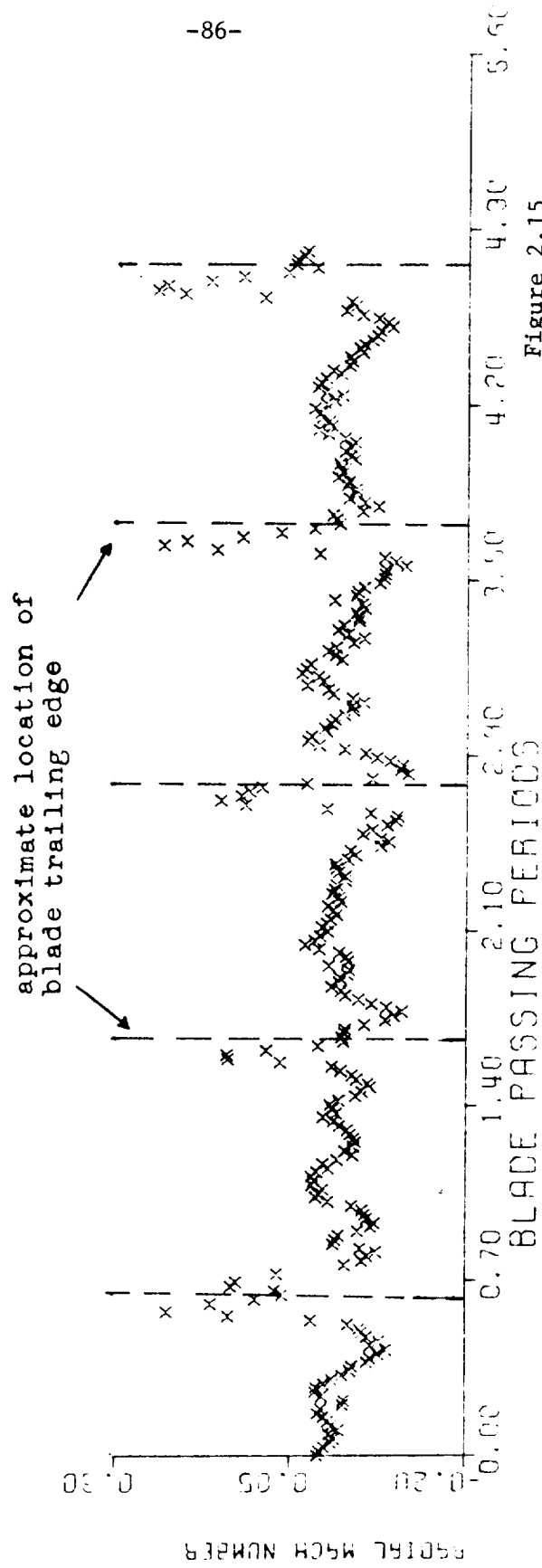


Figure 2.14

MACH NUMBER COMPONENTS
 $R/RT = 0.738$
 0.1 AXIAL CHORDS DOWNSTREAM OF ROTOR



TOTAL AND STATIC PRESSURE RATIOS
 $R/RT = 0.870$
 0.1 AXIAL CHORDS DOWNSTREAM OF ROTOR

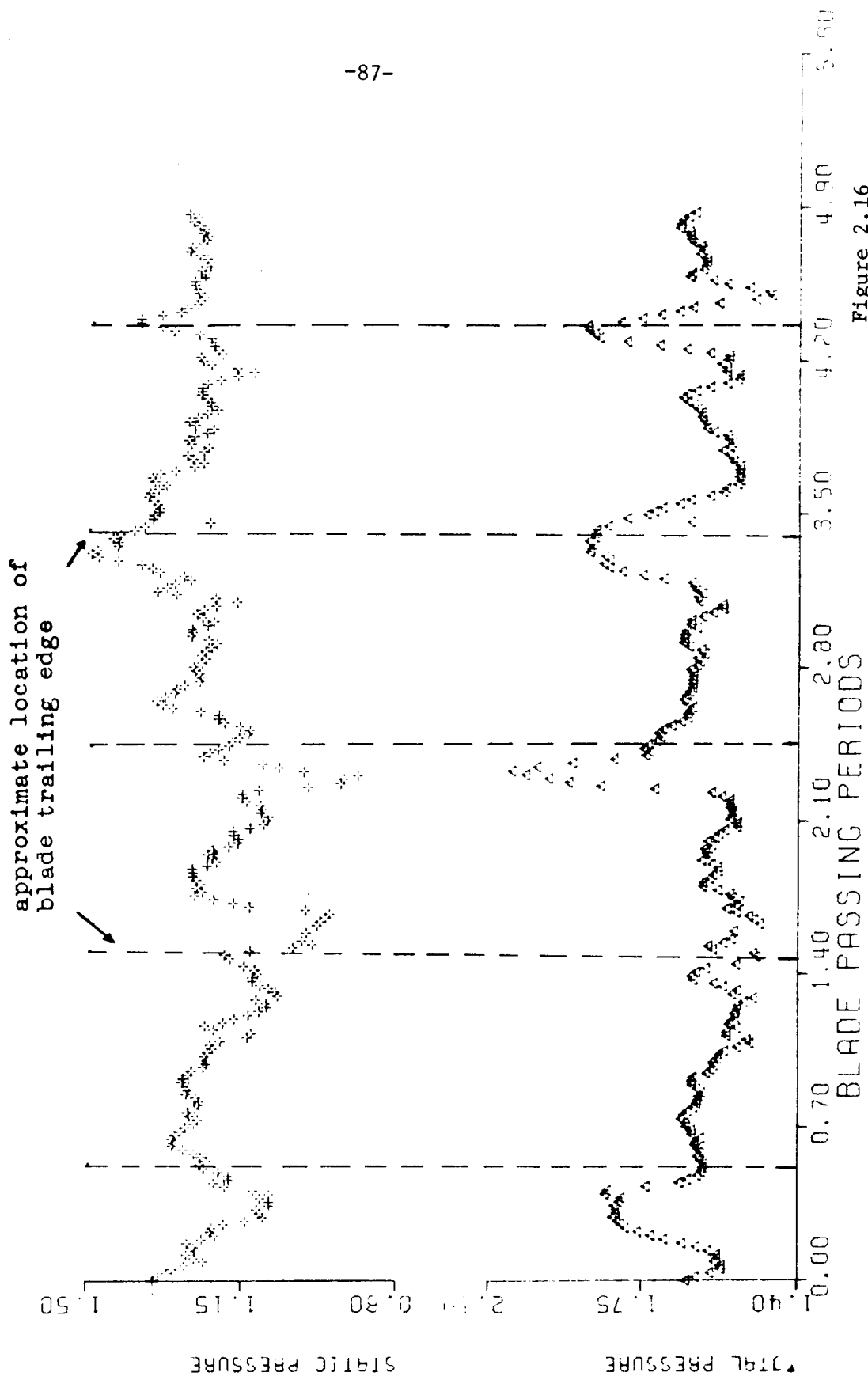


Figure 2.16

RADIAL AND PITCHWISE FLOW ANGLES
 $R/RT = 0.870$
 0.1 AXIAL CHORDS DOWNSTREAM OF ROTOR

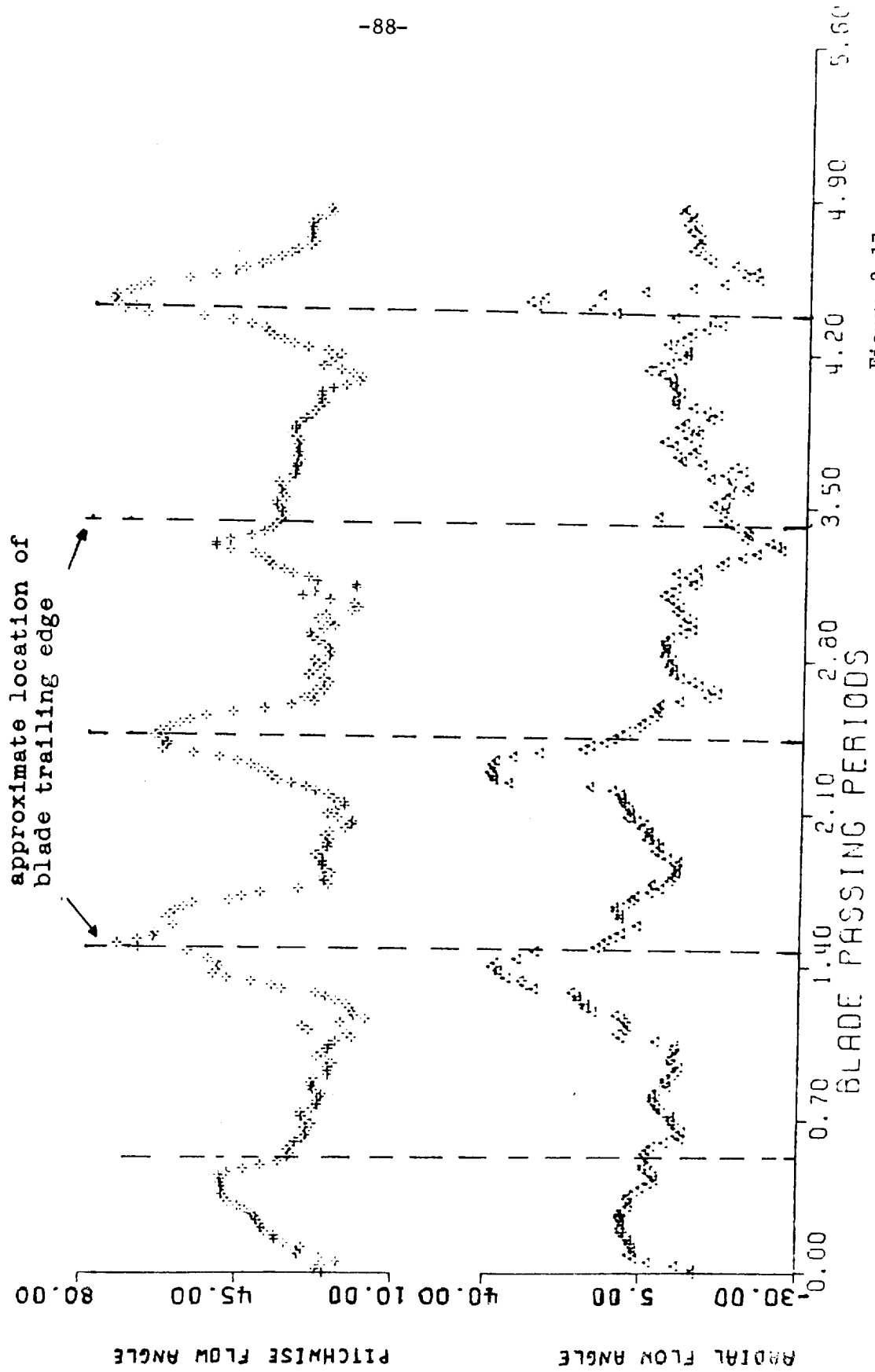


Figure 2.17

MACH NUMBER COMPONENTS
 $R/RT = 0.870$
 0.1 AXIAL CHORDS DOWNSTREAM OF ROTOR

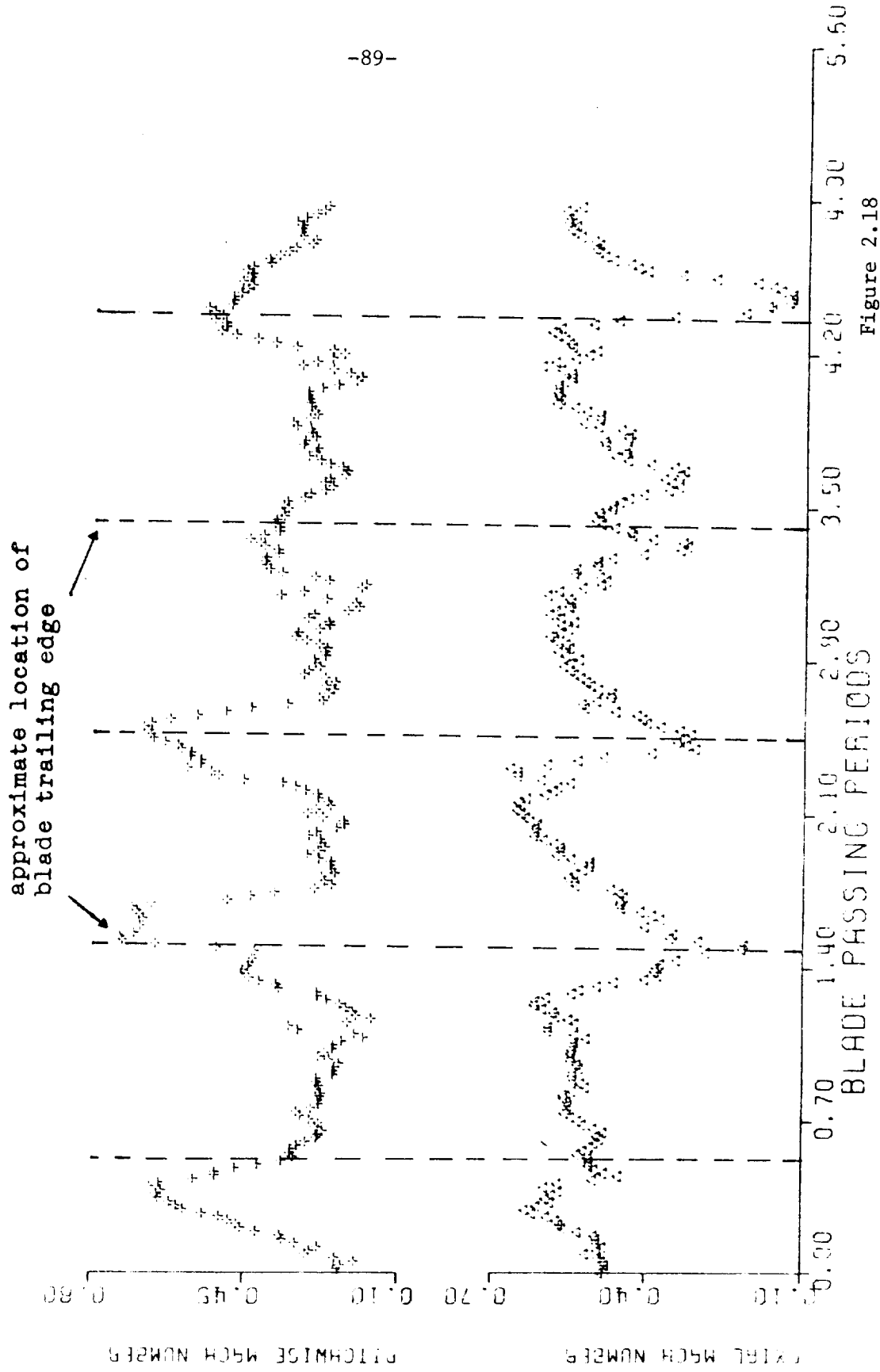


Figure 2.18

MACH NUMBER COMPONENTS
 $R/RT = 0.870$
 0.1 AXIAL CHORDS DOWNSTREAM OF ROTOR

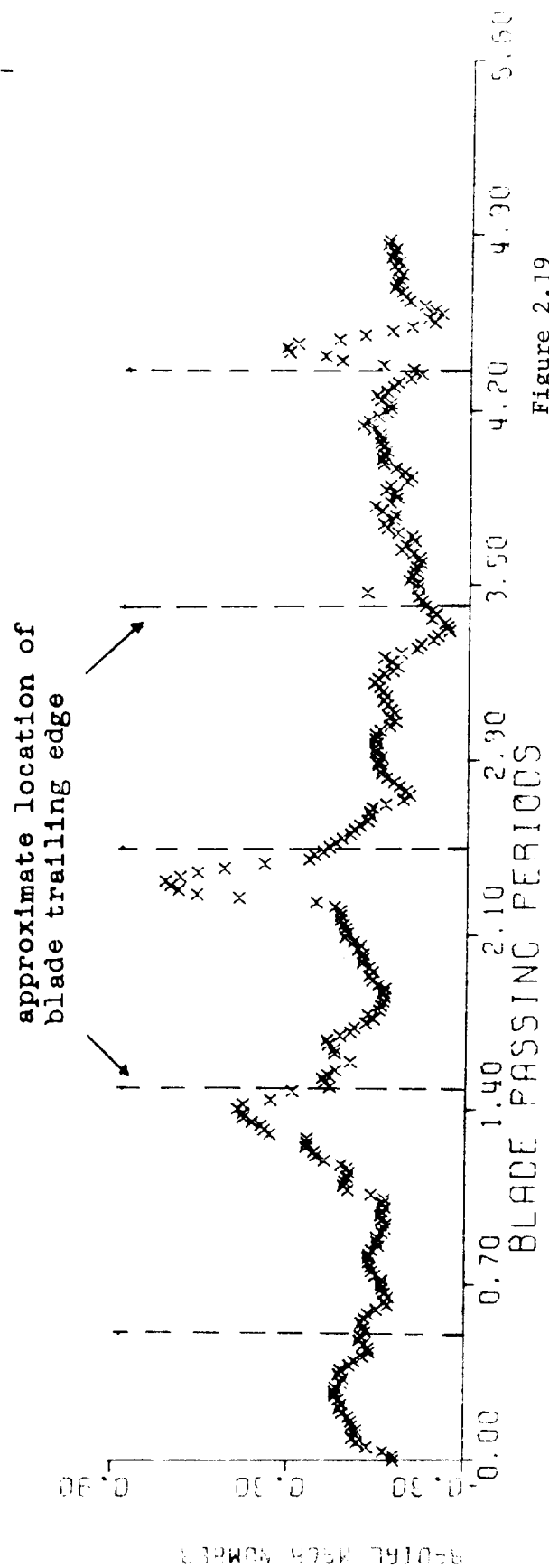


Figure 2.19

Comparison of Miniature Stagnation Probe
Measurements to Four-Diaphragm Probe
Measurements $r/r_t = 0.87$
0.1 Axial Chords Downstream of Rotor

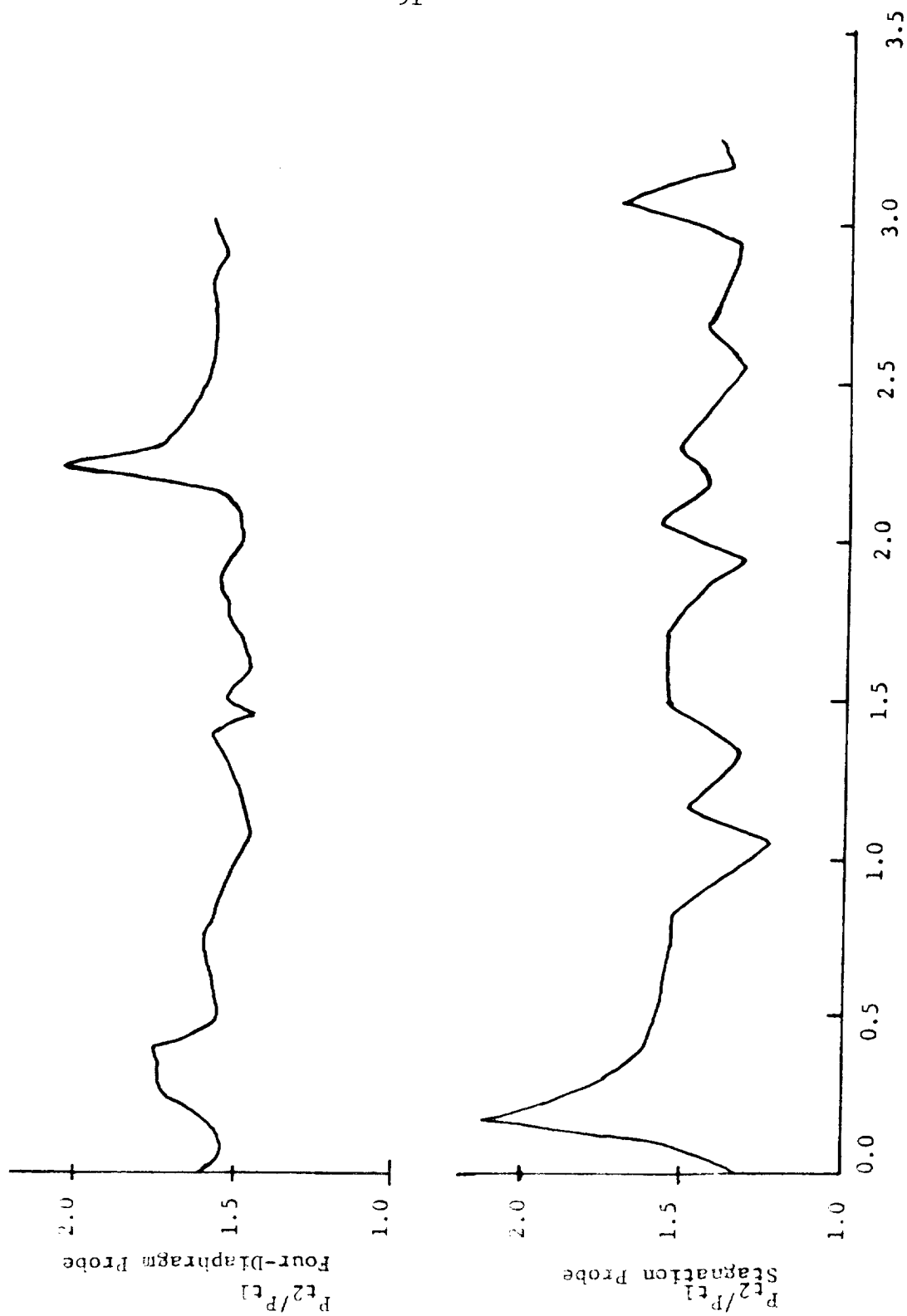


Figure 2.20

PRESSURE AND TEMPERATURE RATIOS
 $R/RT = 0.738$
 0.1 AXIAL CHORDS DOWNSTREAM OF ROTOR

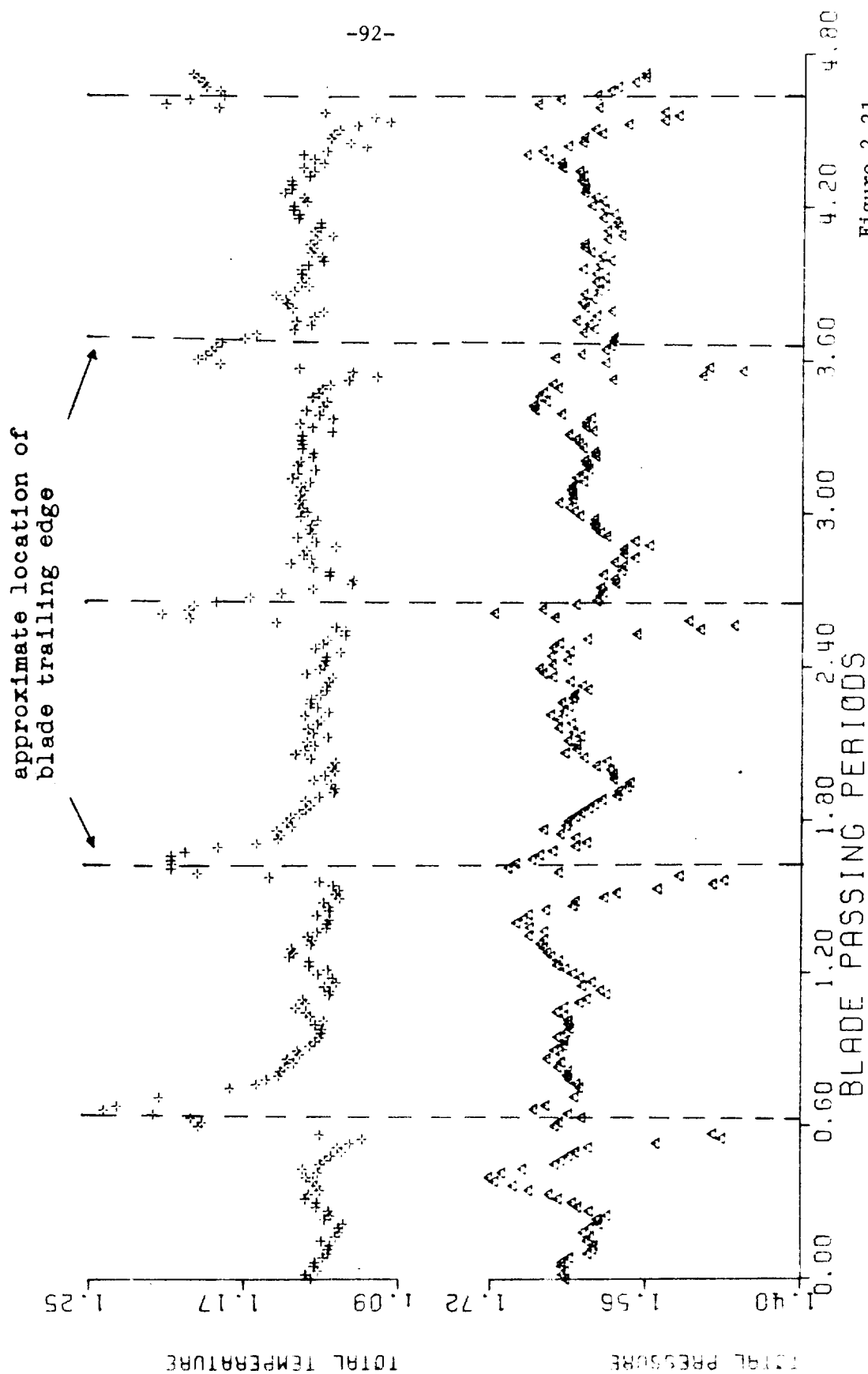


Figure 2.21

Mass Averaged Total Pressure and
Total Temperature ratios

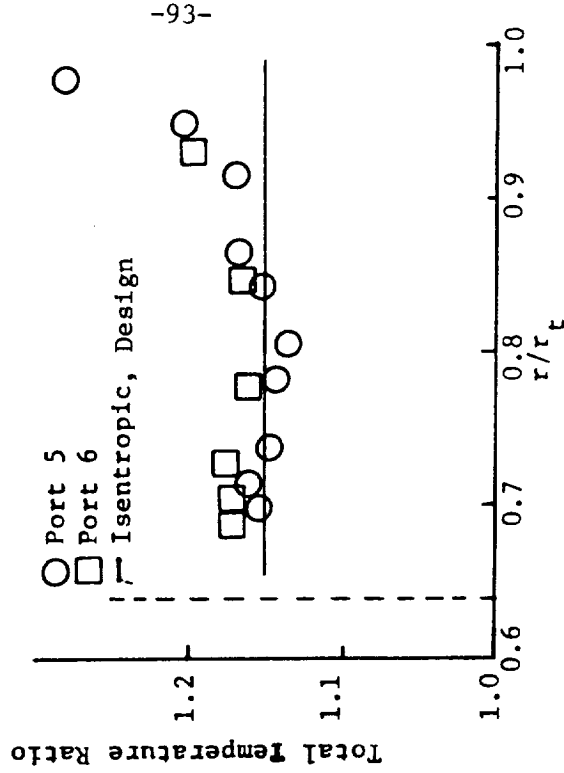
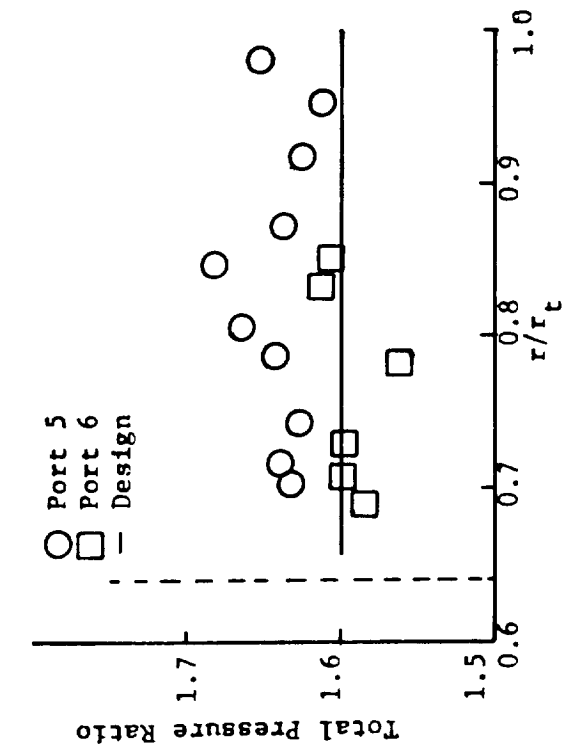


Figure 2.22

Mass Averaged Mach Number Profiles

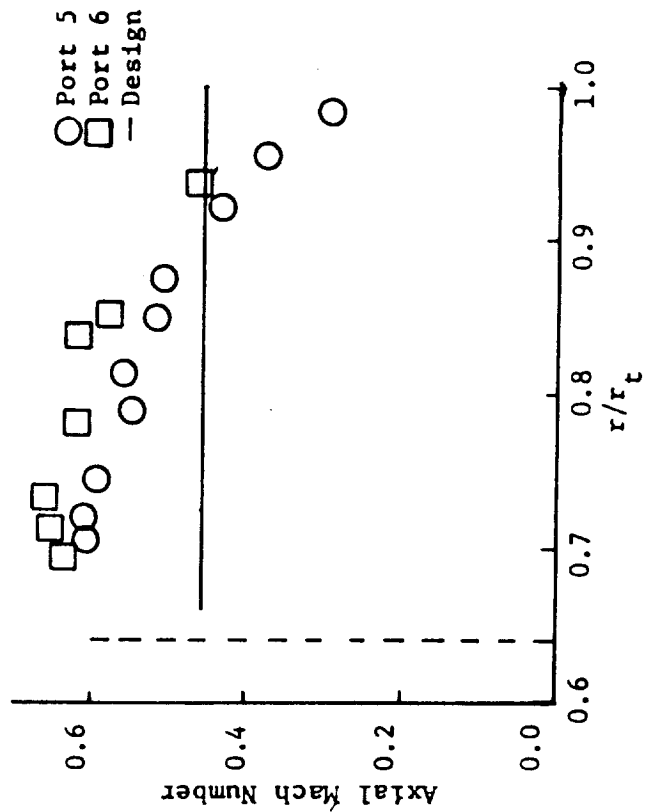
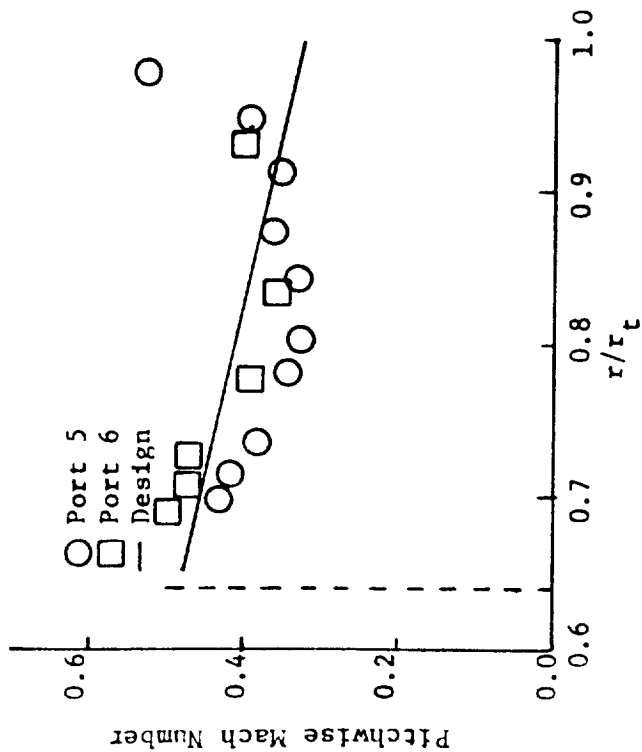


Figure 2.23

TOTAL PRESSURE RATIO MAP

0.1 CHORDS DOWNSTREAM OF ROTOR

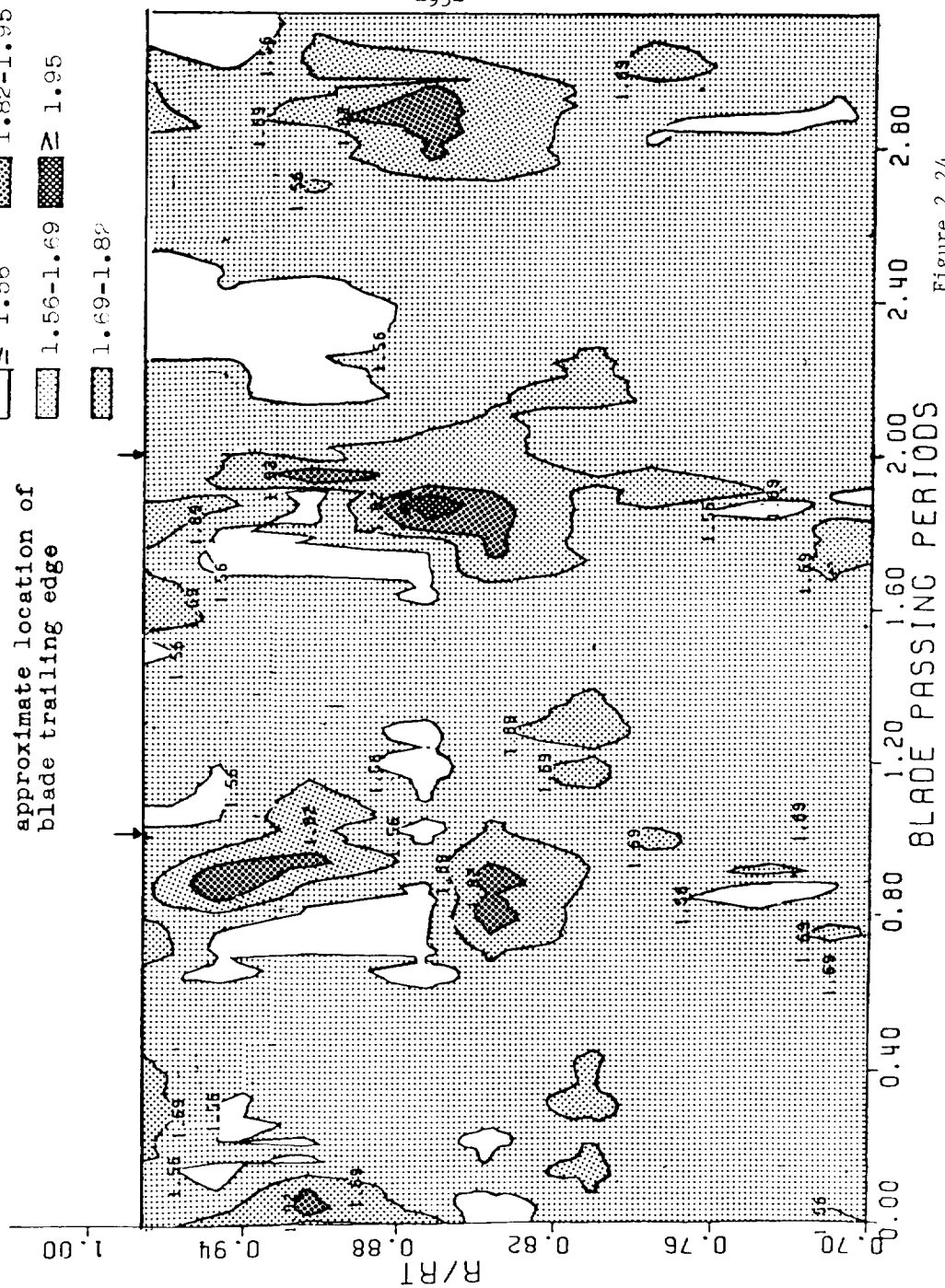
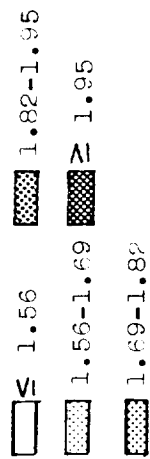


Figure 2.24

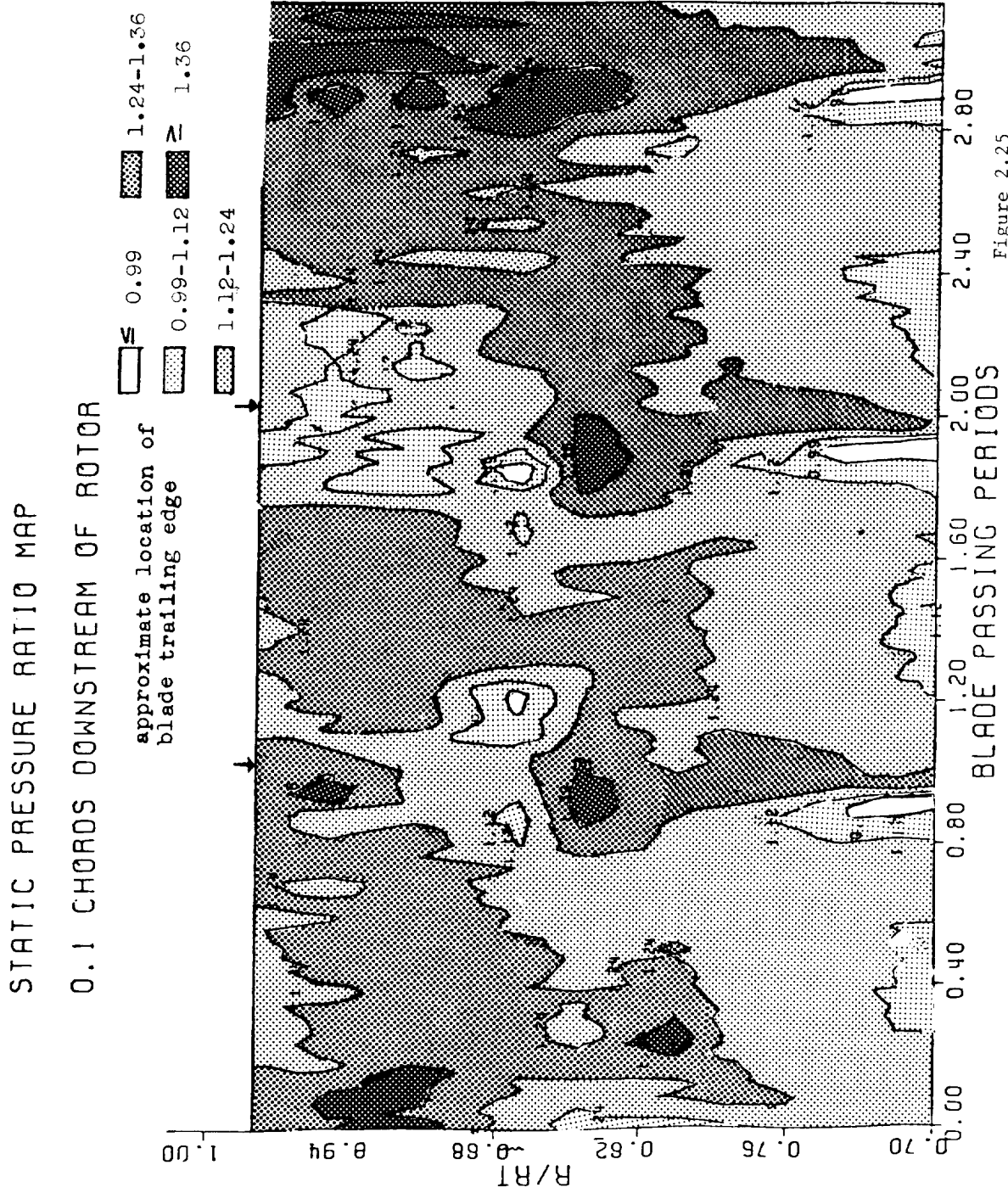


Figure 2.25

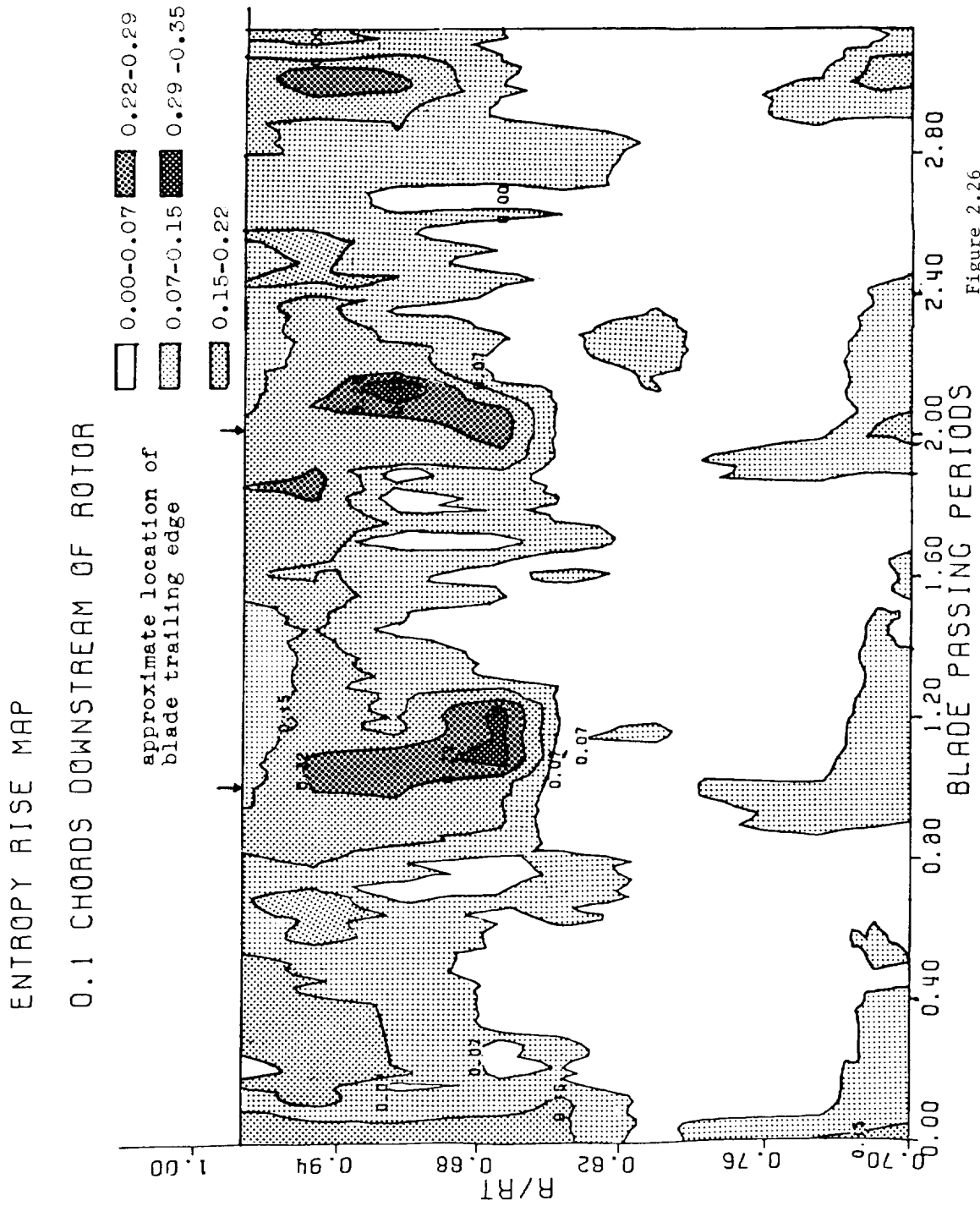
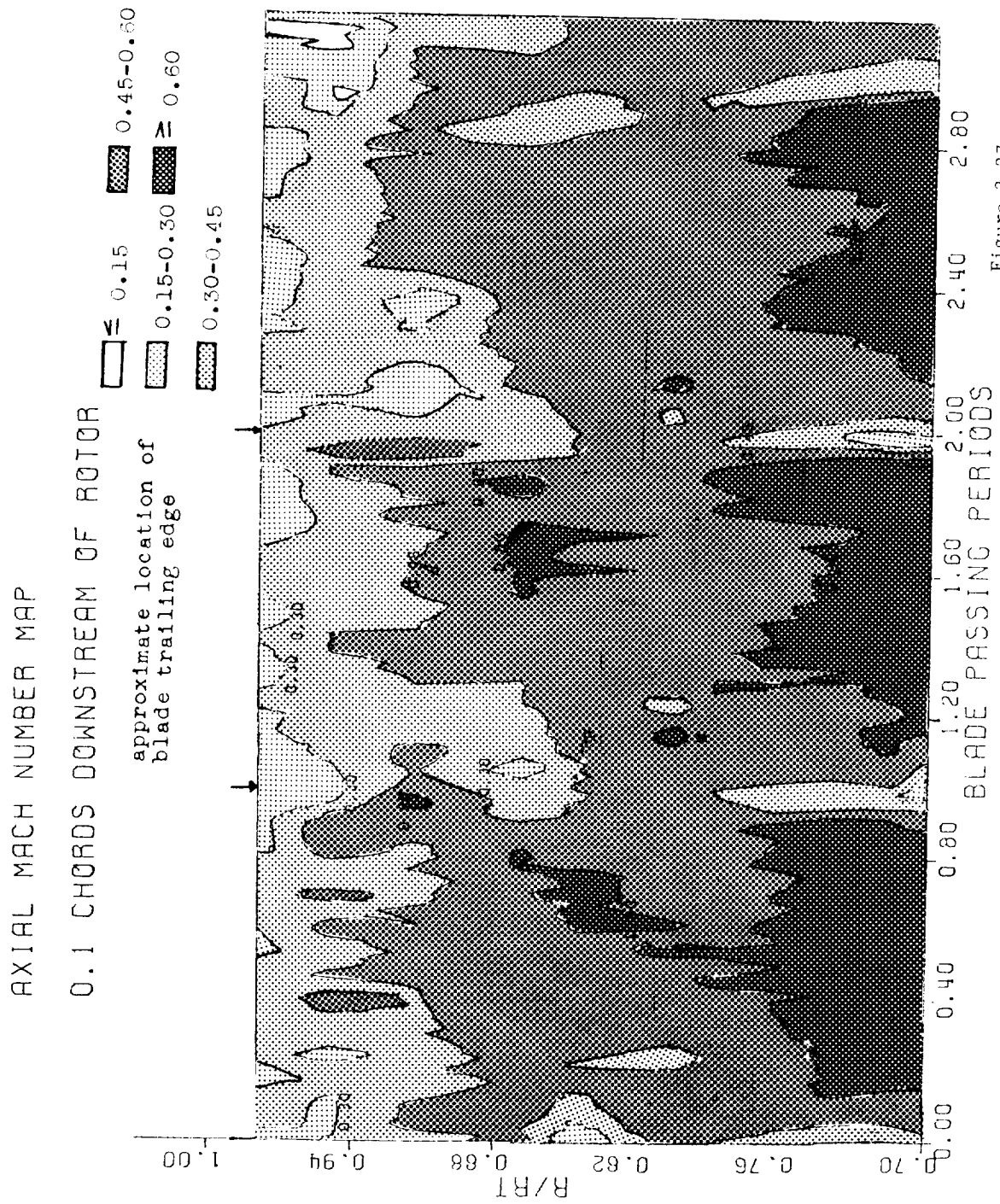
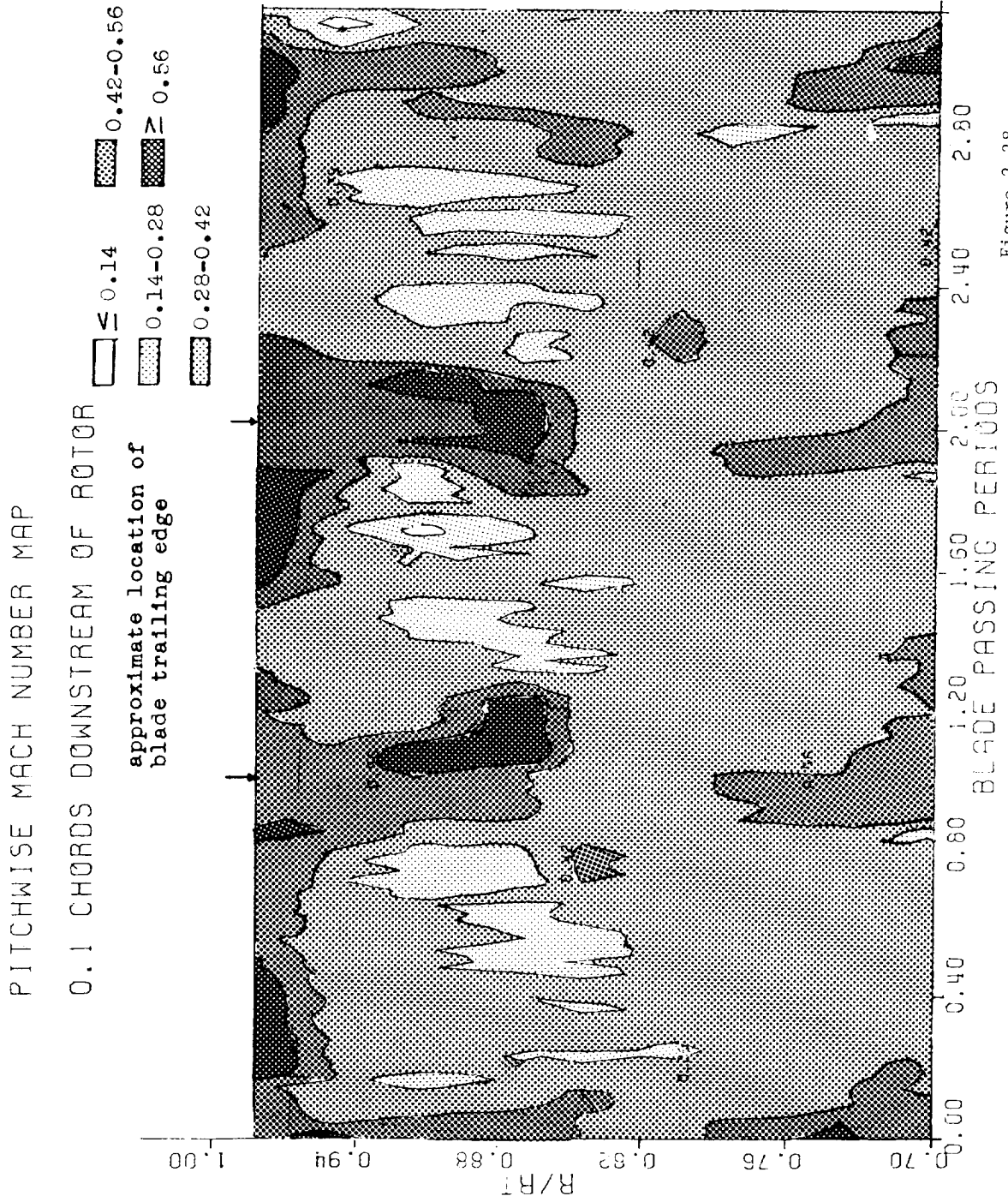
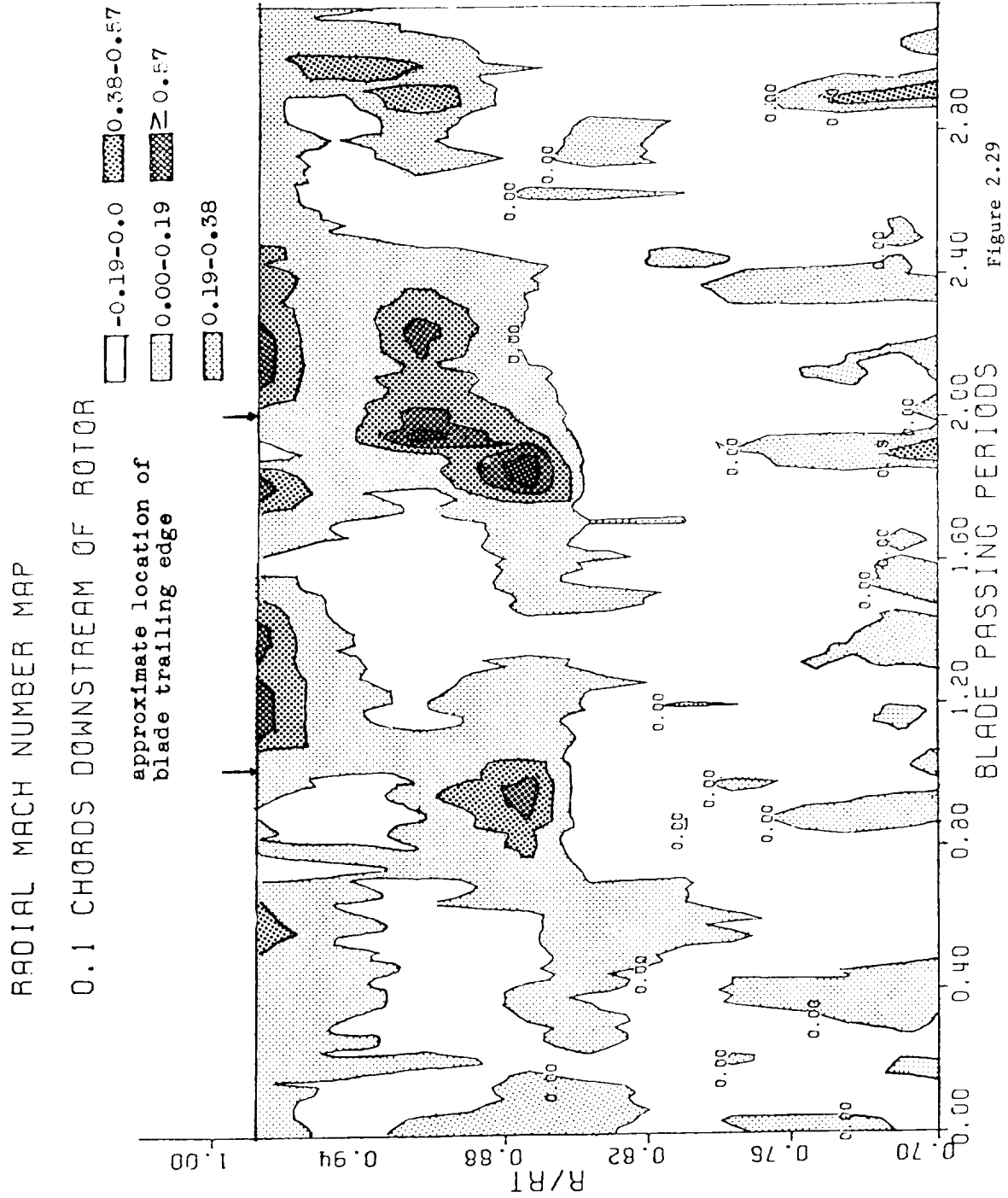


Figure 2.26







TOTAL TEMPERATURE RATIO MAP
0.1 CHORDS DOWNSTREAM OF ROTOR

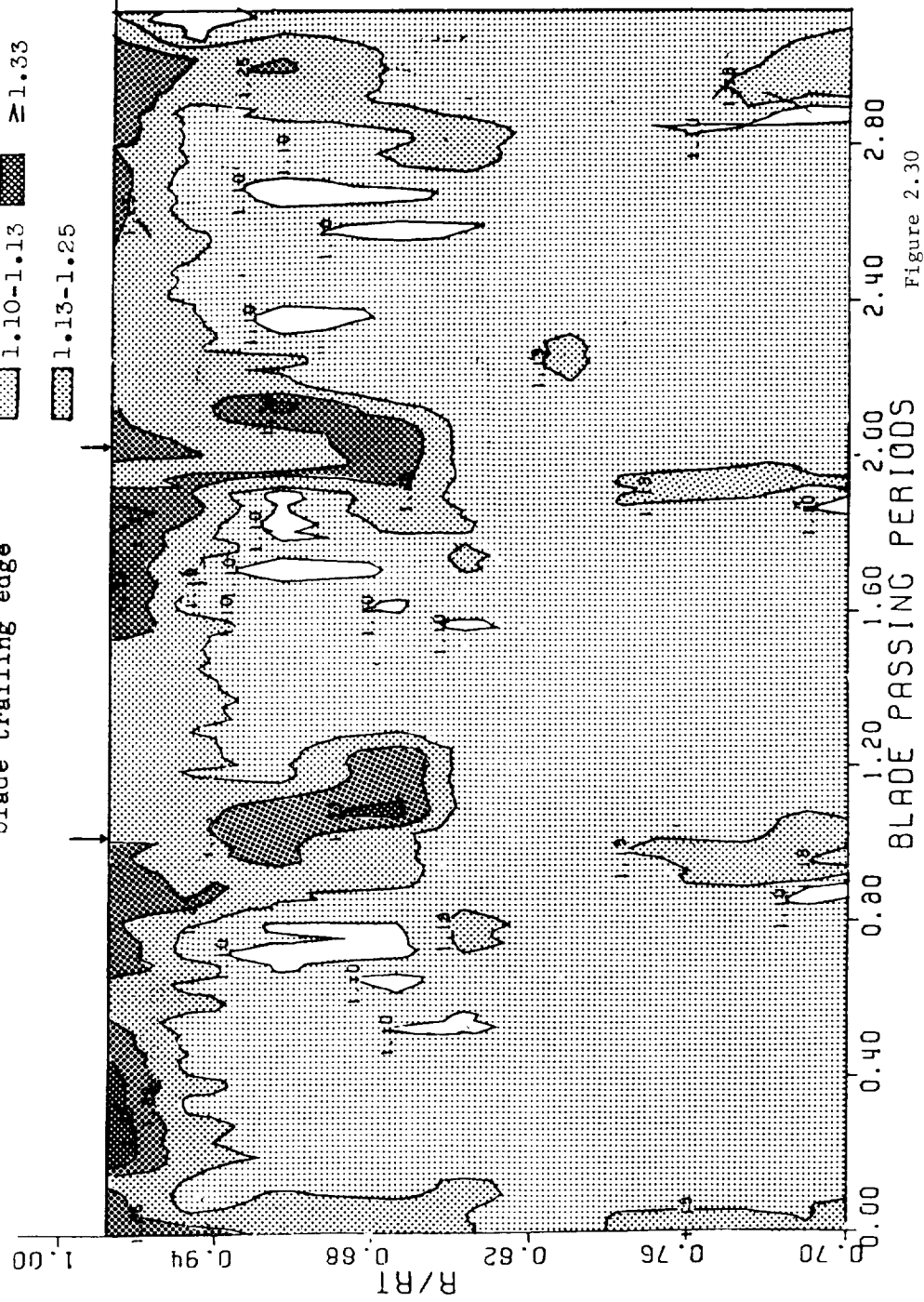
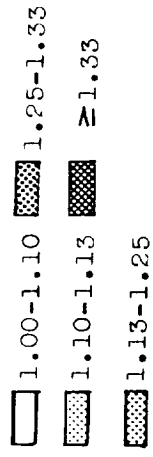
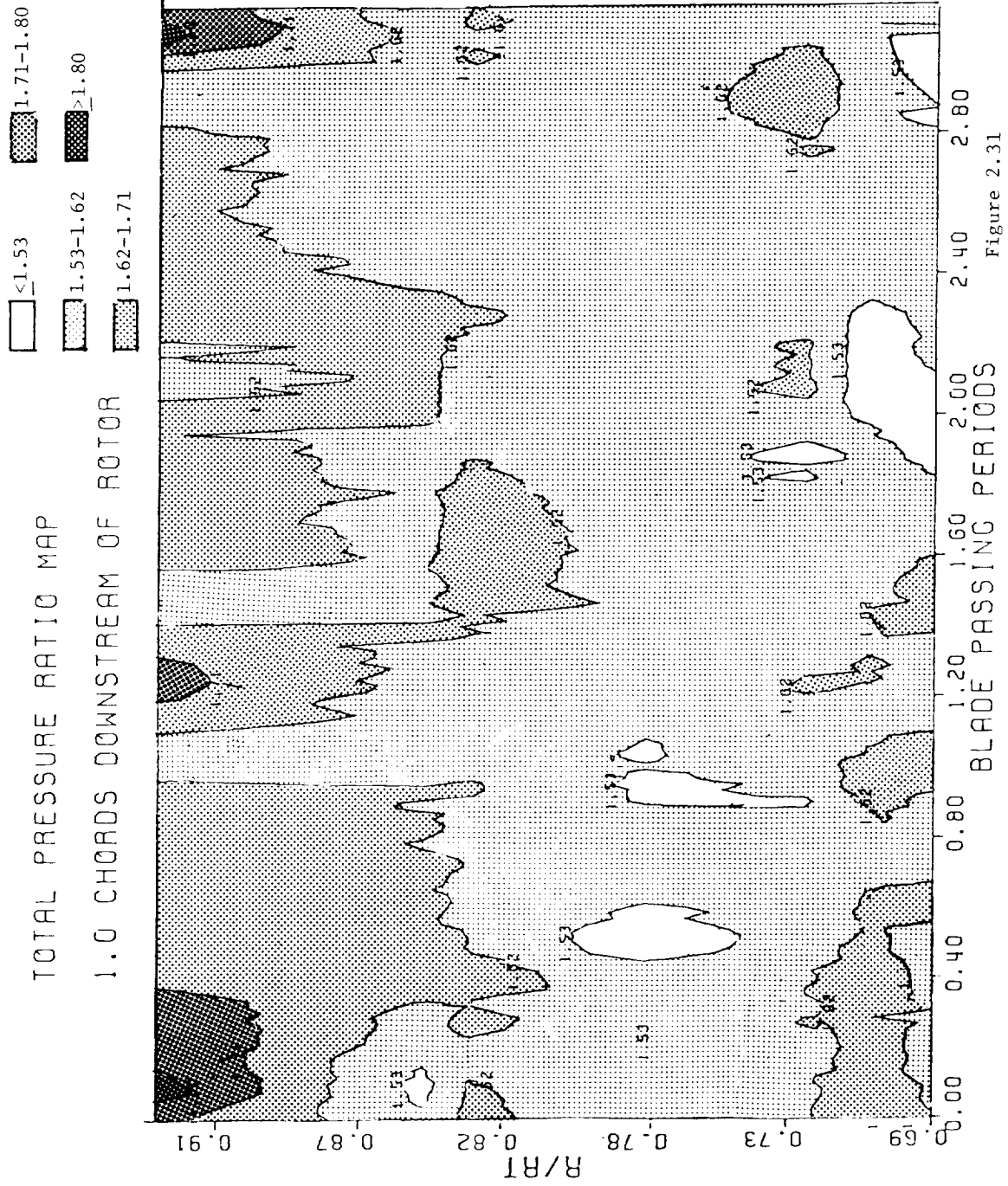
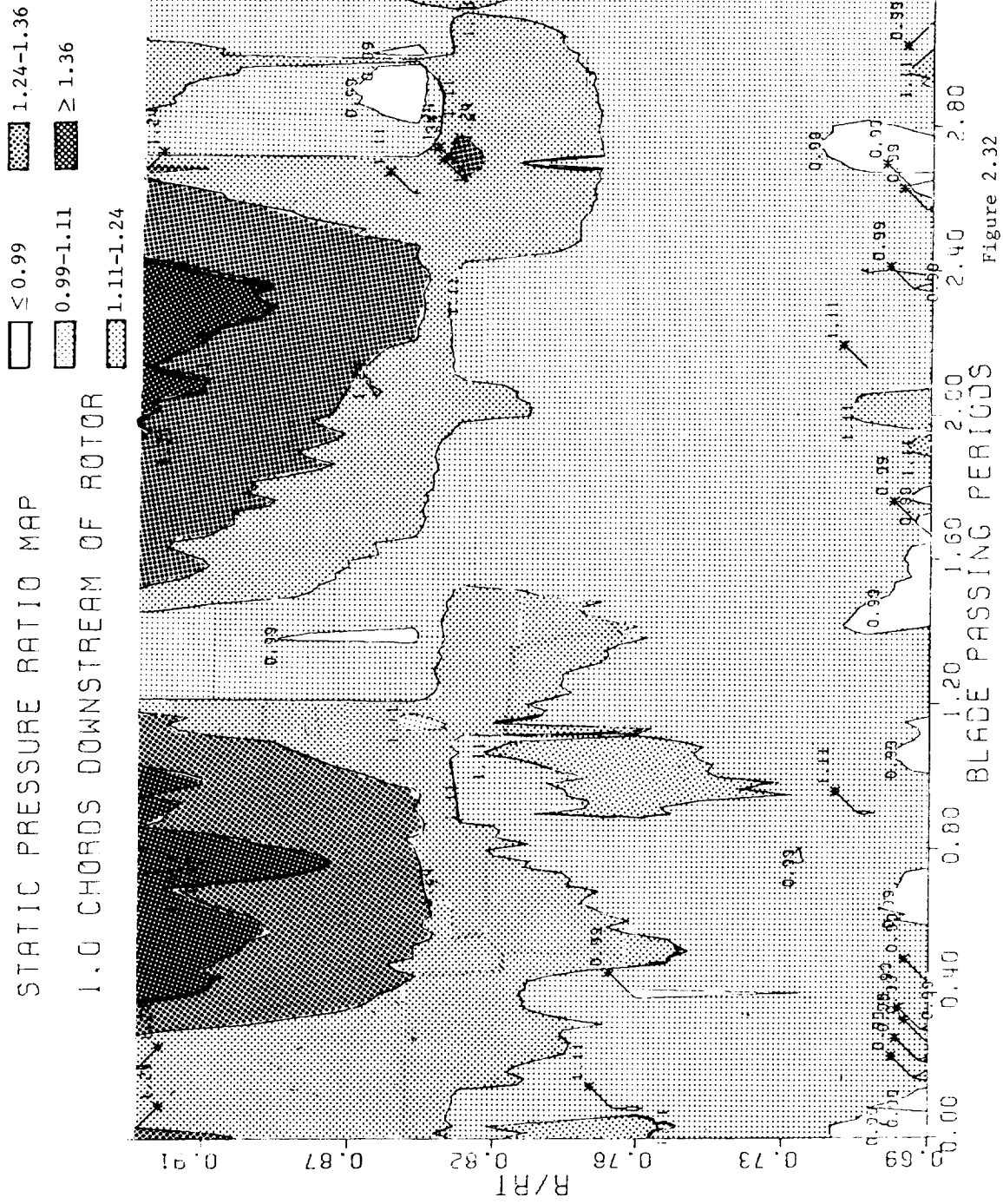


Figure 2.30





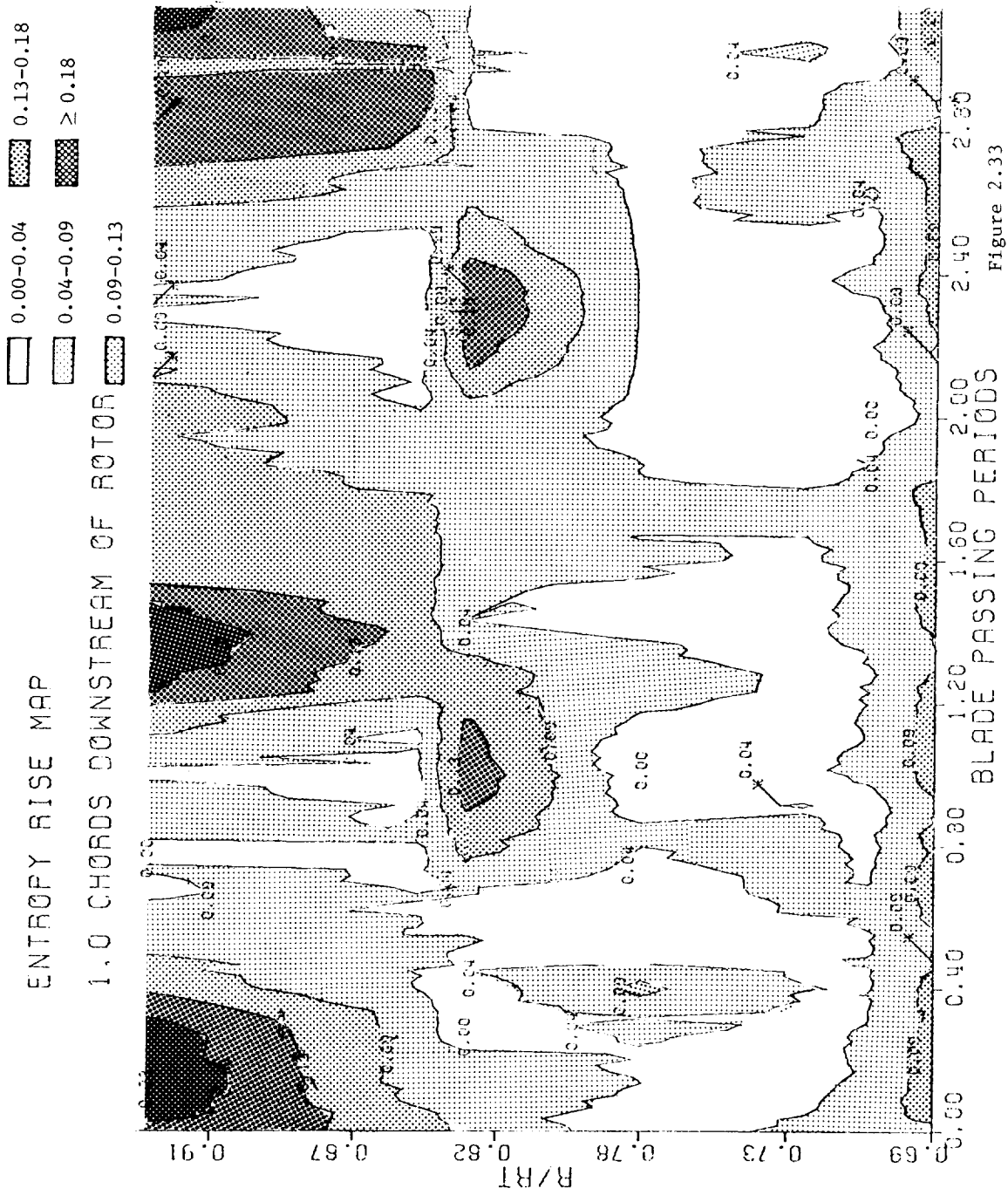
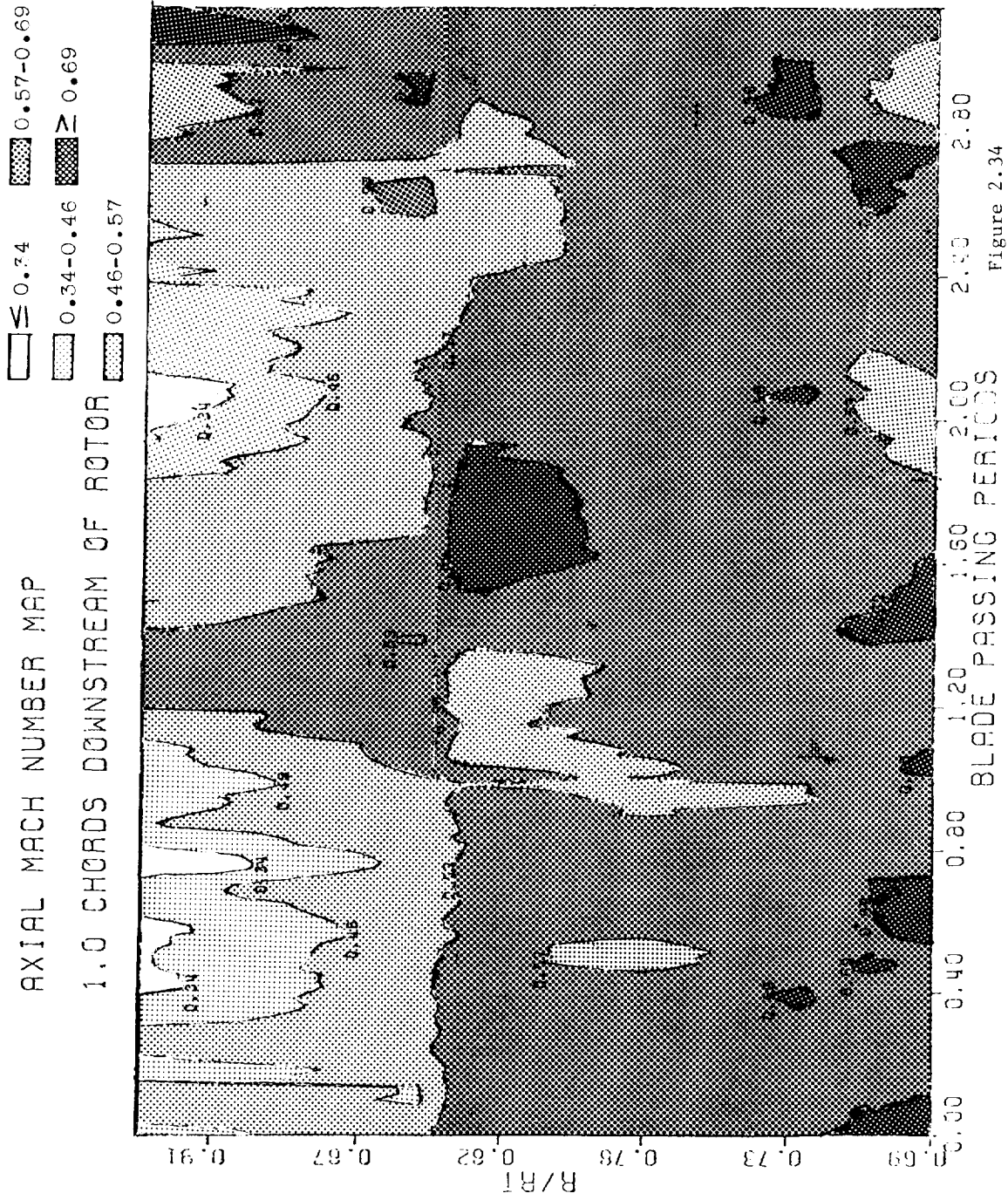
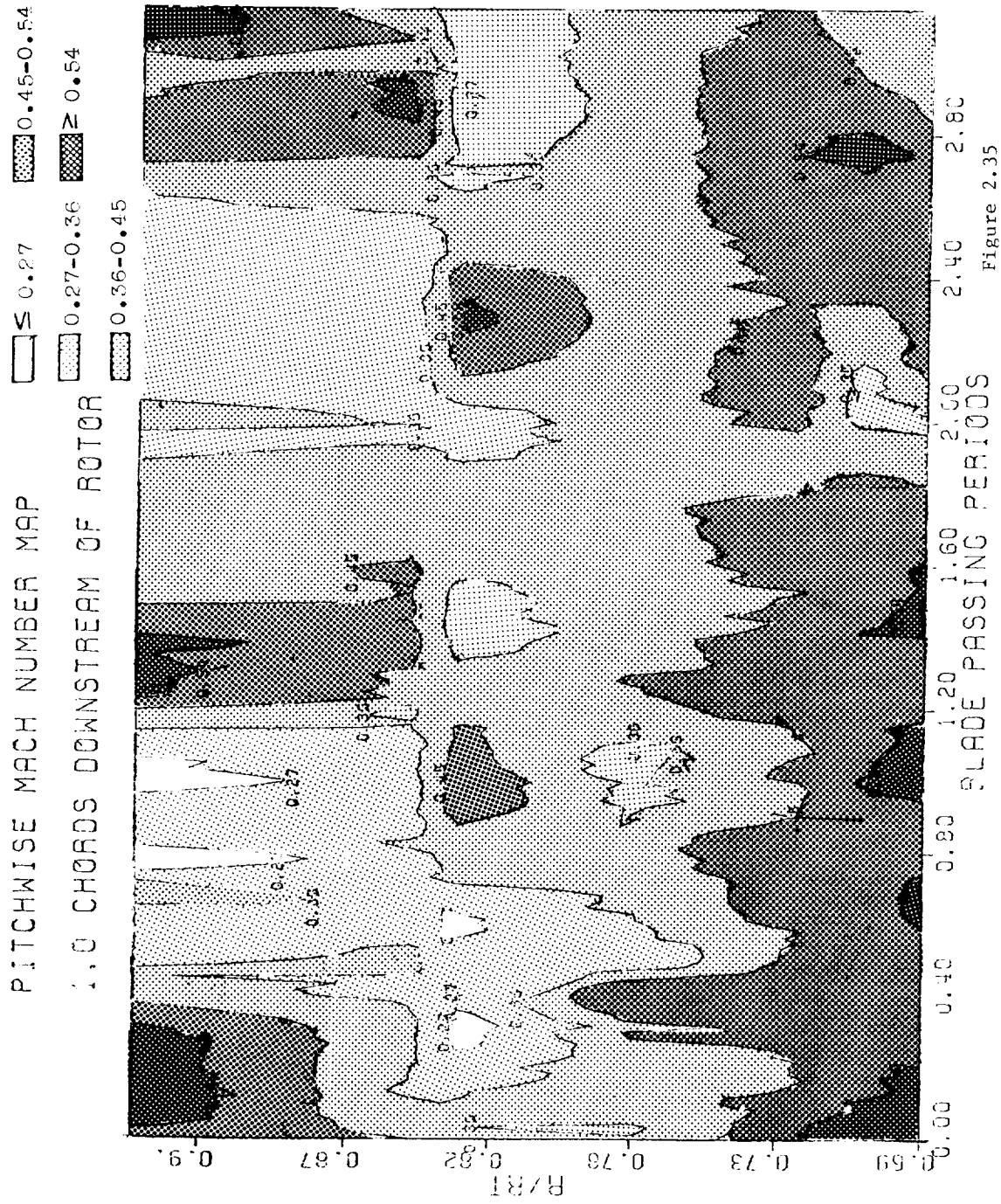
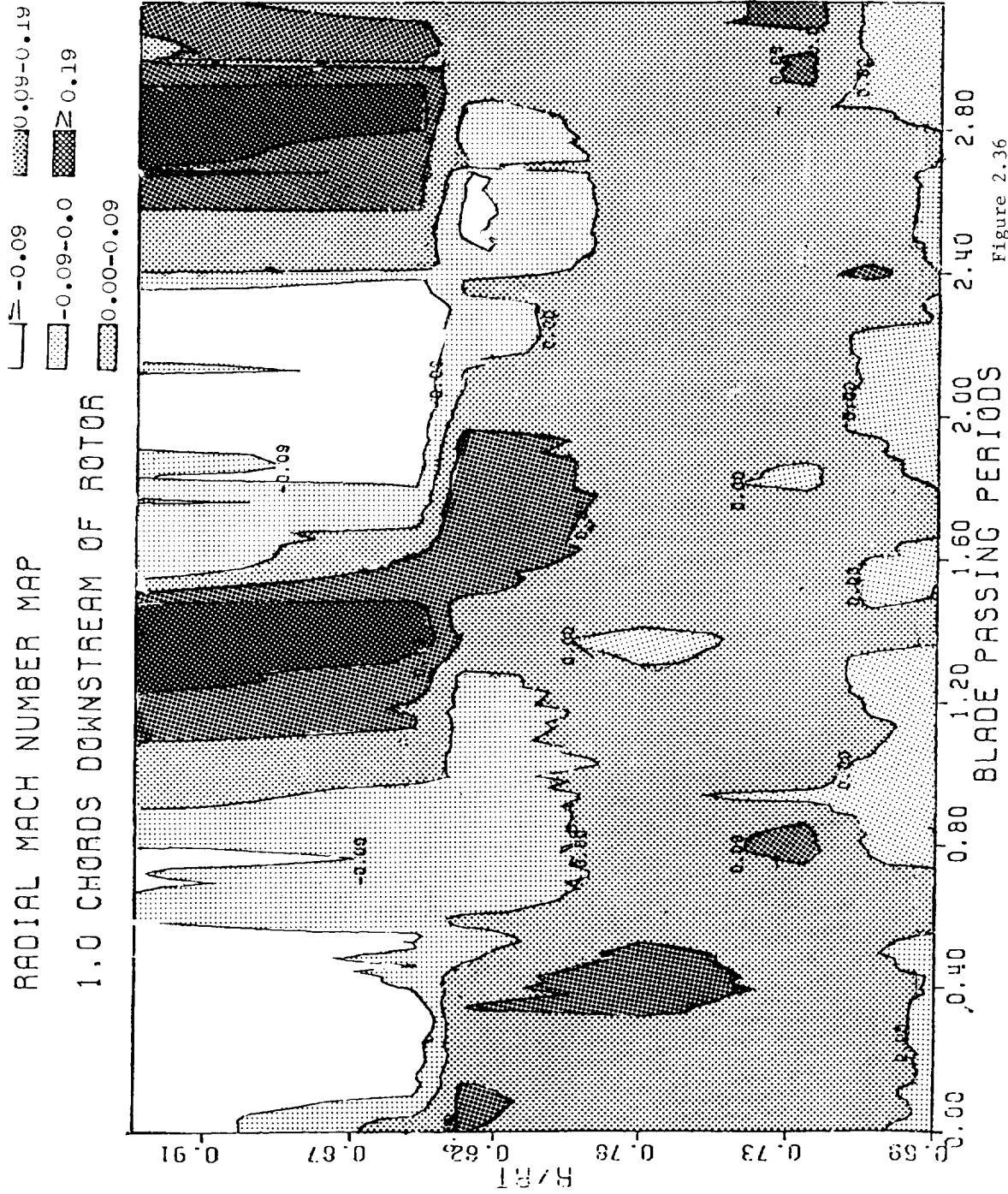
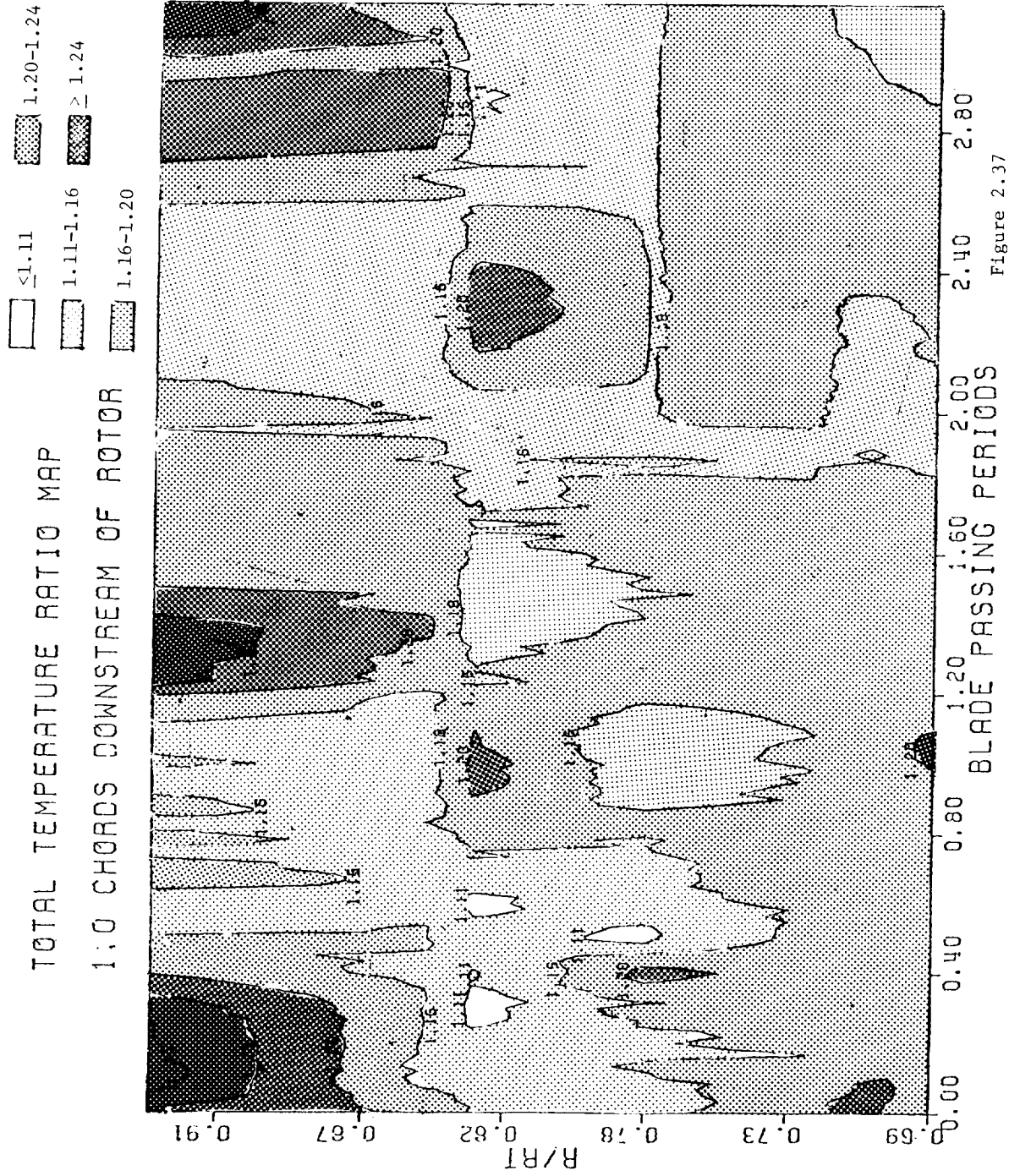


Figure 2.33





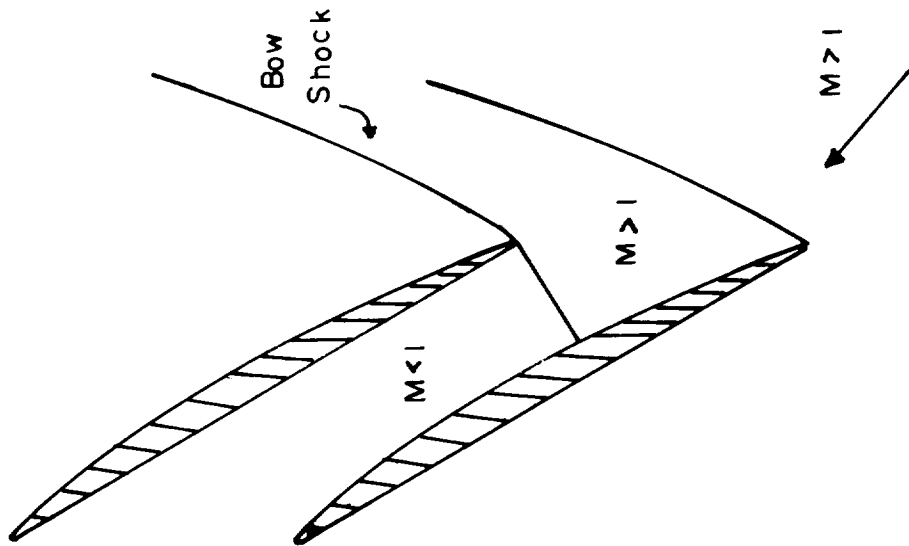






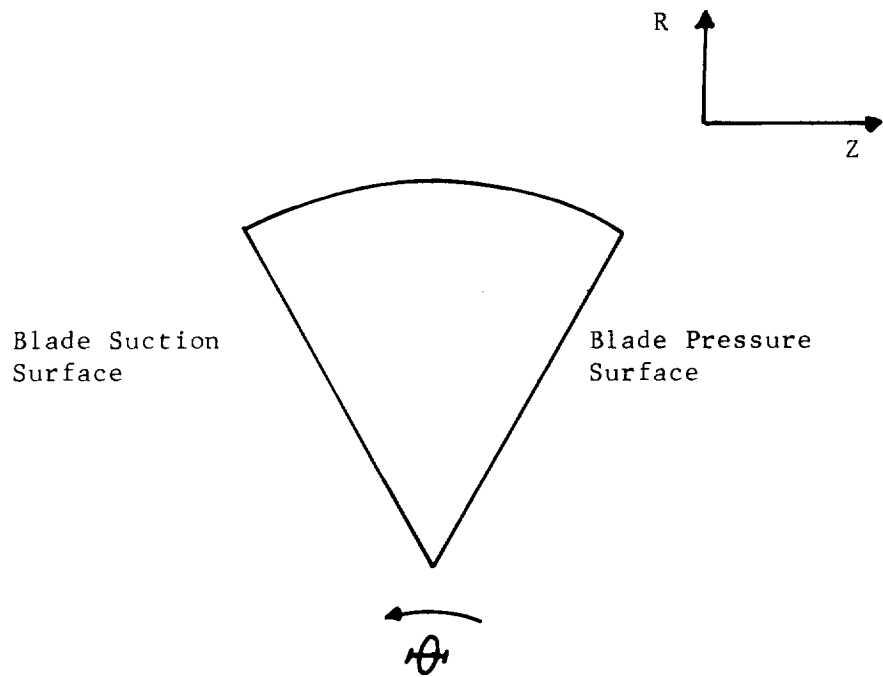
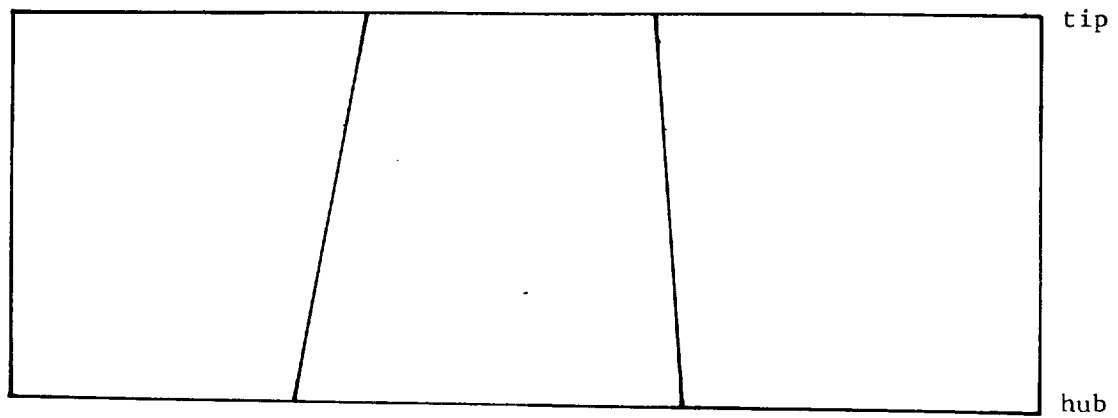
Side View of Blowdown Compressor Rotor

Figure 3.2



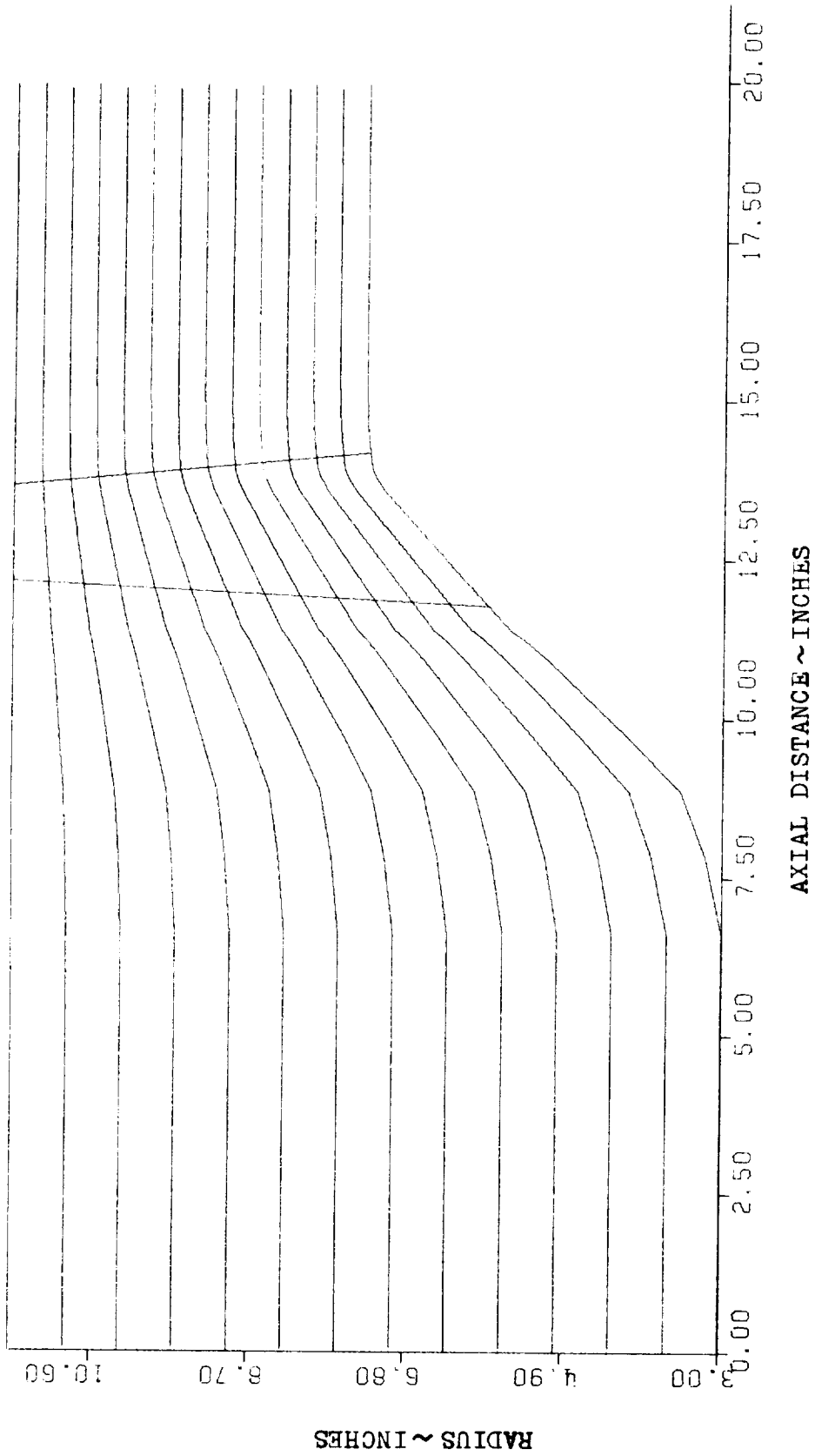
Typical Shock Pattern for a Transonic Compressor Rotor

Figure 3.1



Axial and Radial Views of
Computational Domain

Figure 3.3



Side View of Physical Domain Showing
Positions of Radial Grid Lines

Figure 3.4

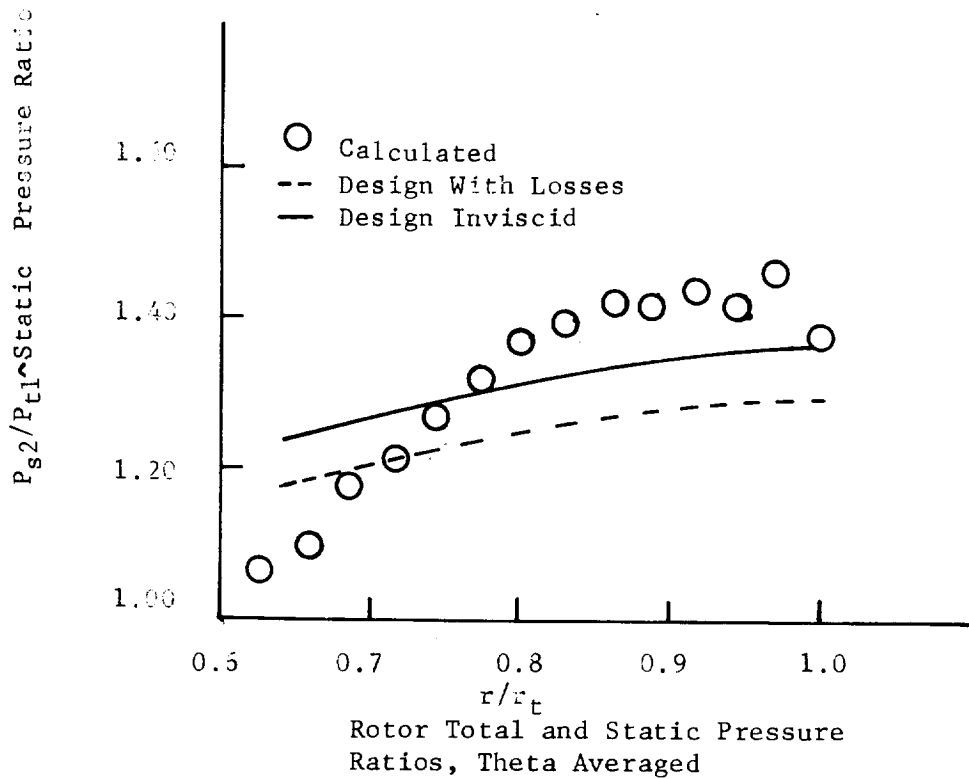
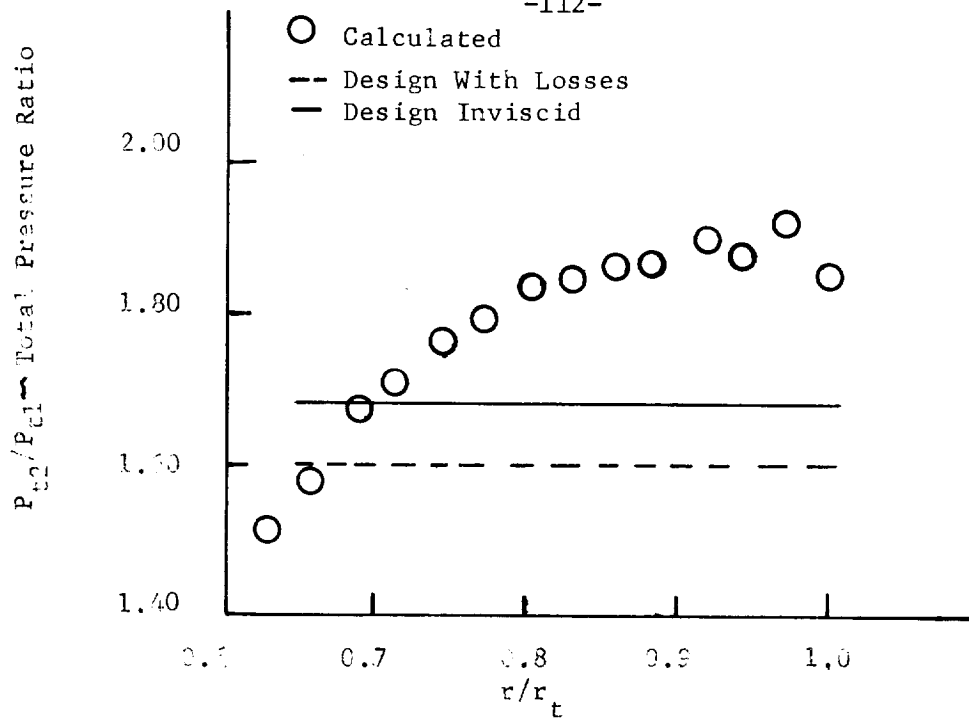


Figure 3.5

Rotor Inlet Flow Angles
Theta Average Values

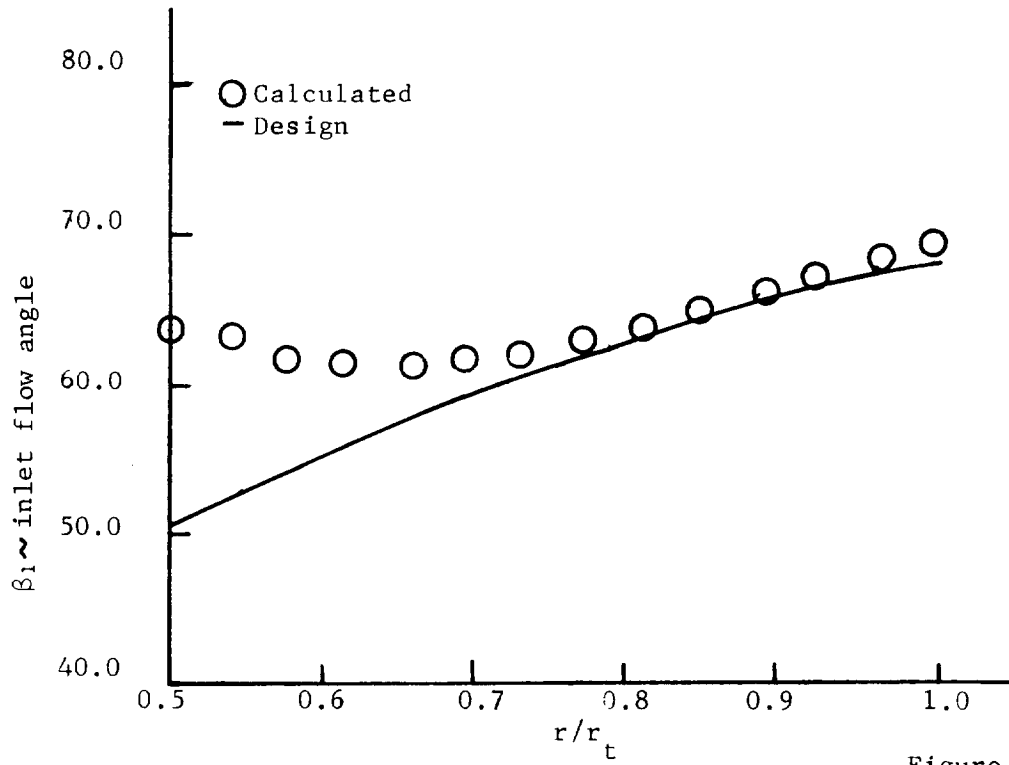
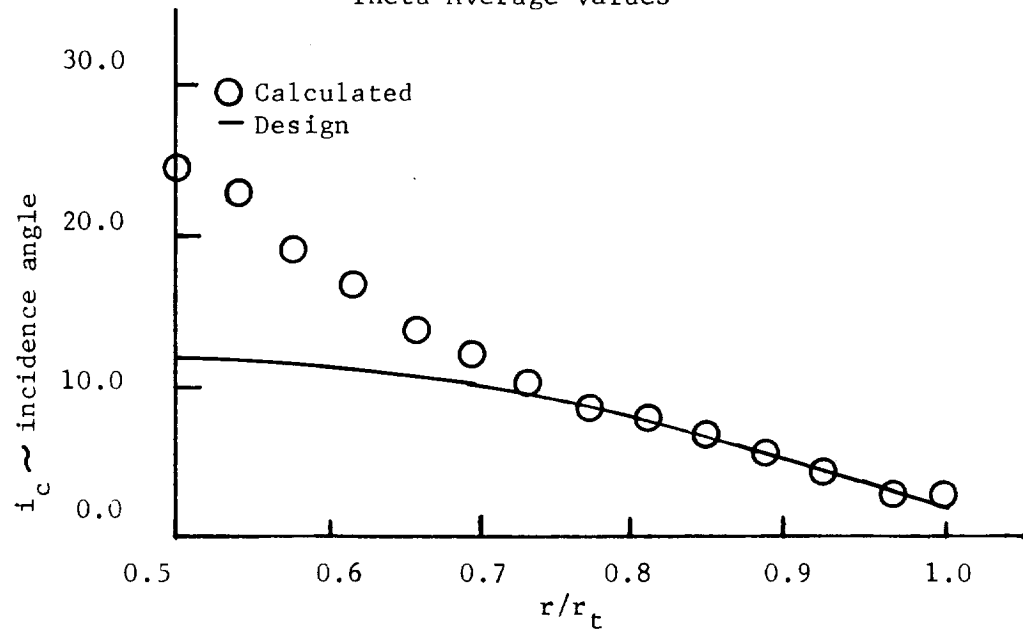


Figure 3.6

Rotor Exit Flow Angles
Relative Reference Frame
Theta Averaged Values

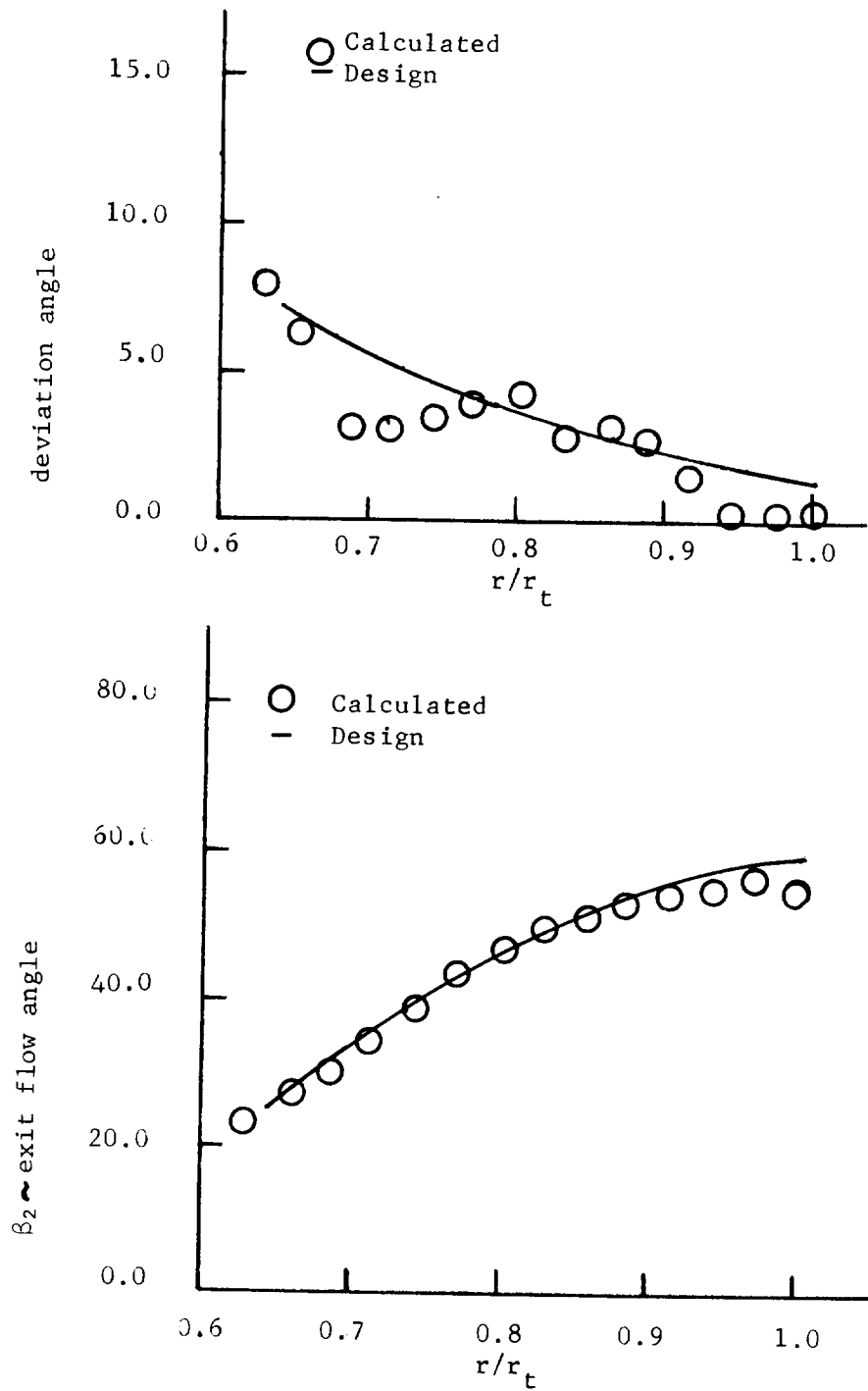


Figure 3.7

Rotor Exit Axial and Pitchwise
Mach Number Profiles
Theta Averaged Values

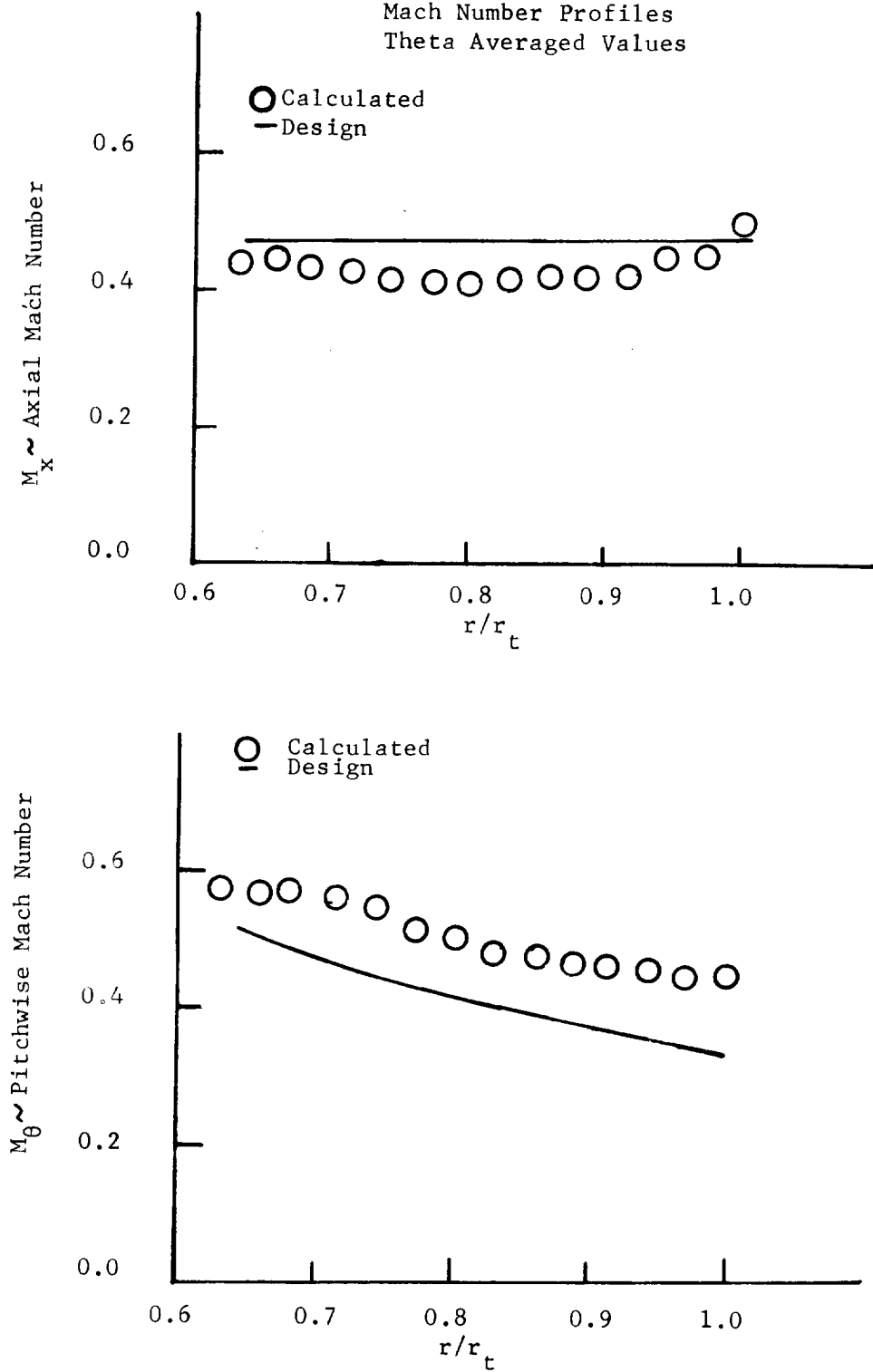


Figure 3.8

Mach Number Contours for Computational
Blade to Blade Surface
Radius Ratio = 1.0

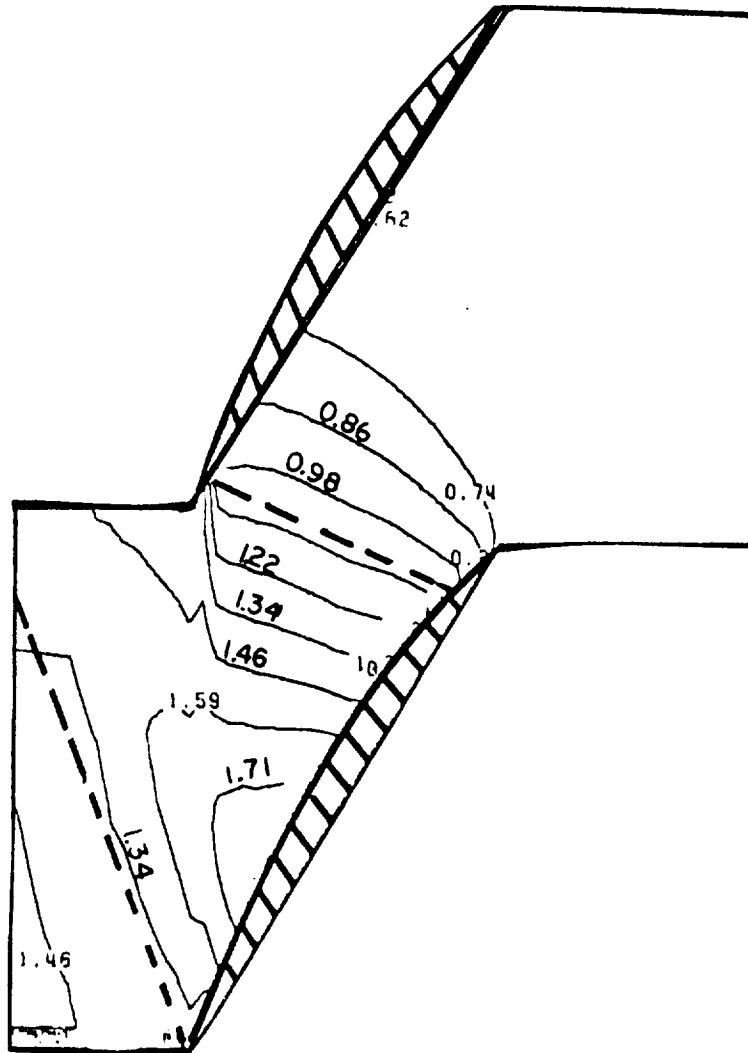


Figure 3.9

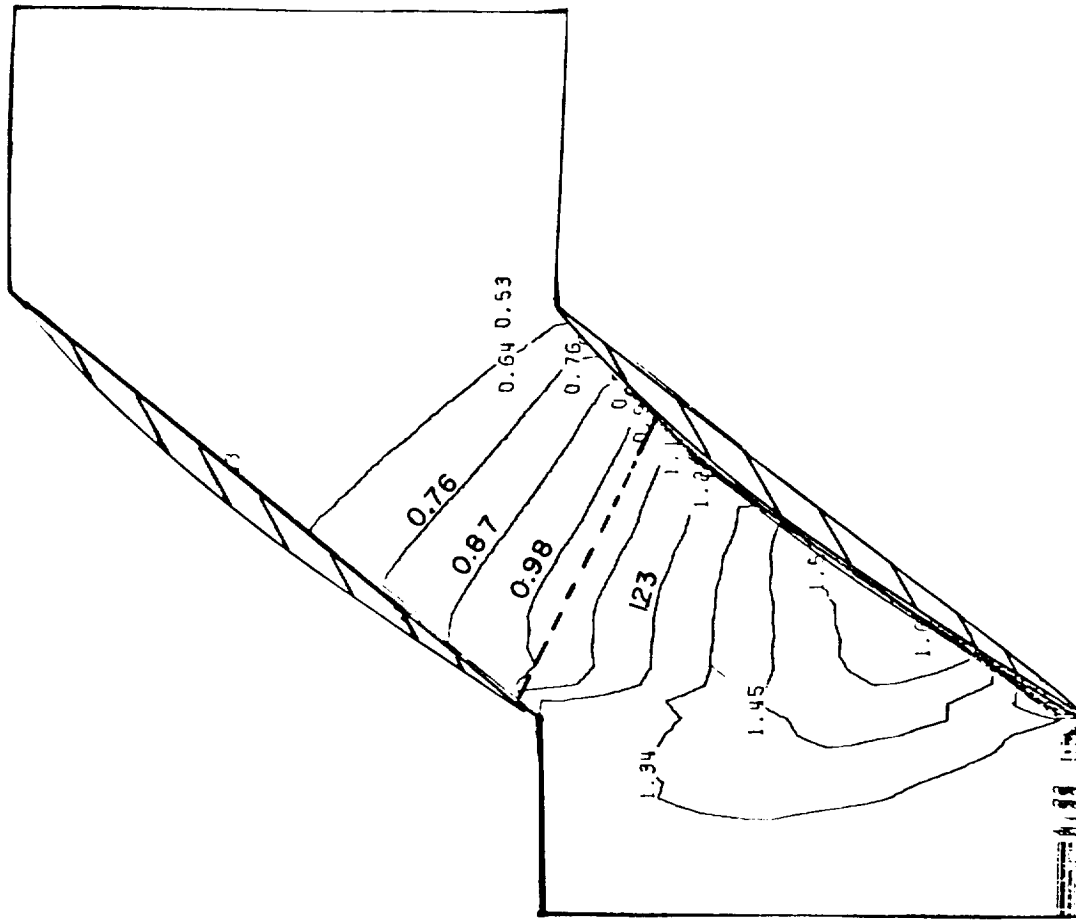


Figure 3.10

Mach Number Contours for Computational
Blade to Blade Surface Radius Ratio= 0.75

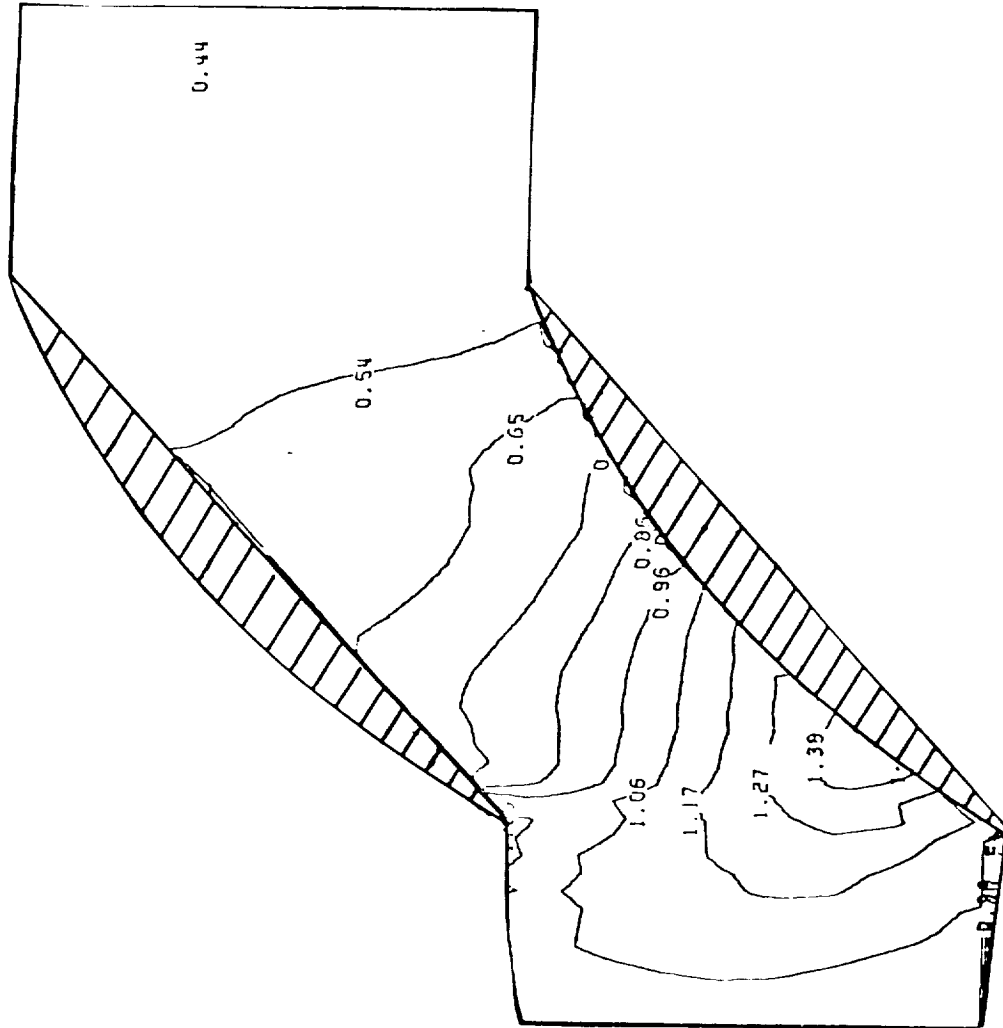
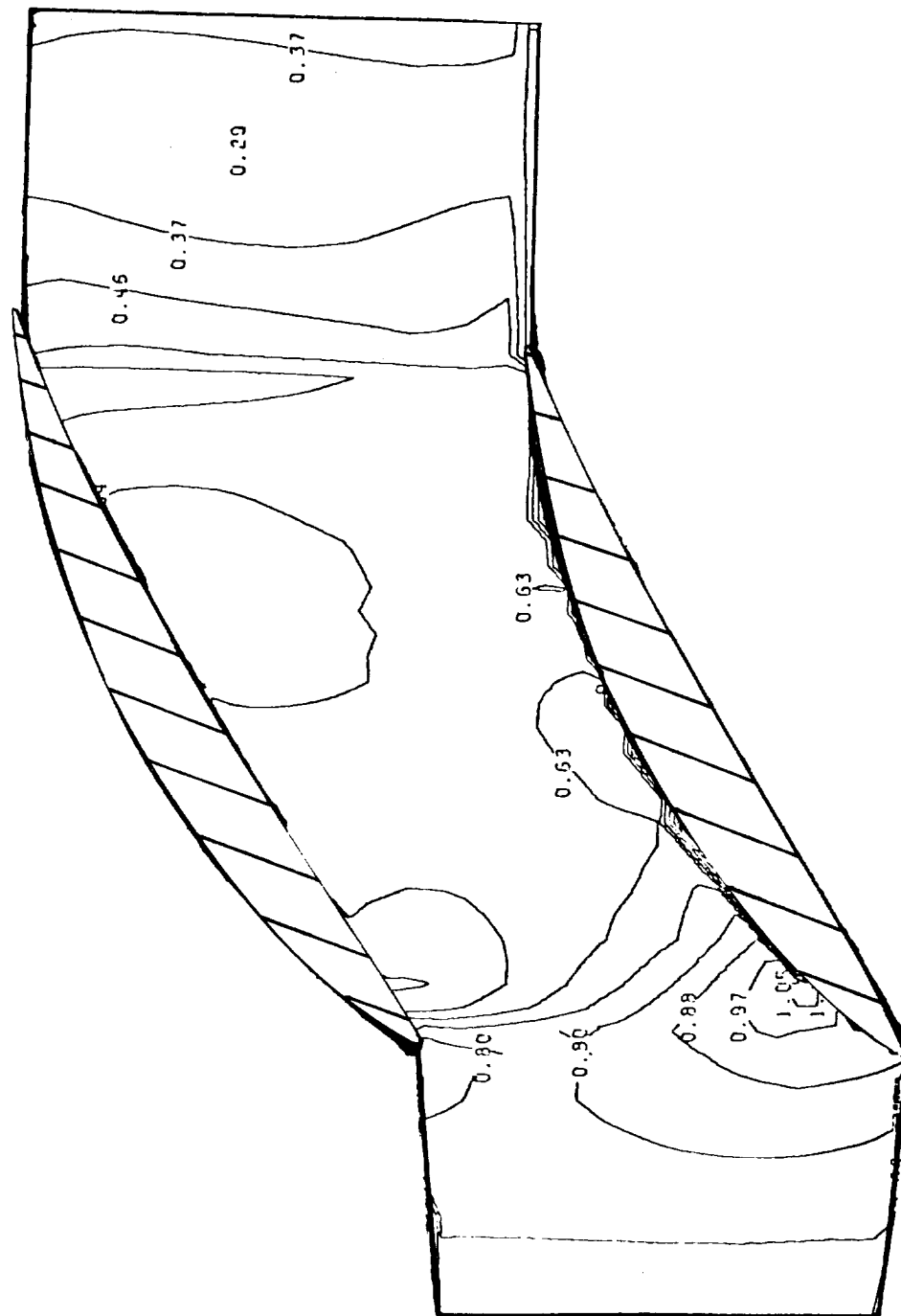
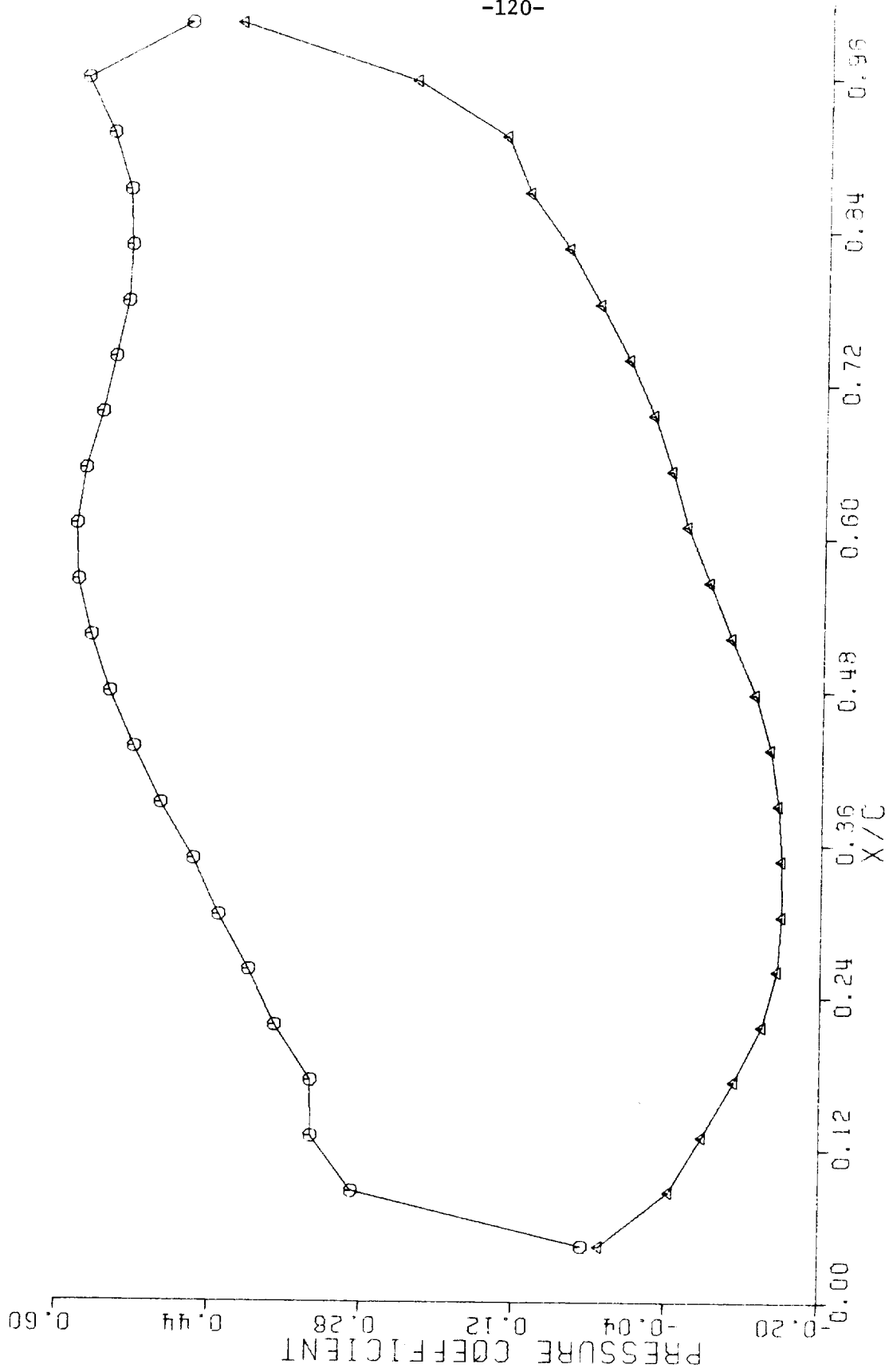


Figure 3.11

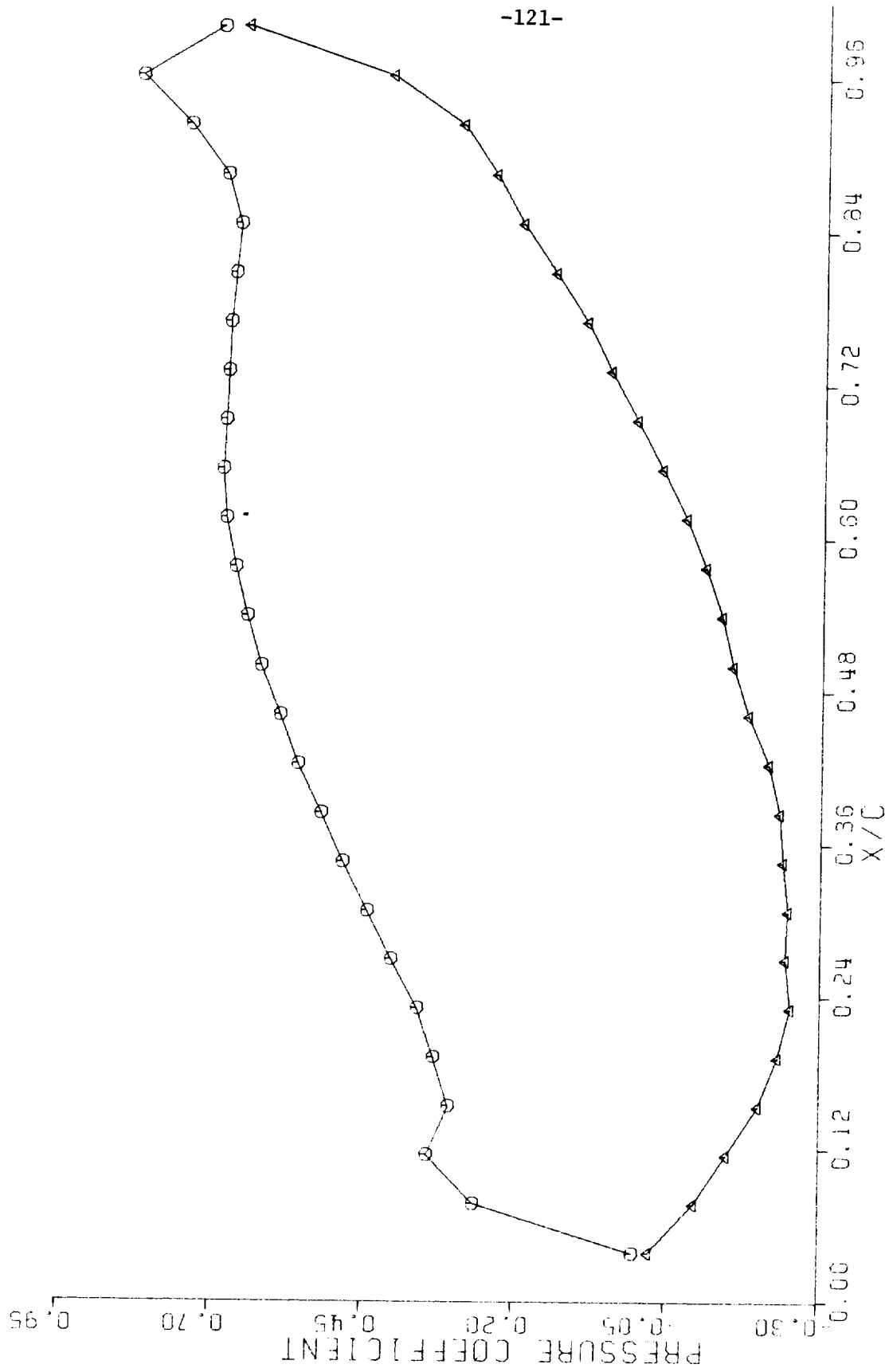
MACH NUMBER CONTOURS FOR COMPUTATIONAL
BLADE TO BLADE SURFACE NUMBER 2
HUB SURFACE





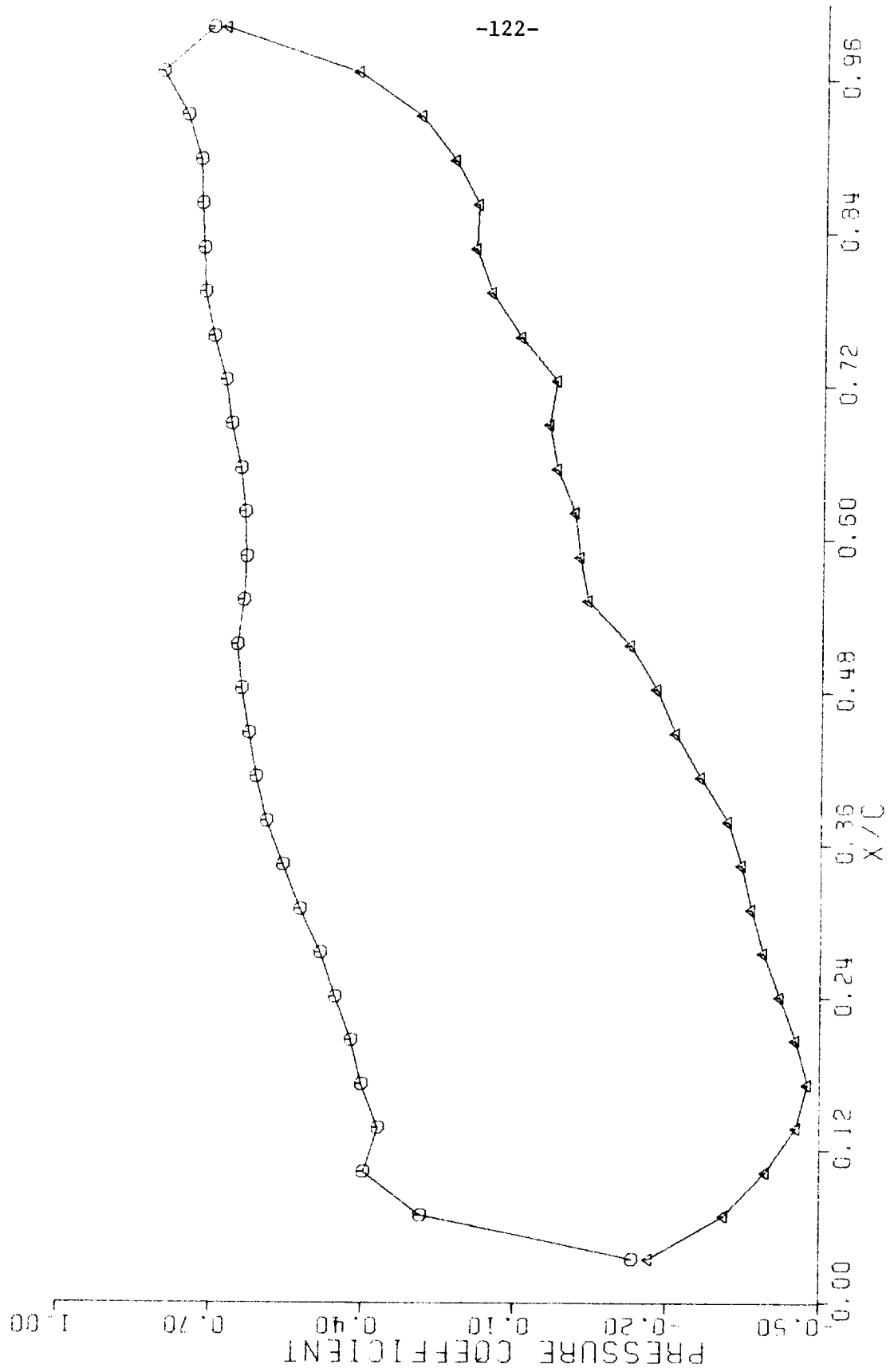
Pressure Coefficient Along Computational
Blade to Blade Surface Tip Radius

Figure 3.13



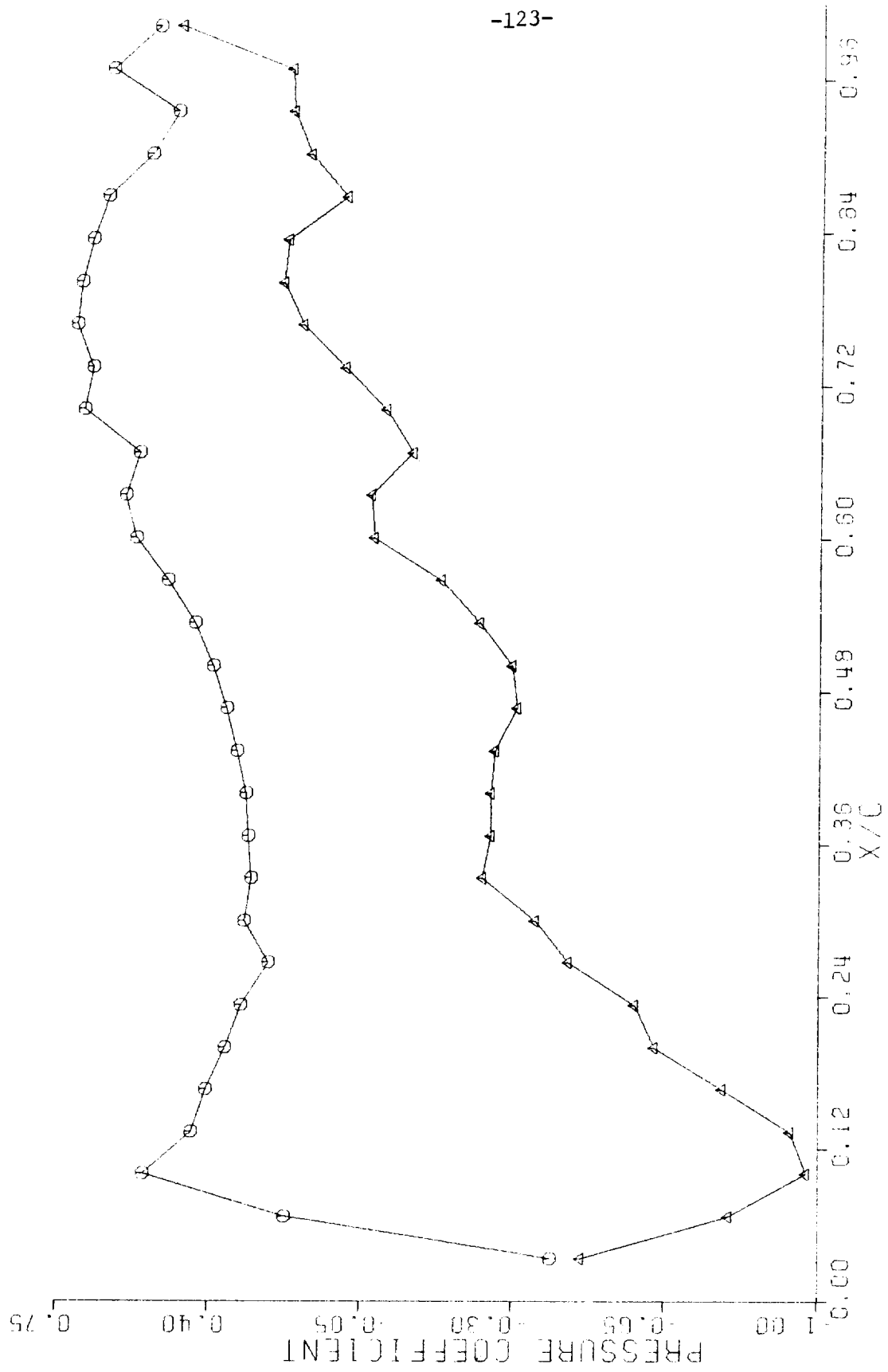
Pressure Coefficient Along Computational
Blade to Blade Surface Radius Ratio 0.86

Figure 3.14



Pressure Coefficient Along Computational
Blade to Blade Surface Radius Ratio 0.75

Figure 3.15



Pressure Coefficient Along Computational
Blade to Blade Surface Hub Radius

Figure 3.16

Computed Blade to Blade Stream Surfaces

View as Seen Looking Downstream

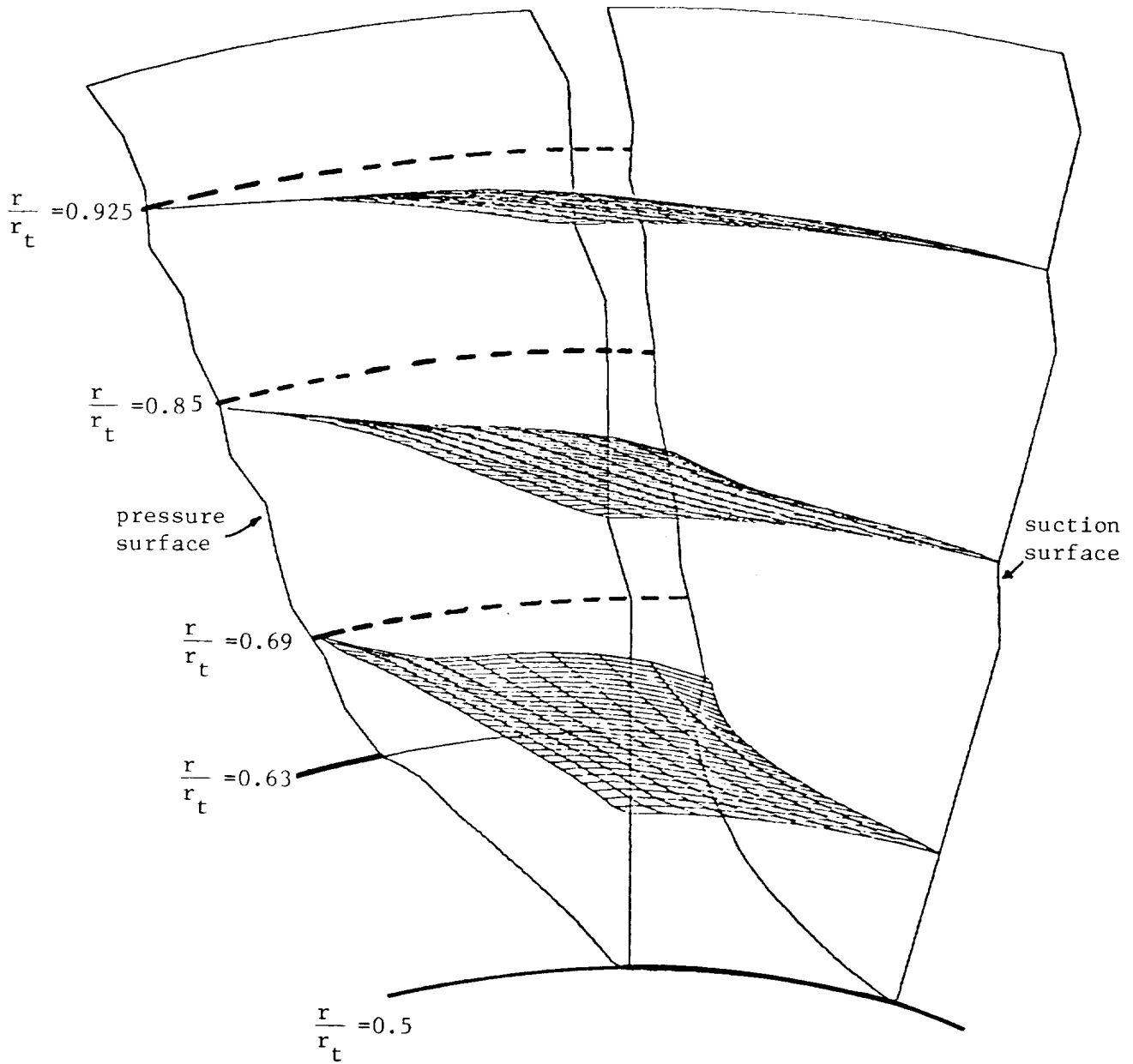


Figure 3.17

Computed S2 Surfaces

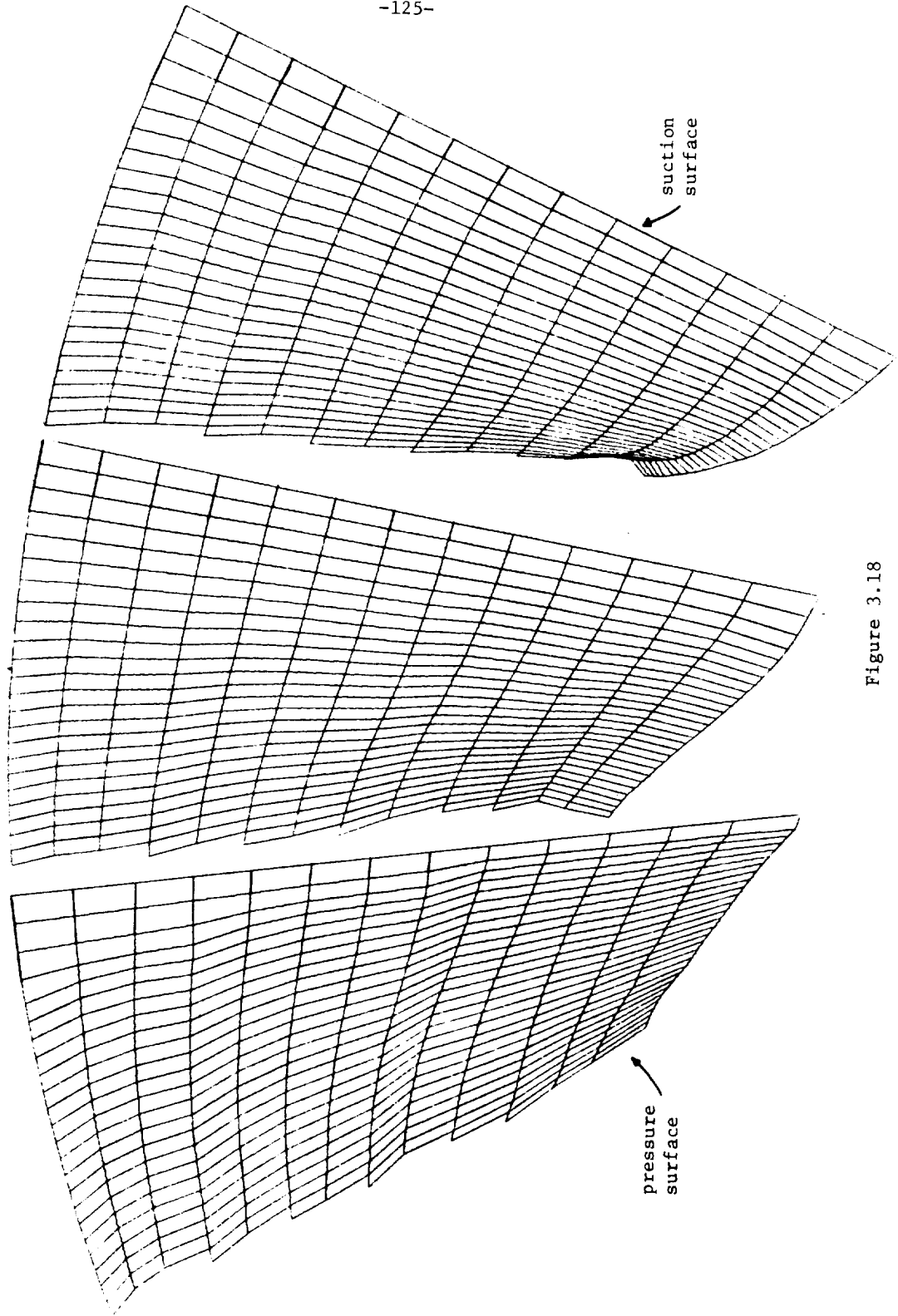


Figure 3.18

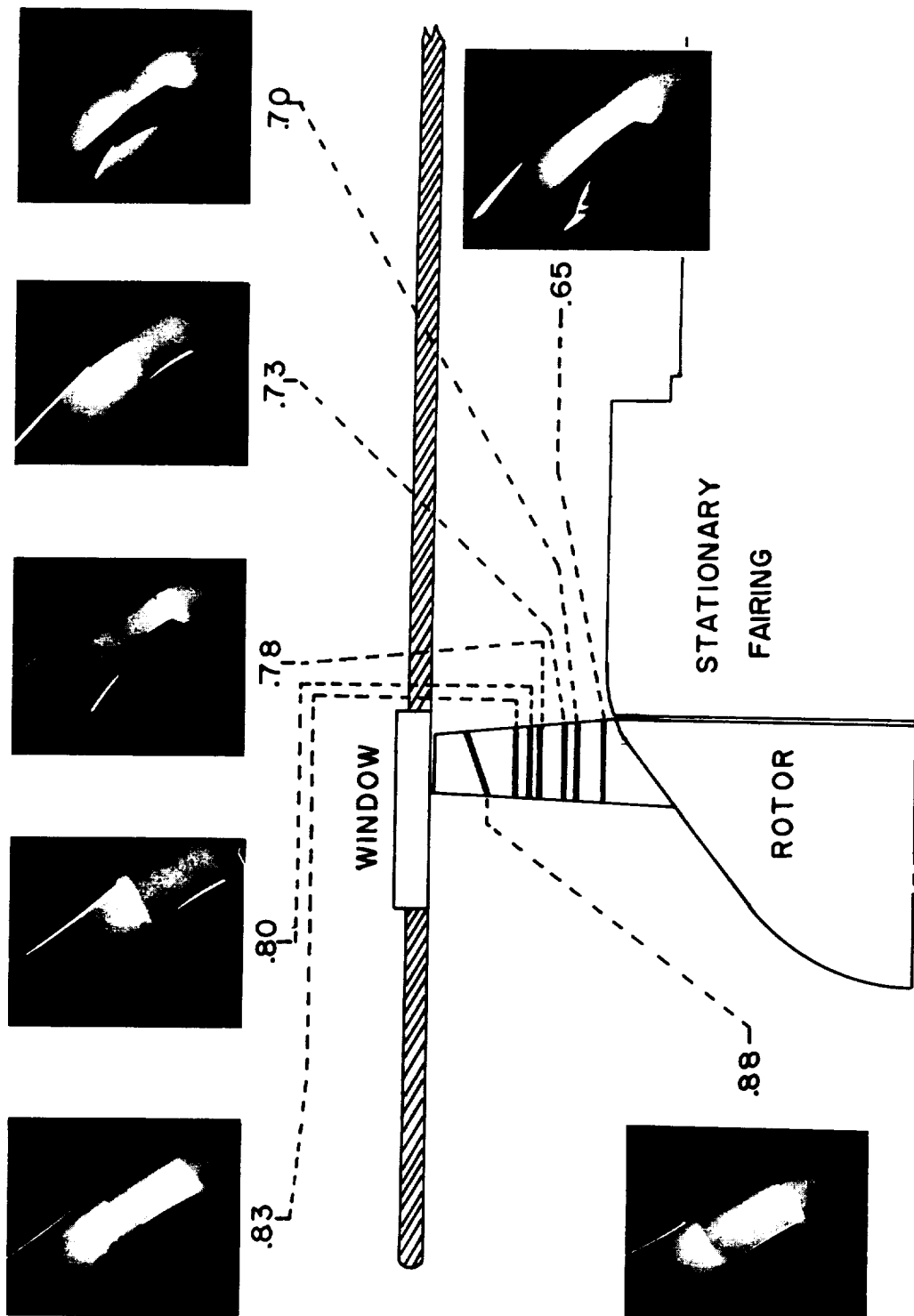
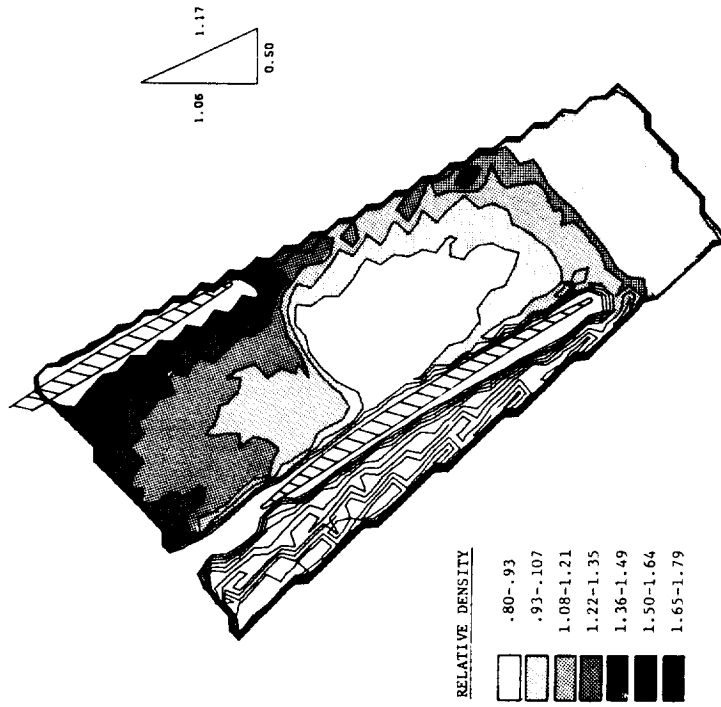


FIGURE 4.1

Positions of visualization planes in the transonic rotor.
All images are at design speed, $M_t=1.2$.



UNPROCESSED



FULLY CORRECTED

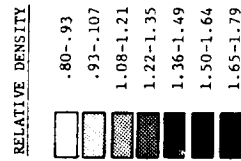


FIGURE 4.2
VISUALIZED FLOW AT $r/r_t = 0.88$

Computed Density Contour Map
Radius Ratio = 0.88

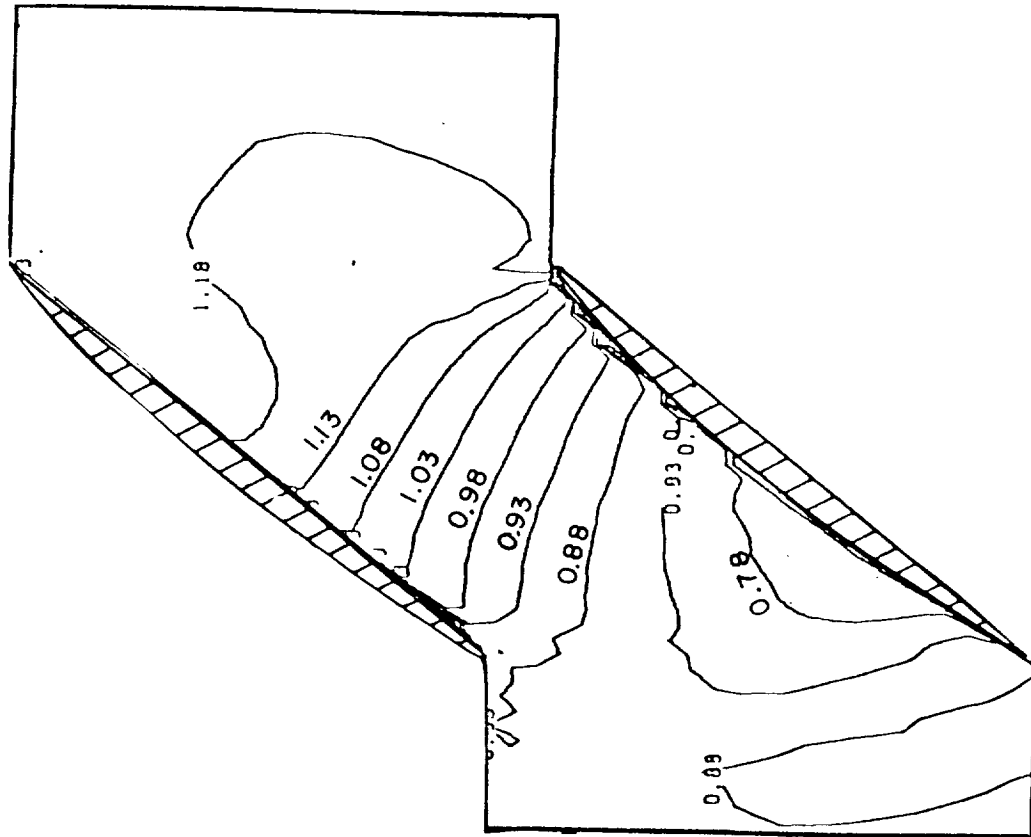


Figure 4.3

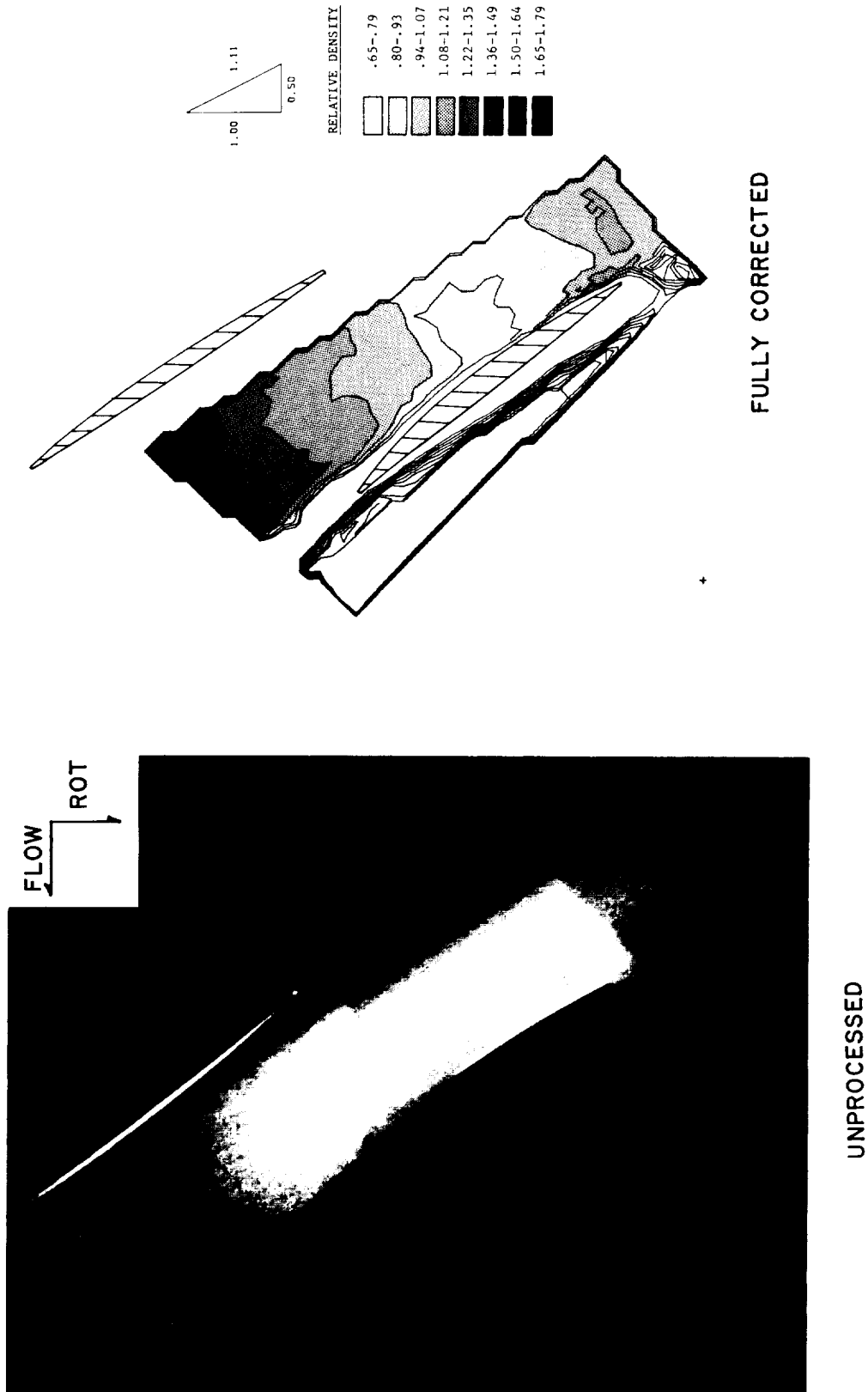


FIGURE 4.4
VISUALIZED FLOW AT $r/r_t = 0.83$

Computed Density Contour Map
Radius Ratio = 0.83

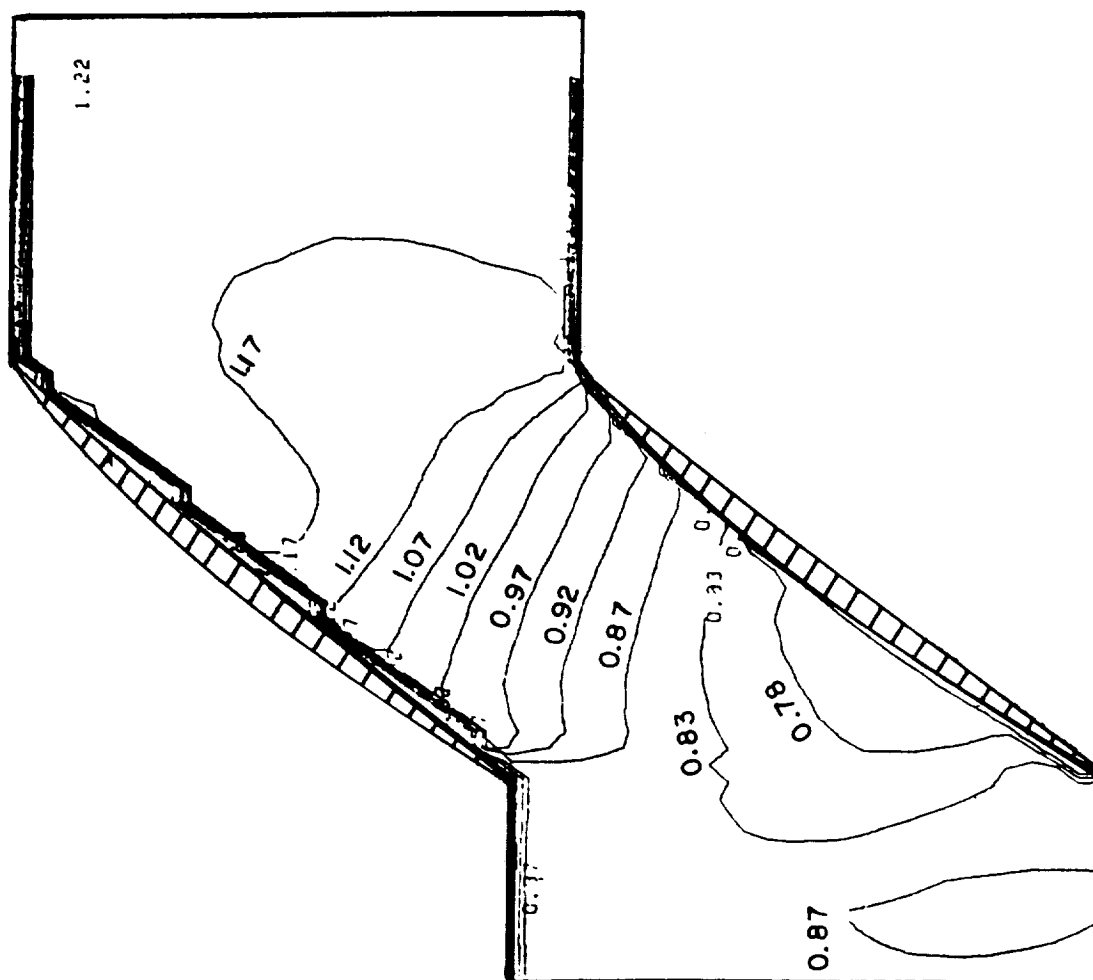


Figure 4.5

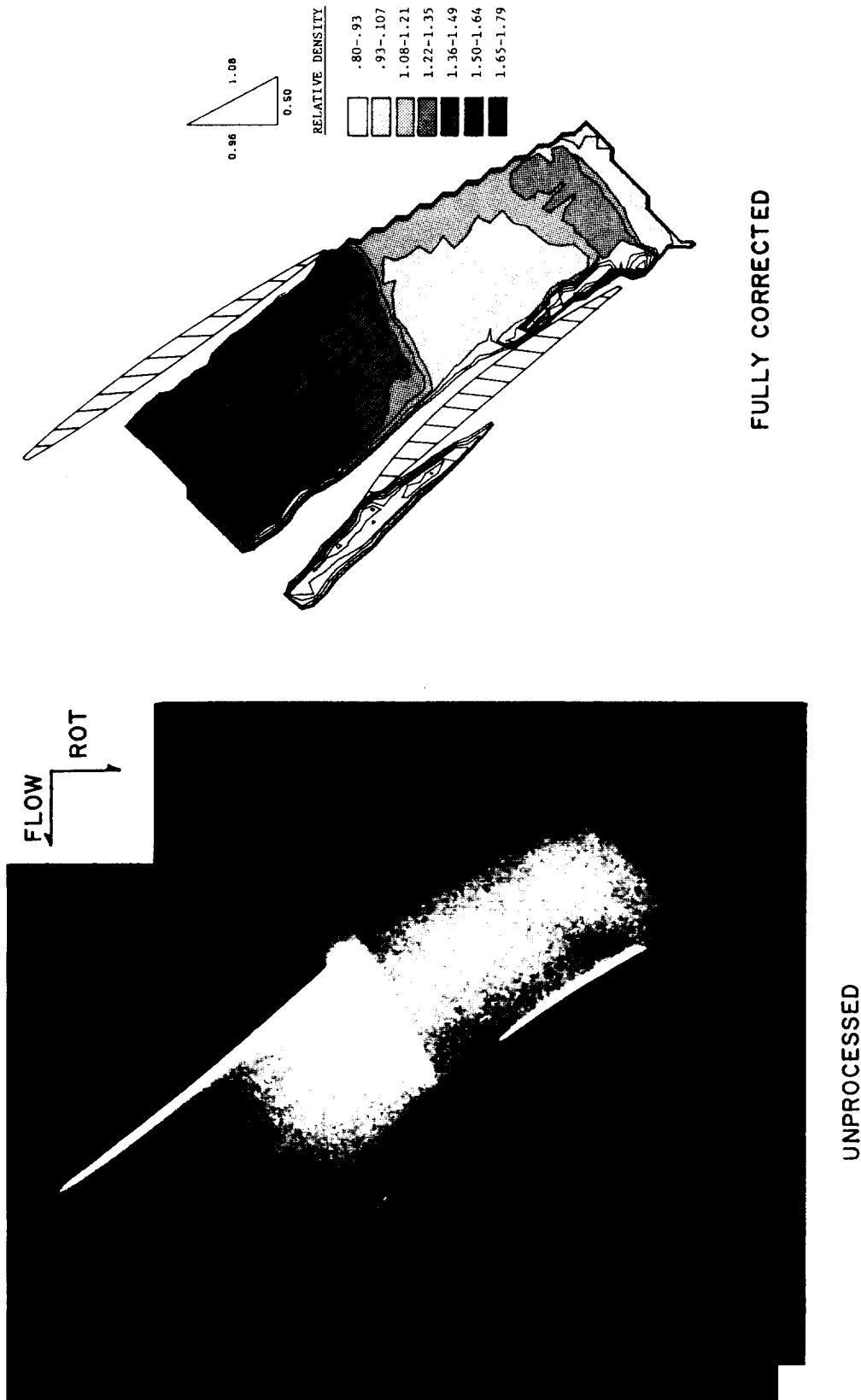


FIGURE 4.6
VISUALIZED FLOW AT $r/r_t = 0.80$

Computed Density Contour Map
Radius Ratio = 0.80

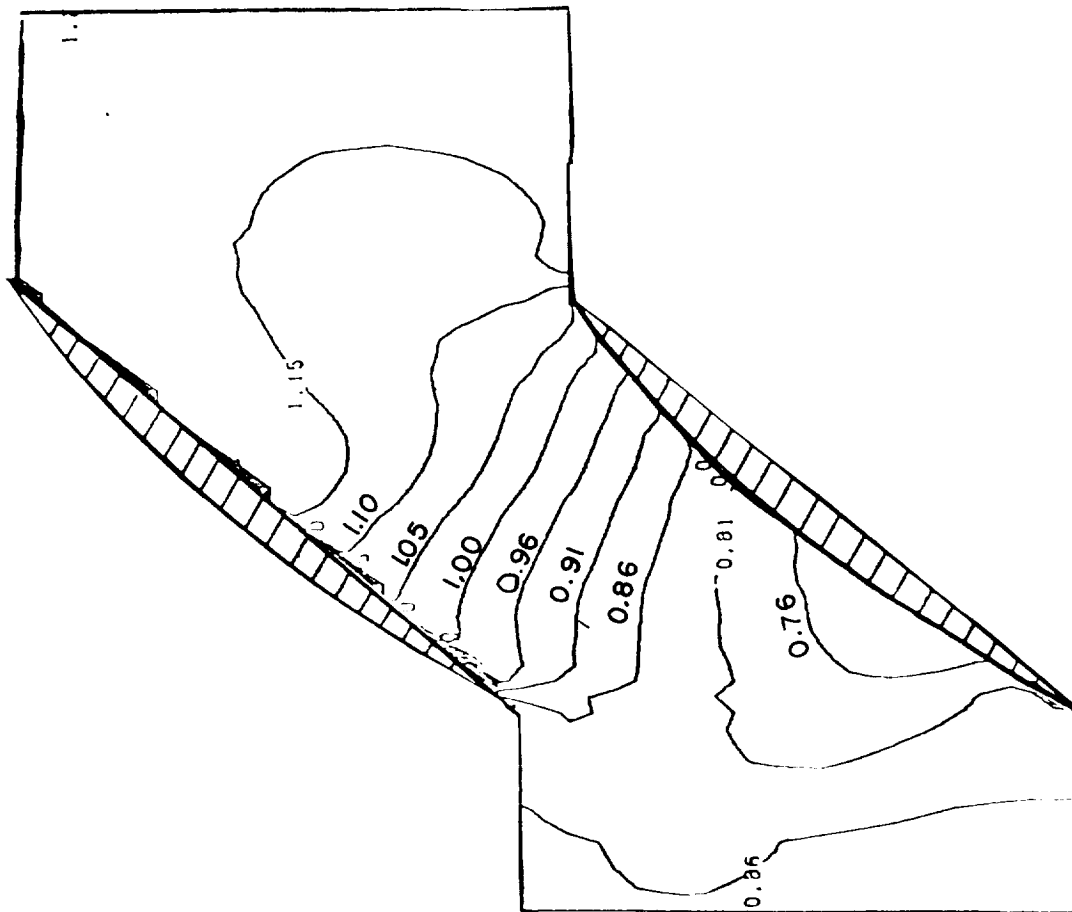
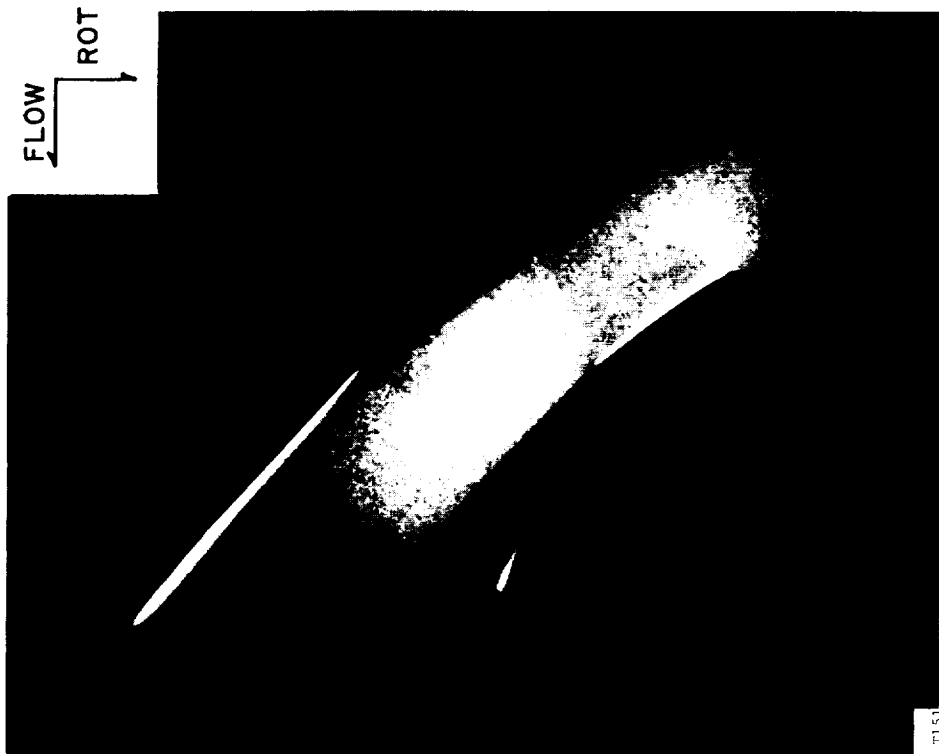


Figure 4.7



UNPROCESSED

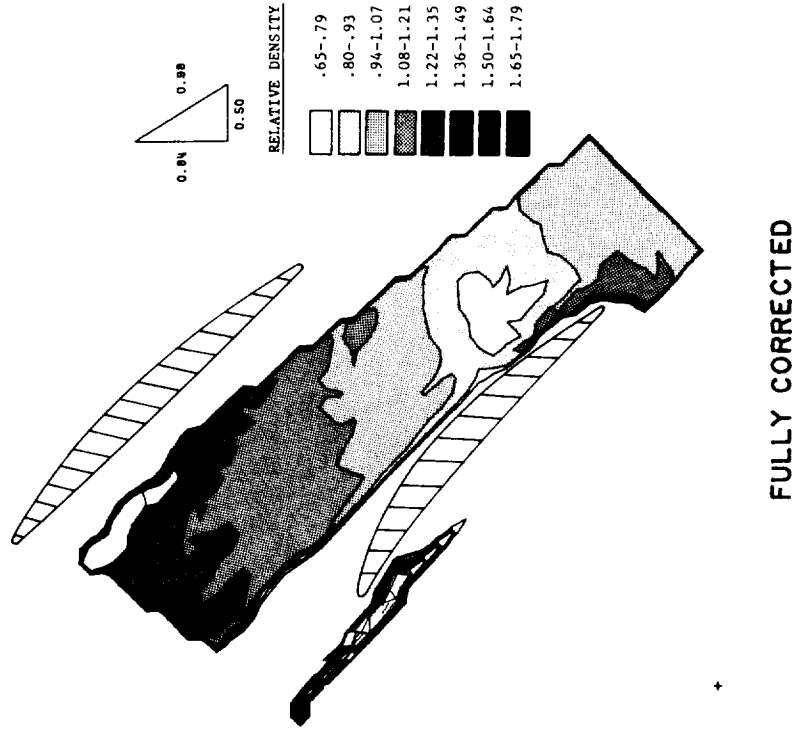


FIGURE 4.8
VISUALIZED FLOW AT $r/r_t = 0.70$

Computed Density Contour Map
Radius Ratio = 0.70

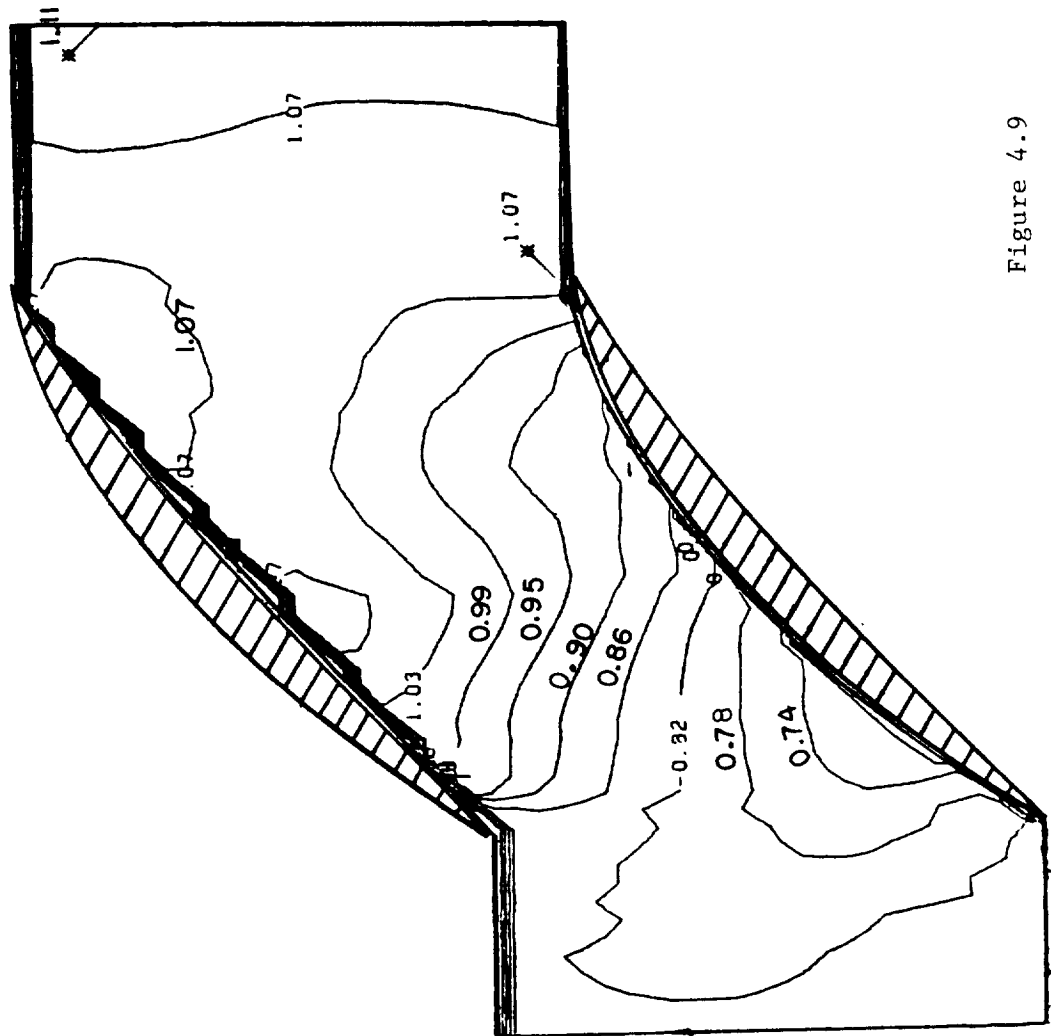
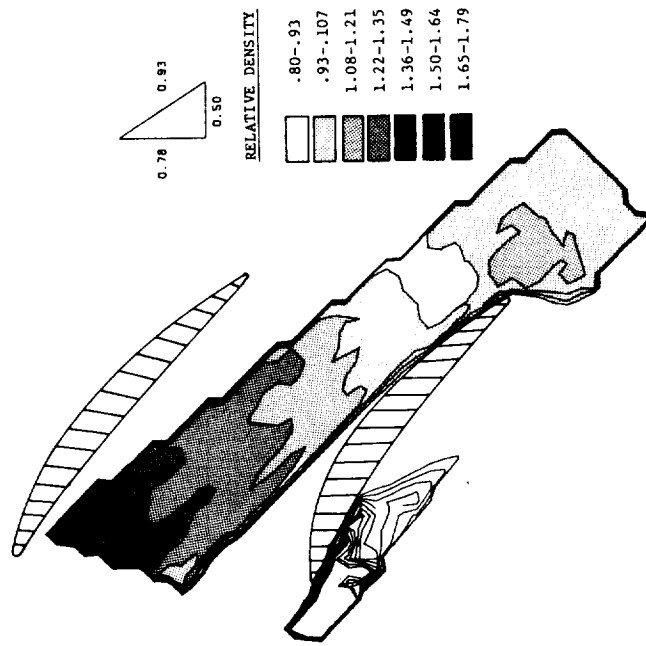


Figure 4.9



UNPROCESSED



FULLY CORRECTED

FIGURE 4.10
VISUALIZED FLOW AT $r/r_t = 0.65$

Computed Density Contour Map
Radius Ratio = 0.65

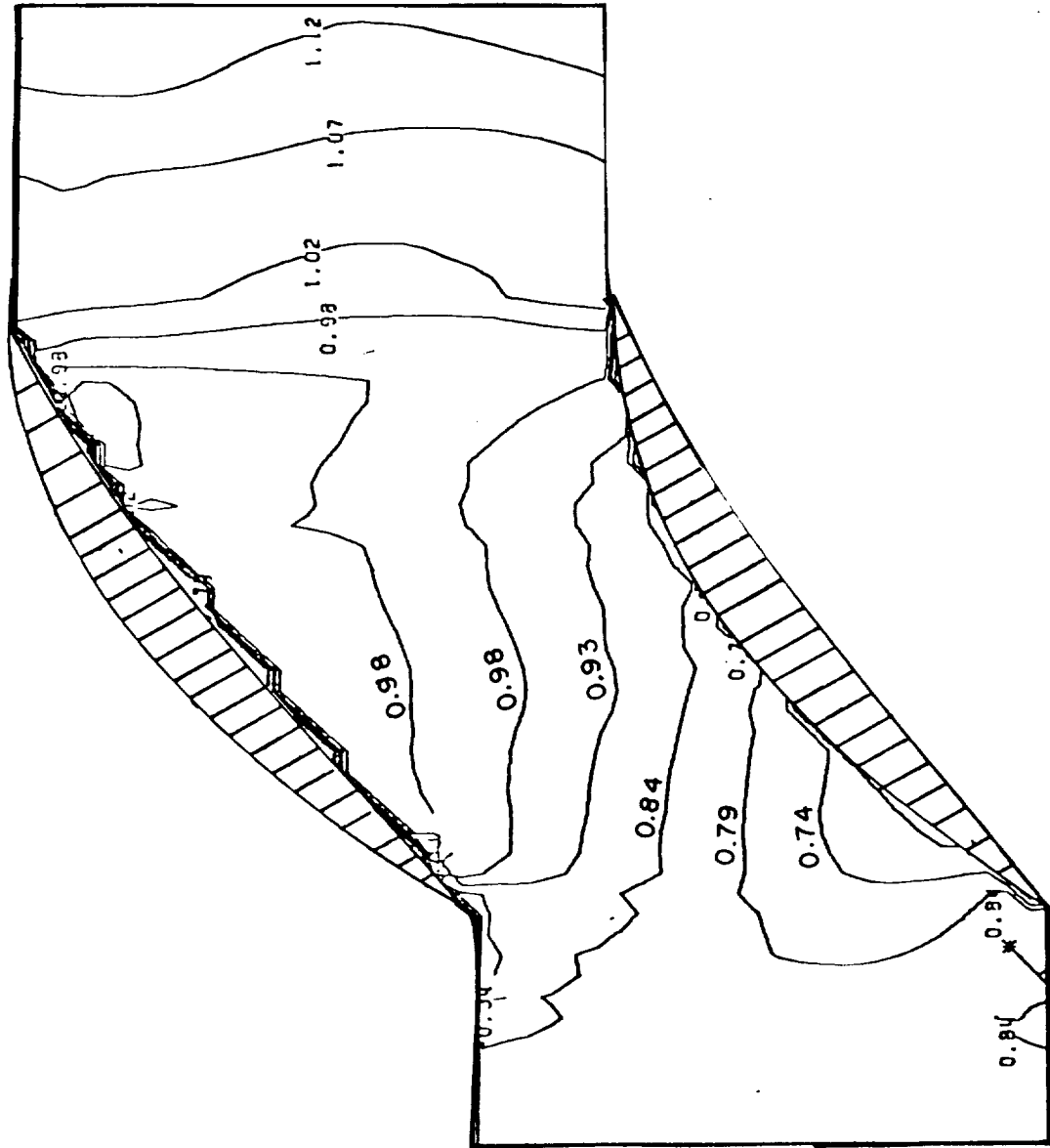
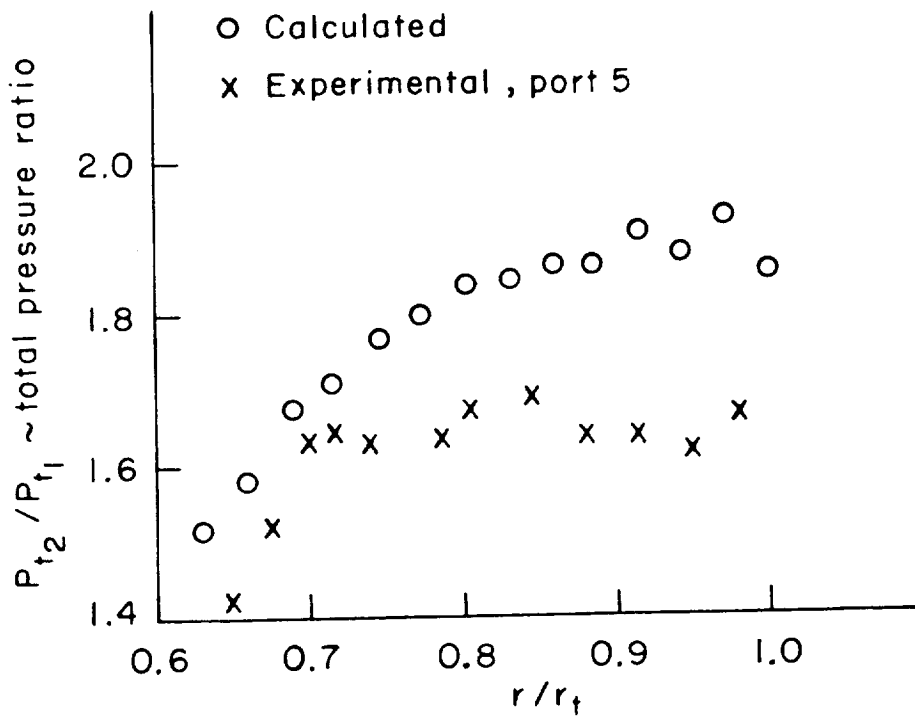
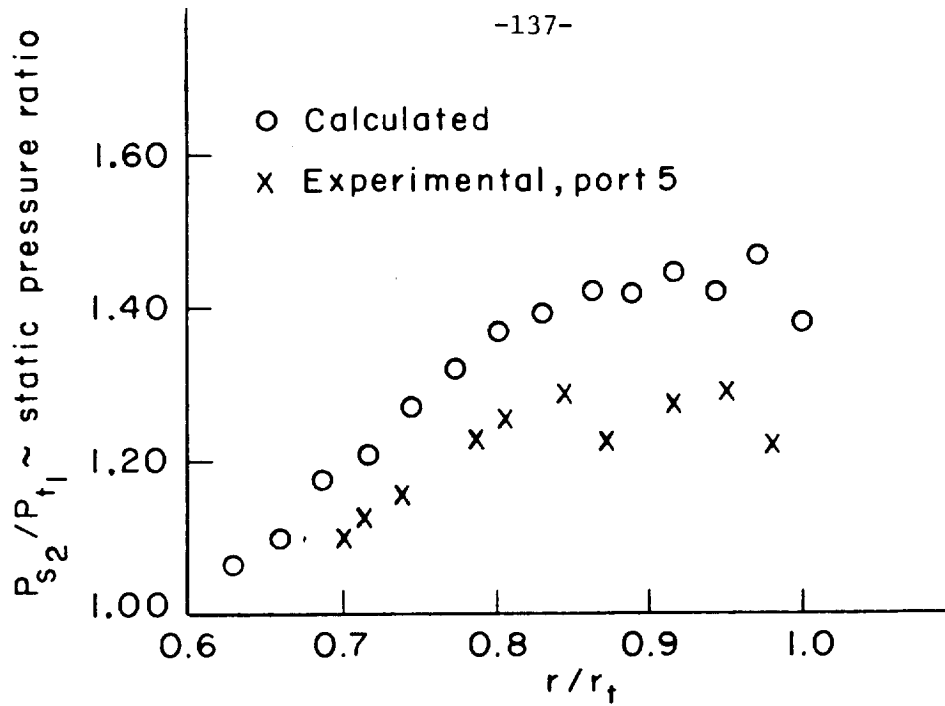
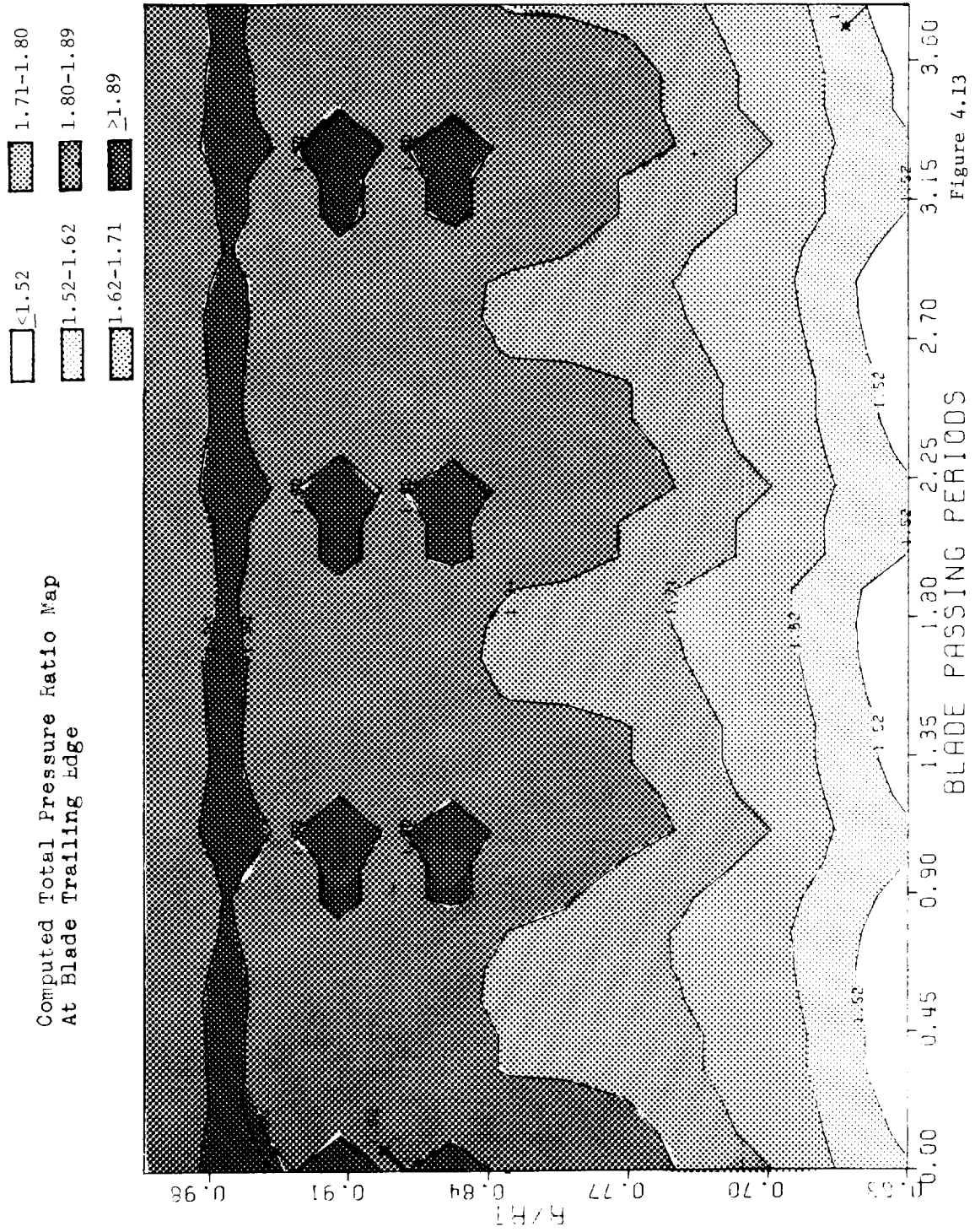


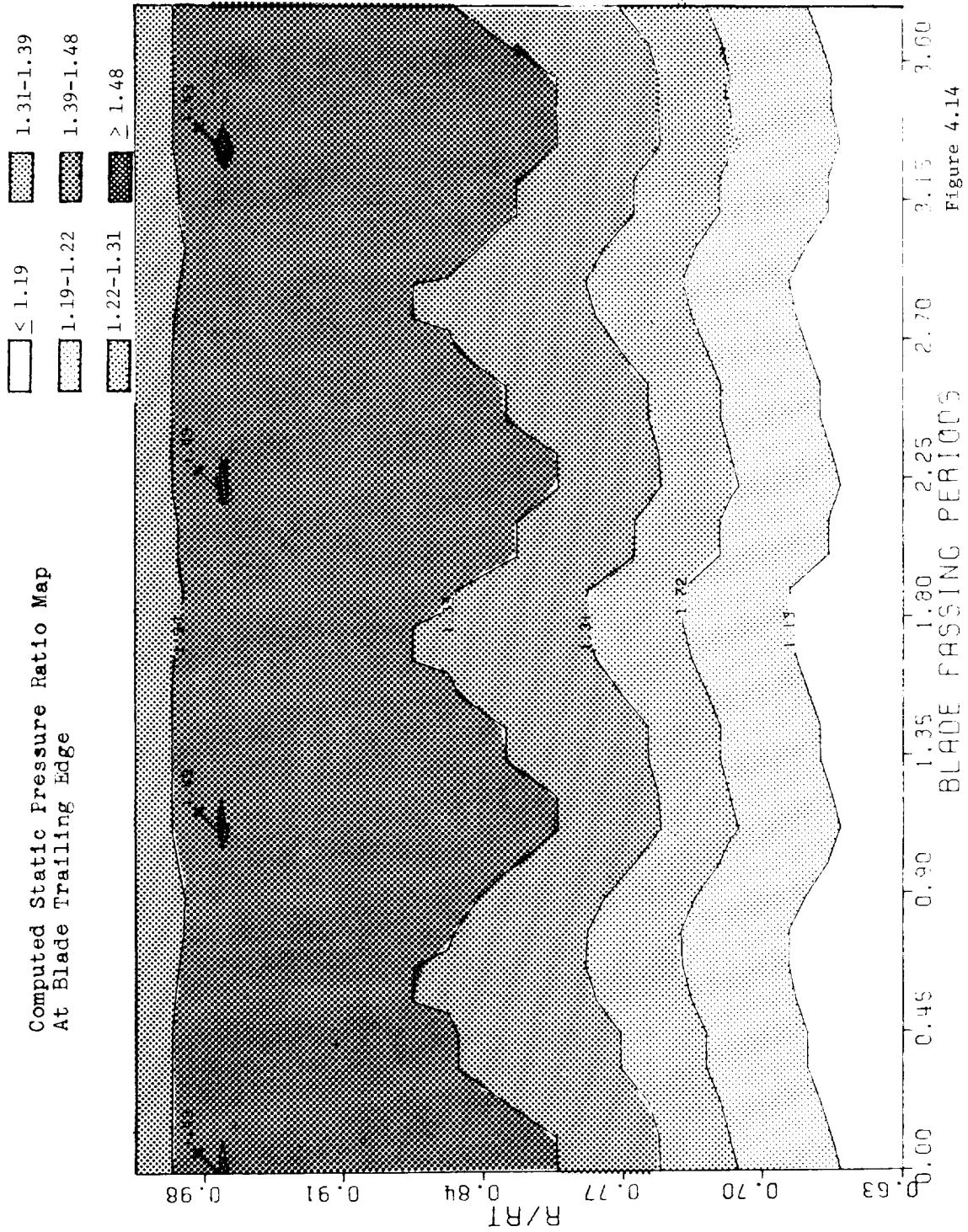
Figure 4.11

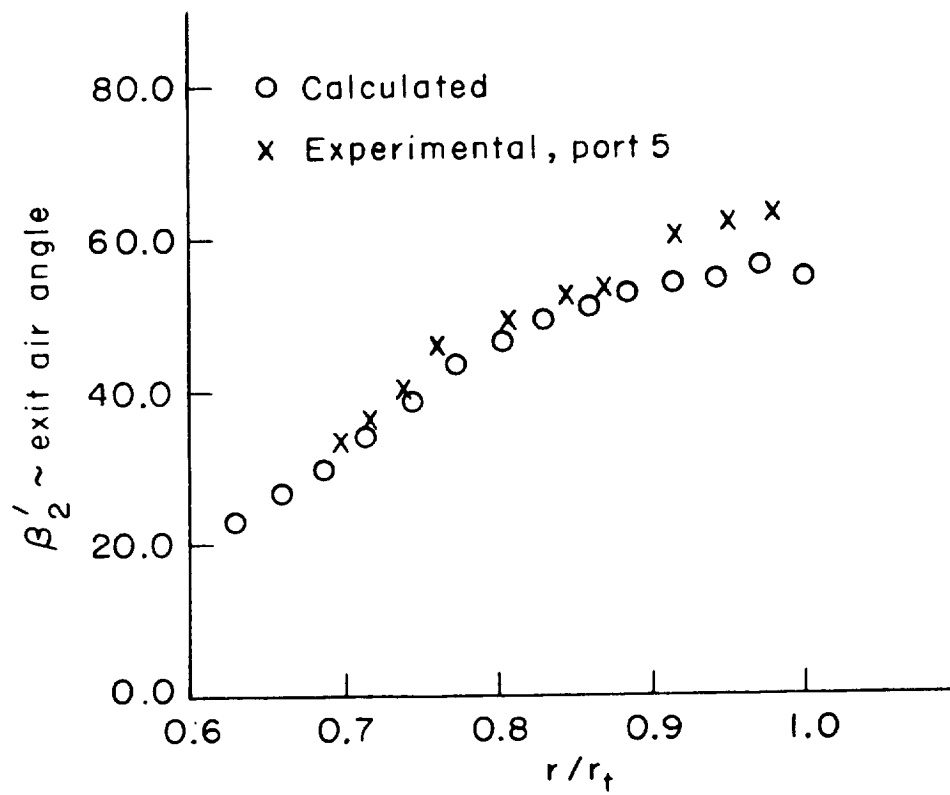


Rotor Total and Static Pressure Ratios
Theta Averaged Values

Figure 4.12







Rotor Exit Air Angles Relative Coordinate
Frame Theta Averaged Values

Figure 4.15

Computed velocity Components
Radius Ratio = 0.75
At Blade Trailing Edge

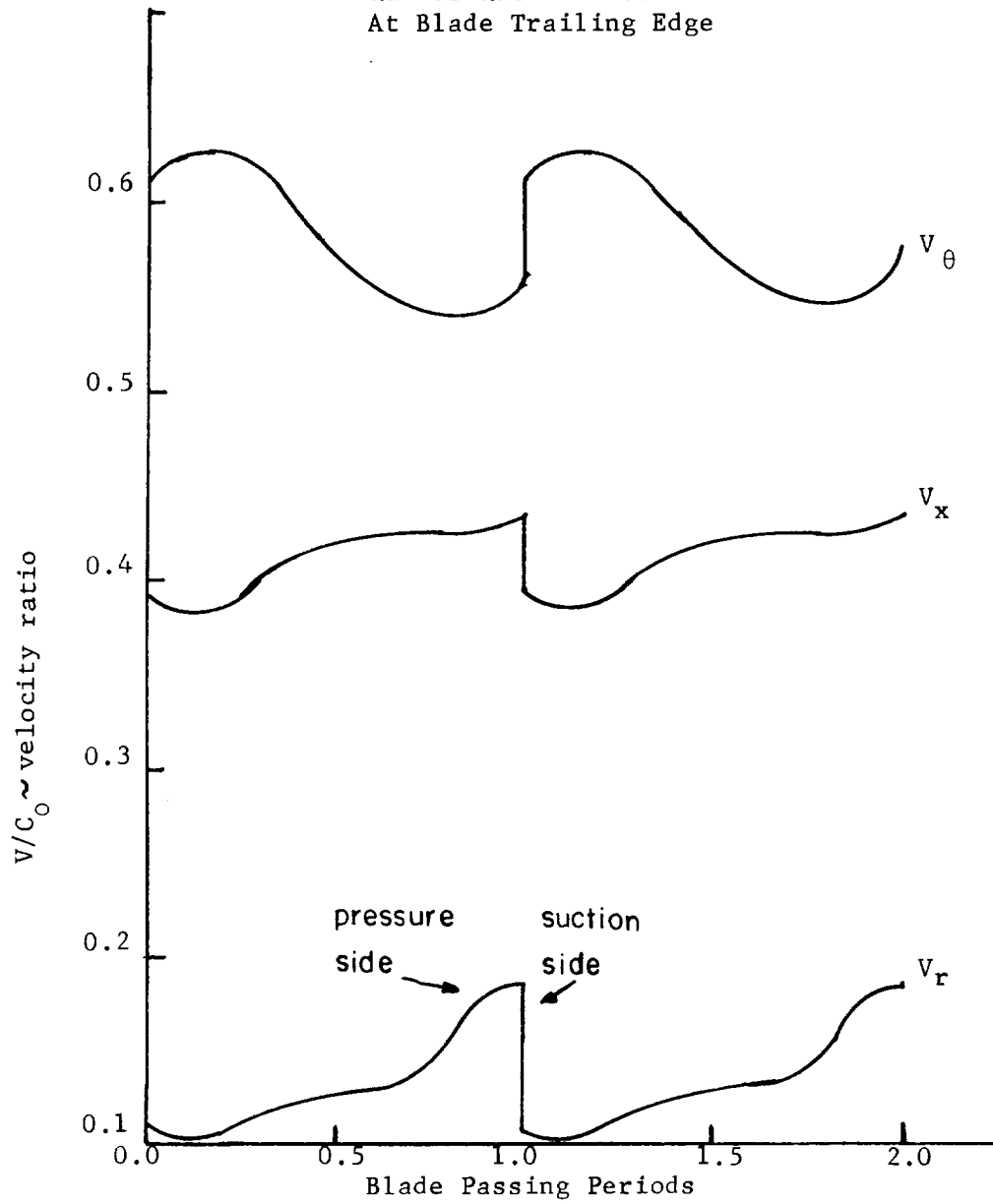


Figure 4.16

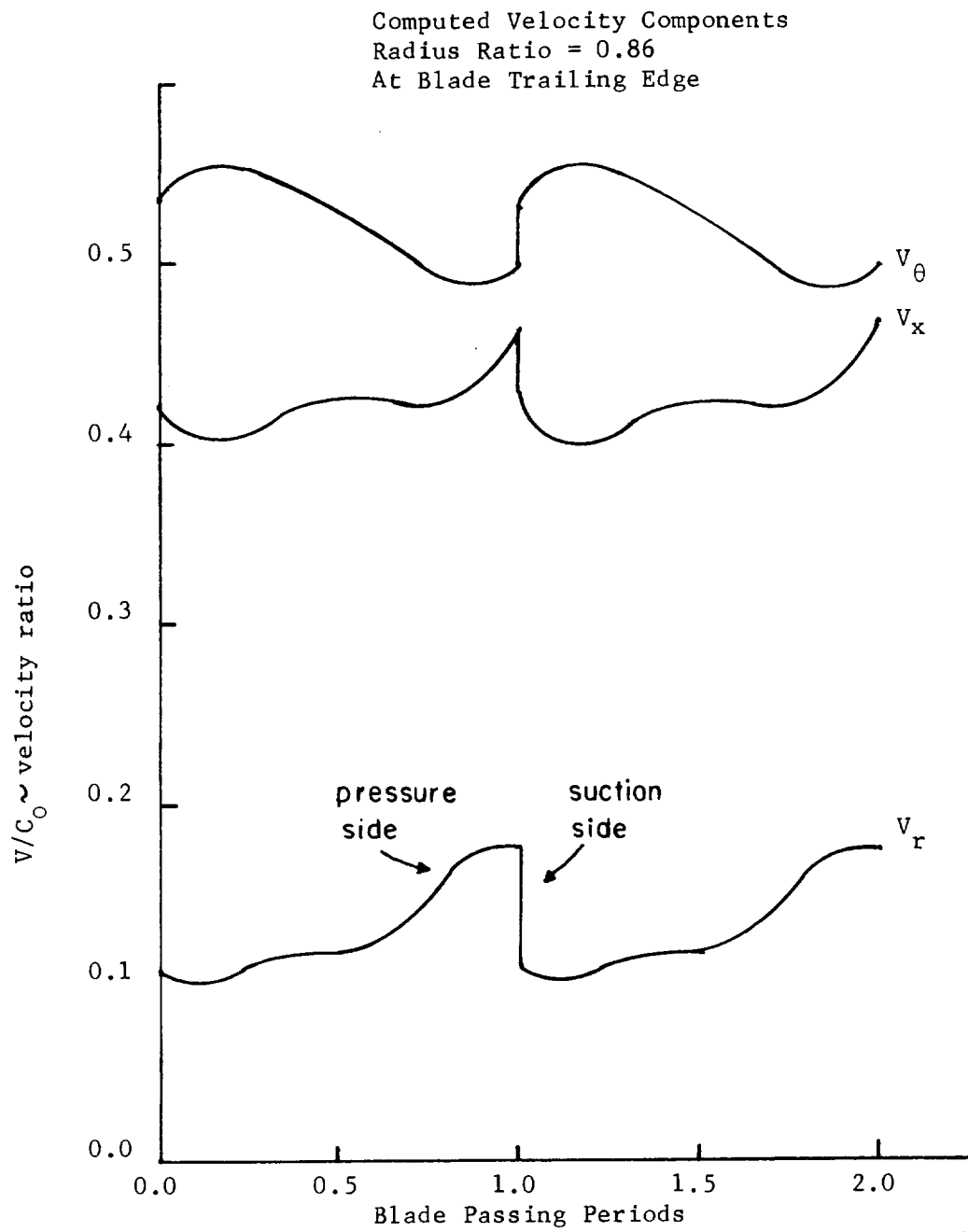


Figure 4.17

MACH NUMBER COMPONENTS
R/RT = 0.345
0.1 AXIAL CHORDS DOWNSTREAM OF ROTOR

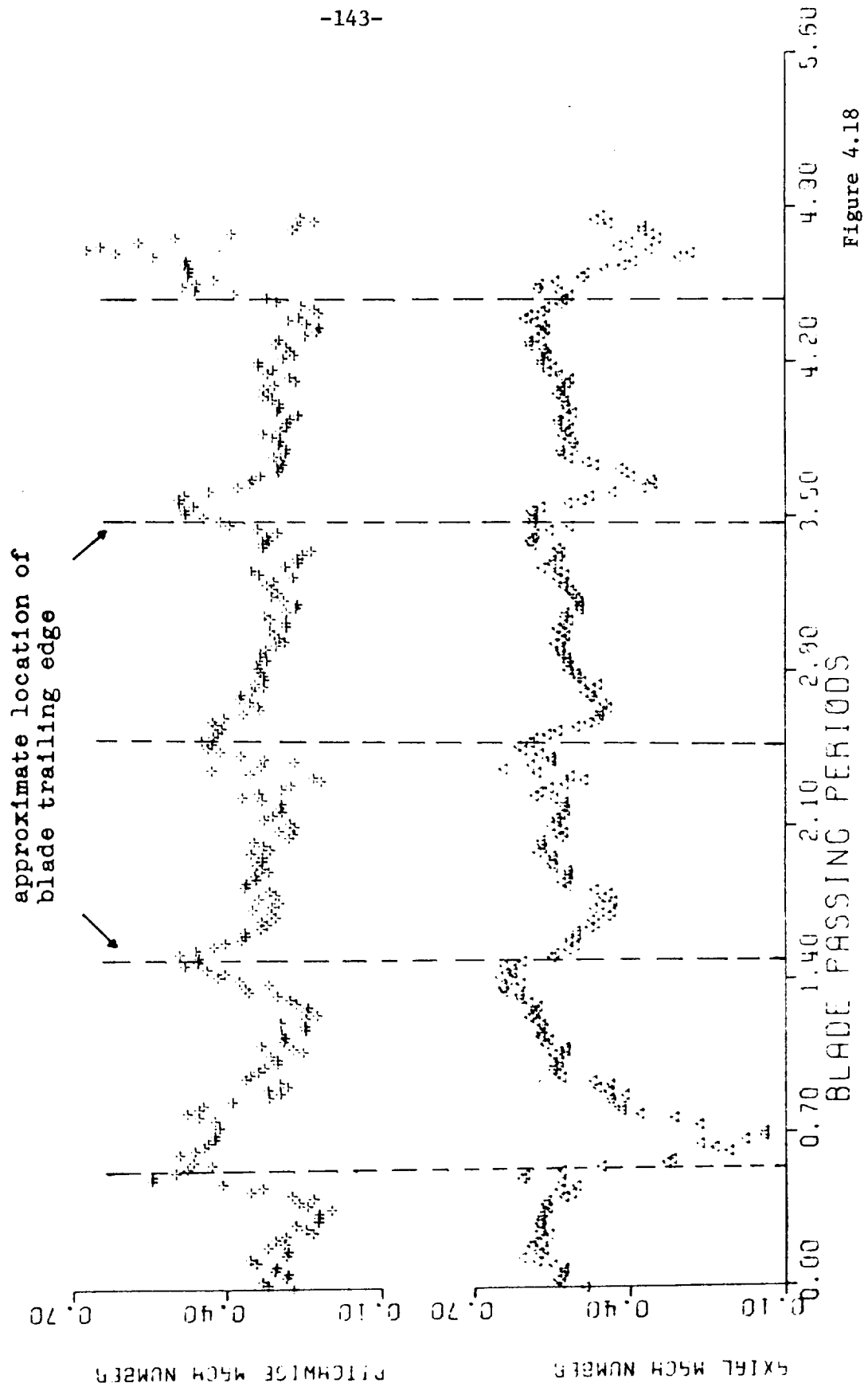


Figure 4.18

MACH NUMBER COMPONENTS
 $R/RT = 0.345$
 0.1 AXIAL CHORDS DOWNSTREAM OF ROTOR

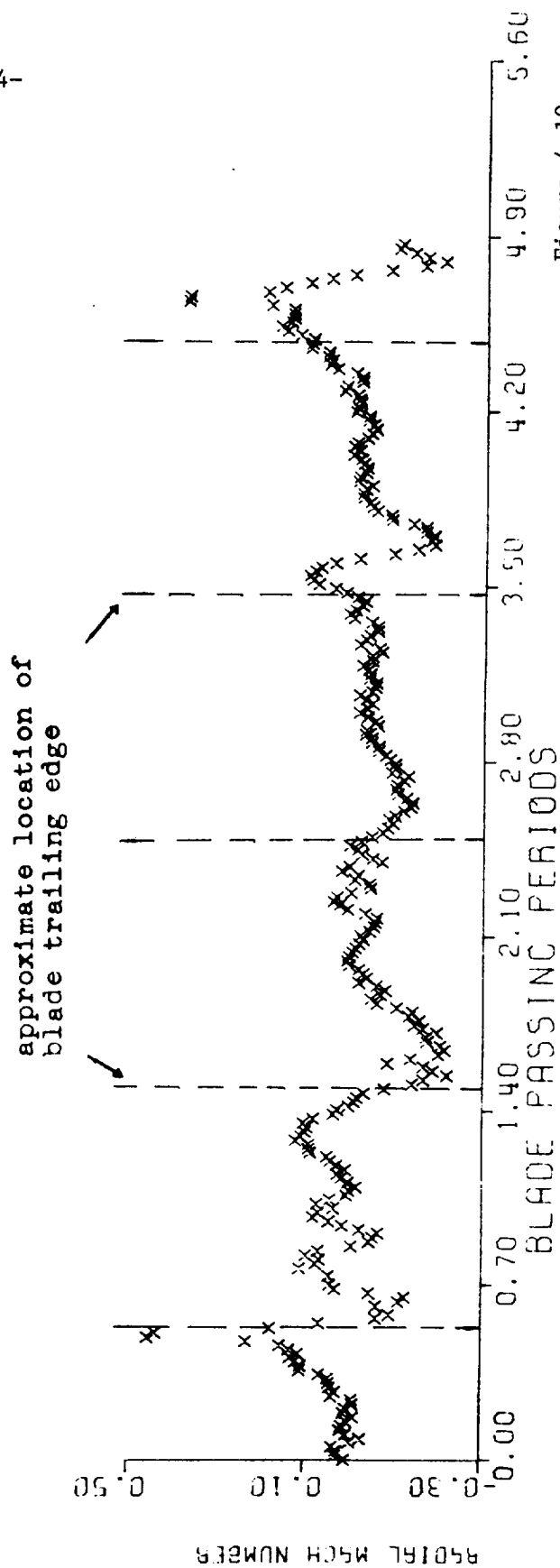
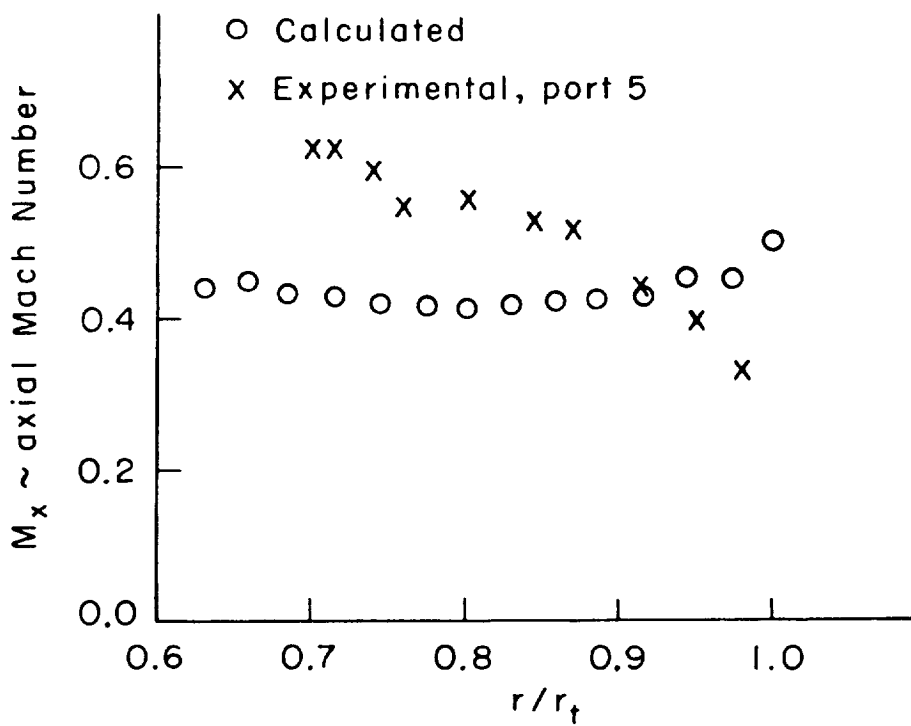
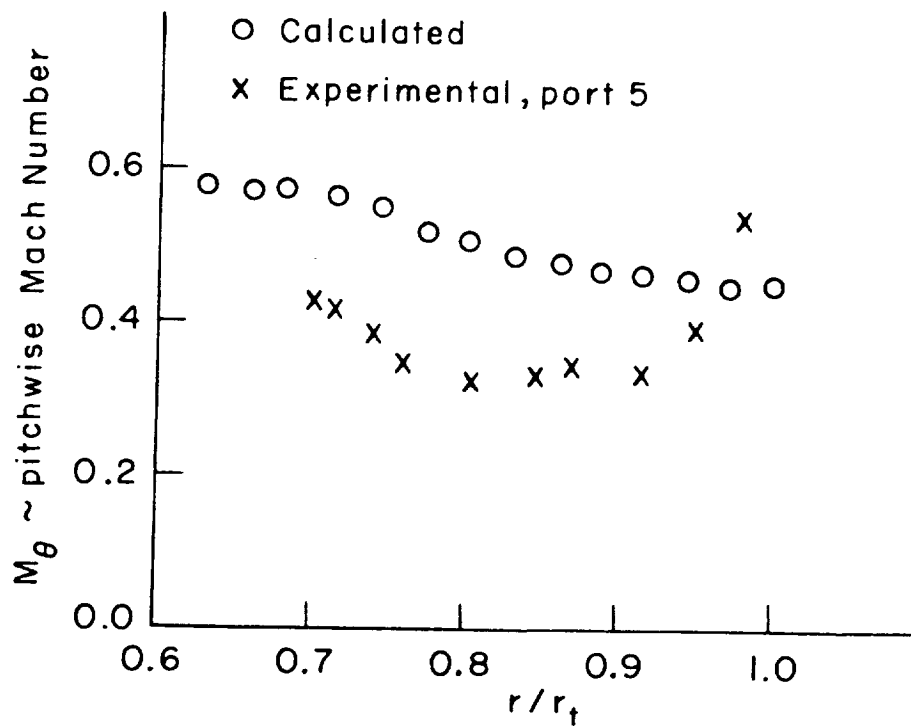


Figure 4.19



Rotor Exit Axial and Pitchwise Mach
Number Profiles Theta Averaged Values

Figure 4.20

